HYDROTHERMAL SYNTHESIS, CHARACTERIZATIONS, AND APPLICATIONS OF NANOSHEETS FROM THAI NATURAL MAGNETIC LEUCOXENE MINERAL

WISSANU CHARERNTANOM

**A DISSERTATION SUBMITTED IN PARTIAL FULFILLMENT OF THE
REQUIREMENTS FOR THE DEGREE OF DOCTOR OF ENGINEERING
PROGRAM IN ENERGY AND MATERIALS ENGINEERING
(INTERNATIONAL PROGRAM)
FACUTY OF ENGNEERING
RAJAMANGALA UNIVERSITY OF TECHNOLYGY THANYABURI
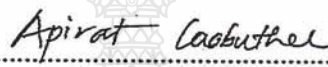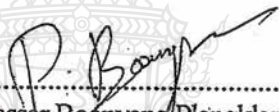ACADEMIC YEAR 2016
COPYRIGHT OF RAJAMANGALA UNIVERSITY
OF TECHNOLYGY THANYABURI**

HYDROTHERMAL SYNTHESIS, CHARACTERIZATIONS, AND APPLICATIONS OF NANOSHEETS FROM THAI NATURAL MAGNETIC LEUCOXENE MINERAL

WISSANU CHARERNTANOM

Dissertation Title	Hydrothermal Synthesis, Characterizations, and Applications of Nanosheets from Thai Natural Magnetic Leucoxene Mineral
Name-Surname	Mr. Wissanu Charerntanom
Program	Energy and Materials Engineering
Dissertation Advisor	Assistant Professor Sorapong Pavasupree, Ph.D.
Academic Year	2016

DISSERTATION COMMITTEE

.... Chairman
(Assistant Professor Sommai Pivsa-Art, Ph.D.)
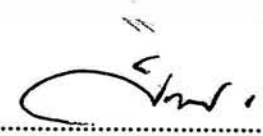
.... Committee
(Associate Professor Apirat Laobuthee, Ph.D.)

.... Committee
(Associate Professor Boonyang Plangklang, Dr.-Ing.)

.... Committee
(Mr.Narongchai O-Charoen, Ph.D.)

.... Committee
(Assistant Professor Sorapong Pavasupree, Ph.D.)

Approved by the Faculty of Engineering, Rajamangala University of Technology Thanyaburi in Partial Fulfillment of the Requirement for the Degree of Doctor of Engineering

....Dean of Faculty of Engineering
(Assistant Professor Sivakorn Angthong, Ph.D.)

Date 3 Month August Year 2017

Dissertation Title   Hydrothermal Synthesis, Characterizations, and Applications of
Nanosheets from Thai Natural Magnetic Leucoxene Mineral
Name-Surname   Mr. Wissanu Charerntanom
Program   Energy and Materials Engineering
Dissertation Advisor   Assistant Professor Sorapong Pavasupree, Ph.D.
Academic Year   2016

ABSTRACT

Titanium dioxide (TiO_2) and the TiO_2-based materials have been deployed in a wide variety of applications, e.g. in dye-sensitized solar cells, water purification and treatment, photocatalytic water splitting, and gas sensors. Moreover, nanosheets are of special interest because of its transformability into various two-dimensional (2D) functional nanostructures. It has large surface area with high chemical activity and quantum confinement effect. The purposes of this research are a) to investigate the prepared nanosheets from Thai magnetic leucoxene mineral using hydrothermal method, b) to study of the nanosheets properties such as size, shape and crystal structure, and c) to know the application of nanosheets on photocatalytic activity and electromagnetic wave absorber application.

This research has experimentally synthesized the nanosheets from the natural magnetic leucoxene mineral under the hydrothermal synthesis condition of 105ºC for 24 hours. Magnetic leucoxene was utilized as the starting material due to its high TiO_2 content (70-80%) and inexpensiveness. The characterization of the synthesized nanosheets was subsequently carried out as follows: crystalline structure, chemical composition, shape, size and specific surface area using X-ray diffraction (XRD), X-ray fluorescence (XRF), scanning electron microscopy (SEM), transmission electron microscopy (TEM) and Brunauer-Emmett-Teller (BET) specific surface area analysis. The said characterization was used to determine the applications of nanosheets on photocatalytic activity and electromagnetic wave absorber applications.

The results indicated that at the beginning, the magnetic leucoxene was of rutile phase while the synthesized nanosheets were of titanate structure ($H_2Ti_xO_{2x+1}$).

After the calcination at the temperature range of 300 and 400 ℃, the calcined samples demonstrated TiO_2 (B). At 500 and 600 ℃, the calcined nanosheets revealed a bi-crystalline mixture consisting of TiO_2 (B) and anatase TiO_2. At 700–1000 ℃, the crystalline structure showed anatase and rutile phase. At 1100 ℃, the prepared samples consisted of a mixture of anatase, rutile phase of TiO_2, and Fe_2O_3 phase. The synthesized product also exhibited the flower-like morphology with 2-5μm in diameter, and the nanosheets structure was slightly curved, with 100nm–2μm in width and 1-3nm in thickness. At 100–200 ℃, the product showed sheets–like structure. At 300–1100 ℃, the calcined nanosheets became unstable and began to decompose and transform into nanoparticles. The increasing size of nanoparticle decreased the specific surface area of the nanosheets caused by increasing calcination temperature. Furthermore, the BET specific surface area of the nanosheets was approximately 279.8 m^2/g. More importantly, the synthesized nanosheets achieved the higher photocatalytic activity under UV and visible light than the commercial TiO_2 nanoparticles (JRC-01, JRC-03, ST-01 and P-25). The electromagnetic wave absorber coin with nanosheets and the commercial TiO_2 nanoparticles (P-25) can absorb electromagnetic wave in gamma (γ) ray and x-ray region were 96.57 and 89.88 % of the initial intensity, respectively. The electromagnetic wave absorber plates made from the as-synthesized nanosheets and recycled high density polyethylene (HDPE) composite could be used for the electromagnetic wave absorption activities in gamma (γ) ray and x-ray region. This synthesis method provided a simple route to prepared nanostructure materials from low-cost Thai mineral with high potential for energy and environment applications.

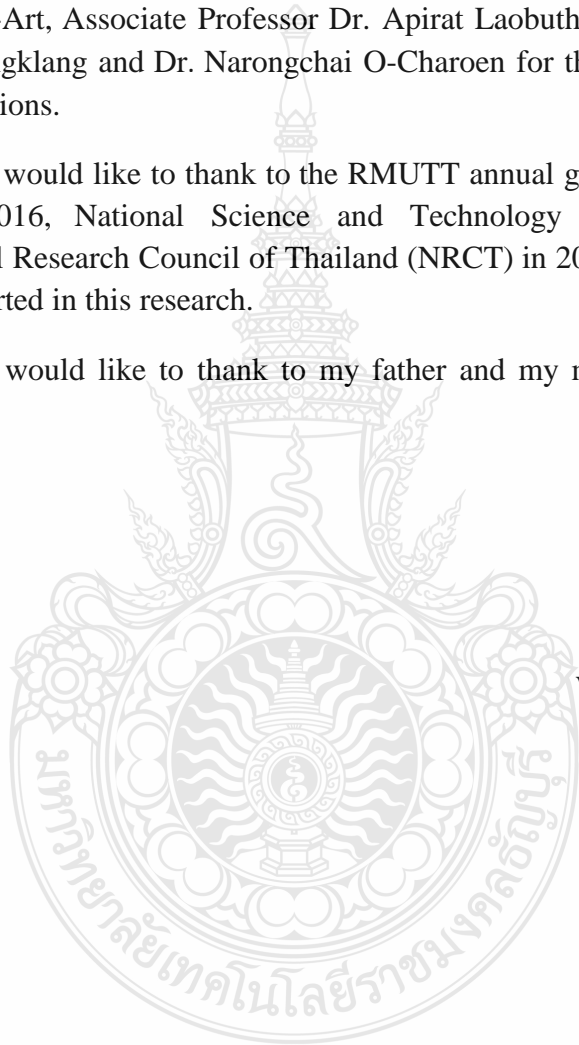**Keywords:** nanosheets, magnetic leucoxene mineral, hydrothermal, titanate, TiO_2

Acknowledgements

Wissanu Charerntanom

Table of Contents

Table of Contents (Continued)

List of Table

List of Figure

List of Figure (Continued)

List of Figure (Continued)

List of Figure (Continued)

List of Figure (Continued)

List of Figure (Continued)

CHAPTER 1

INTRODUCTION

1.1 Research background

Nanotechnology and nanoscience are the rapid evolution of the novel advance technological materials for the section of energy and environmental. Nanomaterials are study about phenomena and materials at scales between 1 nm to 100 nm. In the recent researches nanotechnologies and nanomaterials are attract tremendous attention. The novel technologies preparation and superior physical properties are development materials to application fields. The most nanomaterials application fields are the fields of energy production and environmental such as fuel cells, thermoelectricity, hydrogen conversion, photovoltaic, and environmental purification [1-11].

TiO$_2$-related materials and titanate (H$_2$Ti$_3$O$_7$ Na$_2$Ti$_3$O$_7$ Na$_x$H$_{2-x}$Ti$_3$O$_7$) are importance for environmental purification, industries, and utilizing solar energy. The various applications use TiO$_2$ for catalysts, water treatment materials, gas sensors and a semiconductor in dye-sensitized solar cell. The nanostructured materials (nanosheets, nanotubes, nanofibers, nanowires and nanorods) have been received considerably attended due to novel applications and their unique properties. Several methods are employ in the preparation of the TiO$_2$-derive nanomaterials such as carbon nanotube inner templating, anodic oxidation of a titanium sheet, supramolecular assembly templating, electrodeposition, hydrogen treatment, electrospinning, hydrothermal, anodic porous alumina templating, supramolecular assembly templating, and sol-gel [12-41].

Kasuga et al. first proposed synthesis of TiO$_2$ nanotubes by hydrothermal method. The hydrothermal method is applies prepare low-dimensional TiO$_2$ nanostructures, such as nanosheets, nanotubes, nanowires, nanoparticles and nanofibers. Hydrothermal is a simple process. Temperatures use in the preparation of an extremely in a closed system, low-cost, environmentally friendly and samples are prepare with a special shape high specific surface area [12, 26-27, 32].

Of particular interest for this experimental research is the hydrothermal method due to its straightforwardness whereby the nanomaterials are synthesized in a closed system [50-51]. Moreover, the synthesized materials would be of a distinctive shape and large specific surface area. In this research, the starting material is the naturally-mineral magnetic leucoxene due to its high TiO$_2$ content (70-80%) and inexpensiveness (USD 0.5/kg). Unlike the authors' previous works in which titanium butoxide was the starting material in the nanosheets synthesis [12] and ilmenite in the synthesis of nanofibers [17] using the hydrothermal technology, this current research

has synthesized the high-photocatalytic nanosheets and electromagnetic wave absorber from the naturally-mineral magnetic leucoxene under the hydrothermal condition.

1.2 Purpose of the Study

    1.2.1 To prepared nanosheets from Thai magnetic leucoxene mineral by hydrothermal method.

    1.2.2 To study the properties nanosheets such as size, shape, crystal structure, and so on.

    1.2.3 To study photocatalytic application of nanosheets.

    1.2.4 To study electromagnetic wave absorber application of nanosheets.

1.3 Scope of the Study

    1.3.1 Prepare nanosheets from Thai magnetic leucoxene mineral by simple hydrothermal method.

    1.3.2 Characterize the properties of nanosheets such as chemical properties of nanosheets by X- ray fluorescence, (XRF), crystal structure with X-ray diffraction, (XRD), shapes and sizes with a scanning electron microscope, (SEM) and transmission electron microscope, (TEM), specific surface area with Brunauer-Emmett-Teller (BET) analysis.

    1.3.3 Photocatalytic activity will be investigate under UV light and visible light.

    1.3.4 Electromagnetic wave absorber application will be investigate under grammar ray (γ- ray) and X- ray wavelength.

1.4 Benefits of the Research

    1.4.1 To obtain nanosheets from raw material of Thailand.

    1.4.2 To obtain the knowledge about the nanosheets material with unique properties.

    1.4.3 To obtain the applications of nanosheets such as photocatalytic and electromagnetic wave applications.

CHAPTER 2

BACKGROUNDS AND THORETICAL

2.1 Titanium Dioxide

Titanium dioxide (TiO_2) is known titania or titanium (IV) oxide from a natural occur oxide of titanium element. Titanium dioxide chemical formula is TiO_2 present white powder [35]. TiO_2 is transition metal oxides. TiO_2 found four common polymorphs: (Table 2.1) rutile (tetragonal structure lattice constants a= 4.5936 °A, c=2.9587°A unit cell contains 6 atoms), anatase (tetragonal structure lattice constants a= 3.784 °A, c= 9.515 °A) (Figure 2.1), TiO_2 (B) (monoclinic) and brookite (orthorhombic lattice constants a= 9.184 °A, b= 5.447 °A, c= 5.154 °A) (Figure 2.2) [36,]. In high pressures and high temperatures brookite phase and anatase phase transform to the rutile phase more stable than anatase phase for sizes particle greater than 14 nm and grow faster than anatase phase. Rutile phase can stable at up to 60 k bar and photocatalyst activity very poor [37-38]. Oxygen deficiency Titanium dioxide is an n-type semiconductor [39]. The anatase band gap is 3.2 eV, brookite is~3.2 eV and rutile is 3.0 eV [40]. The investigate photocatalyst is TiO_2 due to low cost, high photo-activity, thermal stability good chemical and low toxicity [41]. Fujishima and Honda reported in 1972 is the first major advance the photoelectrochemical splitting of water The first major advance was in 1972 when Fujishima and Honda reported the photoelectrochemical splitting of water used anode TiO_2 and counter electrode Pt [42].

Table 2.1 Crystal structure data for TiO_2 [43]

Properties	Rutile	Anatase	Brookite
Crystal structure	Tetragonal	Tetragonal	Orthorhombic
Lattice constant (Å)	$a = 4.5936$ $c = 2.9587$	$a = 3.784$ $c = 9.515$	$a = 9.184$ $b = 5.447$ $c = 5.154$
Space group	$P4_2/mnm$	$I4_1/amd$	Pbca
Molecule (cell)	2	2	4
Volume/ molecule (Å^3)	31.2160	34.061	32.172
Density (g cm^{-3})	4.13	3.79	3.99
Ti–O bond length (Å)	1.949 (4) 1.980 (2)	1.937(4) 1.965(2)	1.87–2.04
O–Ti–O bond angle	81.2° 90.0°	77.7° 92.6°	77.0°–105°
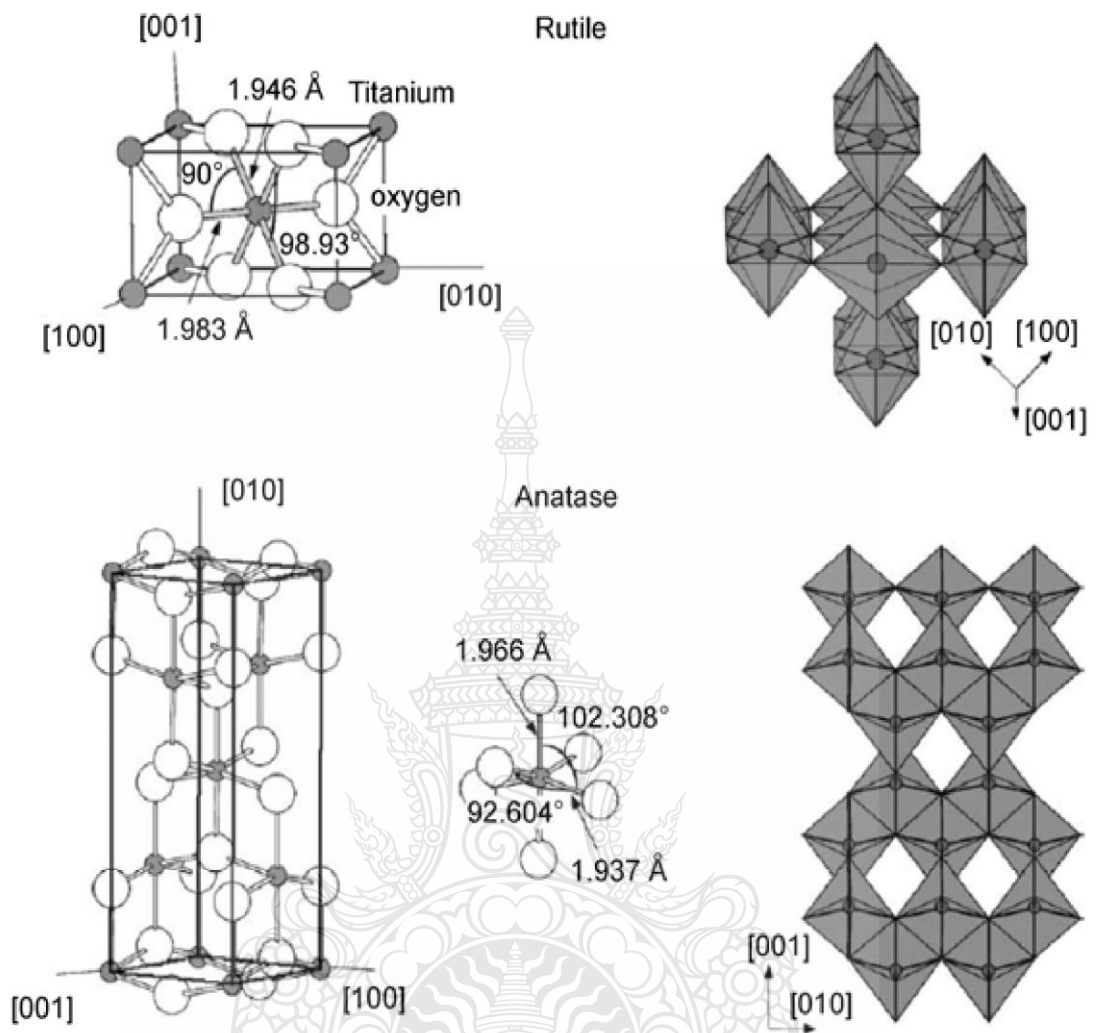
Figure 2.1 Crystal structures of the rutile and anatase phases of TiO$_2$ [43].
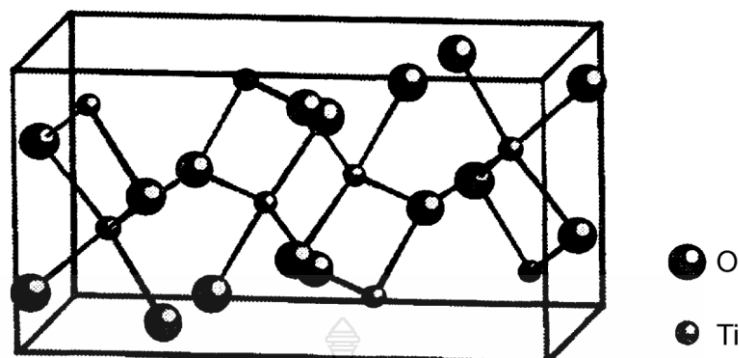
Figure 2.2 Lattice structure of brookite TiO_2 [43].

Table 2.2 Physical properties of TiO_2[44].

Physical properties of TiO_2	
Molecular weight	79.87g/mol
Density	4.23 g/cm^3
Melting point	1870 °C
Boiling point	2972°C
porosity	0%
Dielectric constant (1 MHz)	85
Thermal conductivity (25°C)	11.7 Wmk^{-1}
Electrical resistivity (25°C)	10^{12} ohm.cm
Electrical resistivity (700°C)	2.5x10^4 ohm.cm
Young 's modulus	230 GPa

Table 2.2. shows the TiO_2 physical properties. The TiO_2 energy band gap is 3.2 eV, high photoreactivity, biocompatibility, chemical stability, include strong ultraviolet absorptivity, long-term photostability, non-toxicity and cost-effectiveness due to these properties extraordinary. The utilized several applications of TiO_2 is for energy-related devices, dye-sensitized solar cells (DSSCs), antibacterial compositions, hydrogen storage, self-cleaning ceramics and glass, lithium ion battery, optoelectronic device, photocatalyst humidity sensor, water-splitting, and photocatalyst for organic pollutants degradation [45]. The titanium metal processes and production of TiO_2 pigment shown in Figure 2.3. The chloride process to manufacture titanium pigment to the pigment industry. [46]. Therefore, TiO_2 nanomaterials are prepared by many processes such as micelle and inverse micelle,

hydrothermal, chemical vapor deposition electro-deposition, solvothermal, sol–gel and so on [12-34].
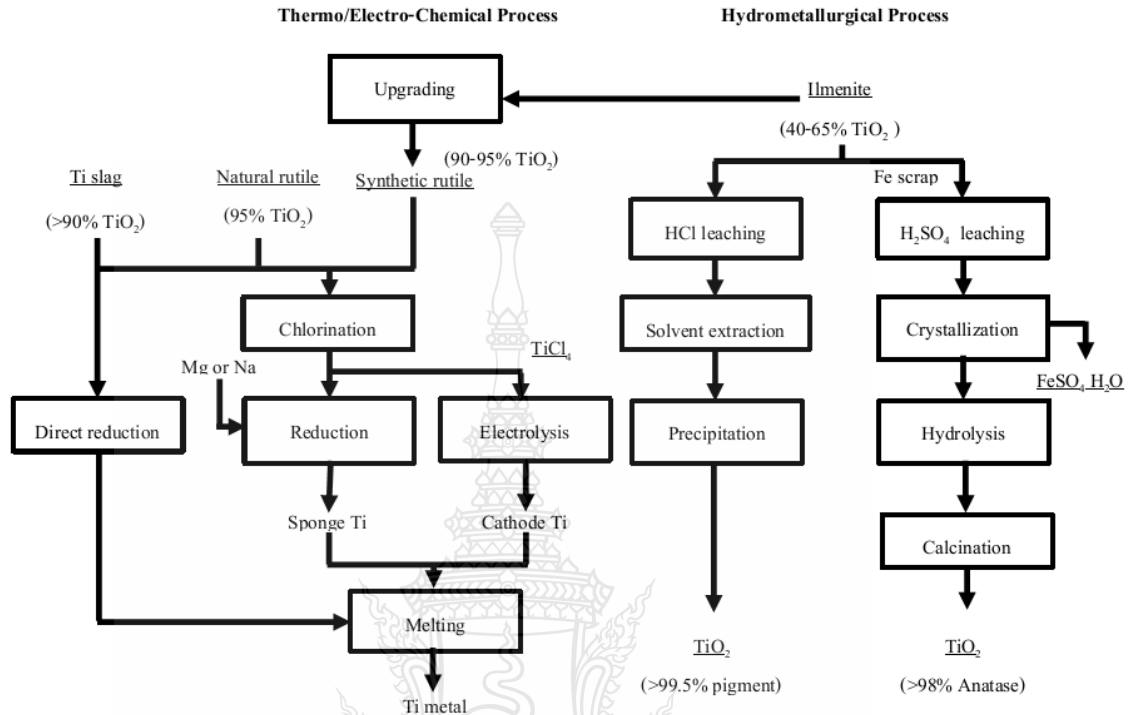
Figure 2.3 The processes production of Ti metal and pigment TiO_2 [46].

2.2 Magnetic Leucoxene Mineral

Magnetic leucoxene mineral is one of TiO_2-related mineral. The main component TiO_2 mineral has five type minerals such as Ilmenite mineral TiO_2 ~50 - 60 %, Hydro Ilmenite mineral TiO_2 ~60 - 70 %, Magnetic Leucoxene mineral TiO_2 ~70 - 80 %, Leucoxene mineral TiO_2 ~80 - 90 %, Rutile mineral TiO_2 ~90 - 100 %. Magnetic Leucoxene mineral consists mainly of TiO_2 and mixture of portions of the impurities Fe_2O_3, Al_2O_3, CaO, SiO_2, MnO, Nb_2O_5, MgO and SO_3.

2.3 Hydrothermal Technology

Sir Roderick Murchison (British Geologist) was the first person to use word "hydrothermal" (1792–1871) to explain action of water at high pressure and high temperature in the earth's crust to formation of minerals and various rocks. The Hydrothermal method has been gathering interest, and popular from technologists and scientists of properties extraordinary. The word "hydrothermal" has geological origin.

A self-explanatory word "hydro" meaning water and "thermal" meaning heat. [47]. In 1845K. F. E. Schafthaul was the first person to hydrothermal research publication reports the synthesis of freshly precipitated silicic acid in Papin's digestor transformation to tiny quartz crystals. The term hydrothermal usually refers to mineralizers under high pressure and temperature conditions or any heterogeneous reaction in the presence of aqueous solvents [48].

The nanomaterials in hydrothermal processing can be explained to process of preparation nanoparticles from sub-micron by superheated aqueous solution. Nanostructured materials exhibit interesting properties including and unique, improvement of mechanical, electrical, physical and chemical properties [49]. The special advantages of hydrothermal technique is avoidance of pollution, fast reaction times, lowest residence time, lower energy consumption, controlled stoichiometry, lower temperature operations in the presence of the solvent, higher dispersion, narrow particle size distribution, higher rates of reaction, high quality, simple equipment, uniformity, controlled microstructure, excellent reproducibility, high crystallinity, dense particles, controlled morphology, the high control diffusivity in a strong solvent media in a close system, high purity, less defects, and so on [50-53].

The synthesis of hydrothermal offers more advantages than non conventional and conventional synthesis methods. The advanced methods have the respective costs for instrumentation, prepare a large variety of forms, precursors and energy are less for hydrothermal processes. Hydrothermal methods are more environmentally from the environmental perspective than many other methods. The encounter problems of high temperature processes were stress-induced defects and poor stoichiometric control due to volatilization of components such as cooled to room temperature of phase transformations that as the phosphor. Moreover, the phosphor powders ability to precipitate directly from solution the uniformity and regulates rate of nucleation, aging and growth, which aggregation control, affects size, particle sizes and morphology possible with hydrothermal processing that is not possible with many synthesis processes. This beneficial of method to industries which pigments, medical diagnostics pharmaceuticals, materials, will benefit from powders with controlled morphology and size for a wide range of reasons. The preparation difficult to prepare different phases of $PbWO_4$ phosphor with other synthetic methods allows to the unique pressure-temperature interaction of the hydrothermal method. [52]

Hydrothermal synthesis can be hybridized with other method such as optical radiation, mechano-chemistry, ultrasound, electrochemistry, microwave and hot-pressing to gain advantages such as increase ability to make new materials and enhancement of reaction kinetics. The hybridize method does not need any template, seed, expensive surfactant, and harmful or catalyst thus it is promising for low-cost production and large-scale with high-quality crystals.

2.4 Photocatalysis

Photocatalysis is composes of two word the first word "photo" from light and the second word "catalysis" from decompose, brake apart. The definition of photocatalysis describe in term to process a substance activate by light, the rate of a chemical reaction modifies by the photocatalysts, which without chemical transformation being involved itself. The difference between a photocatalysts and conventional thermal catalyst is activated by photons and activated by heat. The reactions of photocatalytic may occur heterogeneously or homogeneously. Heterogeneous photocatalysis is potential use to energy-related applications and a variety of environmental more than organic syntheses. The photocatalysis of heterogeneous reaction scheme is formation of an interface between a products of the reaction and a fluid containing the reactants and solid photocatalyst [53].

2.5 Semiconductors

The characteristics of electronic described by the band theory are semiconductors, insulators, and conductors. Solid material has large number of atoms interact, the energy levels are closely space form band. The electrons fill these bands from the lowest energy to the highest, and each band has a different energy, similar to a single atom way in the that electrons occupy the orbitals. The valence band (VB) is the highest energy fill band highest occupied molecular orbital (HOMO) in a molecule. The conduction band (CB) is the next higher band to the lowest unoccupied molecular orbital (LUMO) in a molecule, is called. The energy bandgap (E_{bg}) are separated the VB and the CB. The insulator semiconductor, or conductor material determine size of the bandgap [45] (see Figure 2.4).
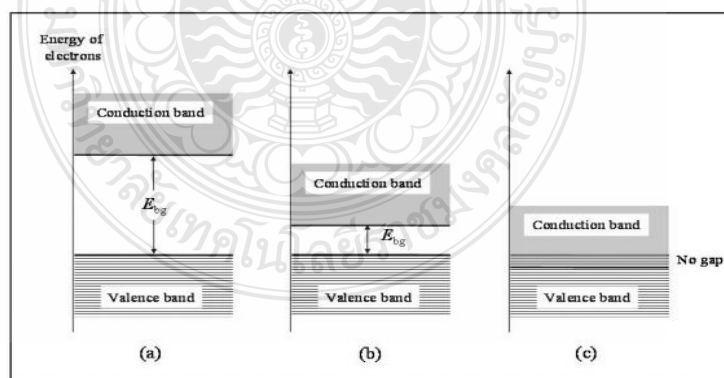
Figure 2.4 Energy bands in solids: (a) insulator ; (b) semiconductor ; (c) conductor[53].

Electrons are the majority carriers and the electron concentration call n-type semiconductor, holes are the majority carriers and their concentration is call p-type semiconductors is shown in Figure 2.5.

22
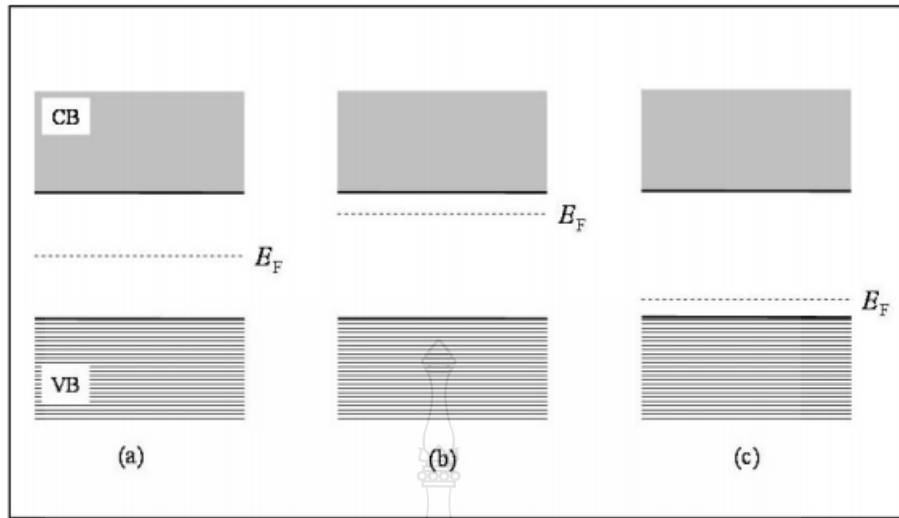
Figure 2.5 Position of fermi level relative to VB and CB for (a) intrinsic, (b) *n-type* and (c) *p-type* semiconductors [53].

2.6 Electromagnetic Waves

The electromagnetic waves are the waves from component of undulating magnetic fields and electrical fields. The electromagnetic waves have many different kinds such as radio wave, microwave, Infrared, visible light, ultraviolet, X-rays, gamma rays, cosmic rays.

The electromagnetic waves absorbers are material for absorbing electromagnetic waves, magnetic permeability and electric permittivity. The electromagnetic waves absorbers used for absorbing, screen and shield electromagnetic waves to damage of equipment and human. The mechanism of electromagnetic waves absorption starts with first, incident waves come to electromagnetic waves absorbers some waves reflected, some waves transmitted, some secondary reflected and some secondary transmitted are shown in Figure 2.6
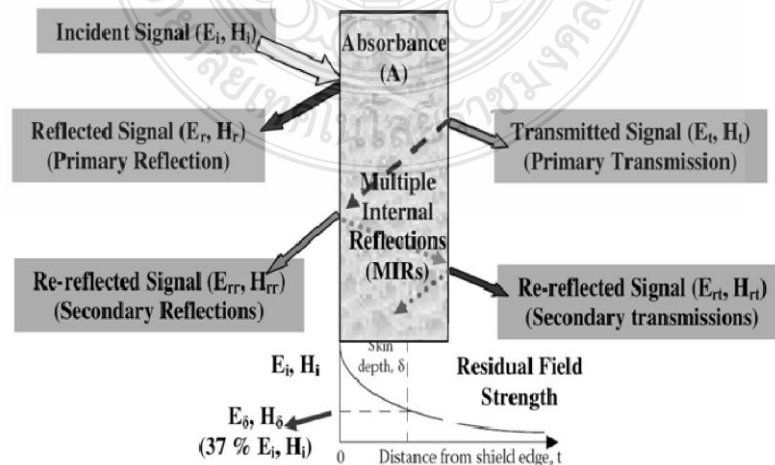
Figure 2.6 Mechanism of electromagnetic waves absorption [54].

23

2.7 X-ray Diffraction Spectroscopy (XRD)

The X-ray Diffraction (Figure 2.7) used to analyze unit cell dimensions, lattice of crystalline substances, details of site-ordering, bond-angles and including bond-lengths. These techniques is non-destructive technique detailed , and observing the scattered intensity of an X-ray beam attack a sample as a function of incident polarization, scattered angle, and energy or wavelength [55-56].

The X-ray diffraction spectroscopy have main three parts sample holder, X-ray detector and X-ray tube. The cathode filament generated X-rays to produce electrons, applying a voltage accelerate electrons to a target and impact target material. When electrons have sufficient energy to dislodge inner shell electrons of the target material, produce characteristic X-ray spectra. These spectra consist of several components, the most common being K_α and K_β. K_α consists, in part, of $K_{\alpha 1}$ and $K_{\alpha 2}$. $K_{\alpha 1}$ has a slightly shorter wavelength and twice the intensity as $K_{\alpha 2}$. The specific wavelengths are characteristic of the target material. Filtering, by foils or crystal monochro-meters, is required to produce monochromatic X-rays needed for diffraction. $K_{\alpha 1}$ and $K_{\alpha 2}$ are sufficiently close in wavelength such that a weighted average of the two is used. Molybdenum is the most common target material for single-crystal diffraction, with MoK_α radiation = 0.7107Å. These X-rays are collimated and directed onto the sample. When the geometry of the incident X-rays impinging the sample satisfies the Bragg Equation (equation 2.12), constructive interference occurs. A detector records and processes this X-ray signal and converts the signal to a count rate which is then output to a device such as a printer or computer monitor.

$$n\lambda = 2d\ \sin\theta \qquad (2.12)$$

where   n is an integer,

         λ is the wavelength of incident wave,

         d is the spacing between the planes in the atomic lattice and

         θ is the angle between the incident ray and the scattering planes.

The wavelength of electromagnetic radiation explain by this law relates of the lattice spacing and diffraction angle in the crystalline sample. The change geometry of the incident rays, all possible diffraction directions of the lattice, the orientation of the centered crystal and the detector, should be attained detected processed, counted and diffracted X-rays.

Figure 2.7 Diffraction of X-ray in material [56].

2.8 X-ray Fluorescence Spectroscopy (XRF)

The X-ray fluorescence spectrometry (XRF) (Figure 2.8-2.9) used for an elemental analysis of minerals, rocks, fluids and sediments. The X-ray fluorescence technique is non-destructive technique used extensively in industry and science. The technique is advantage in the stability, low cost and including simplicity. The X-ray fluorescence principle of involve to interact with X-ray radiation and the behavior of atoms. The x-ray fluorescence analysis of behavior of atoms with interact radiation in elements materials. The materials are excite from X-rays radiation, high-energy, to ionized. The sufficient radiation energy to dislodge a tightly-held inner electron, atom are unstable and outer electron replace missing inner electron. the decreased binding energy due to released energy of the inner electron orbital compare with an outer one. The fluorescent radiation is emitted radiation of lower energy than the primary incident X-rays. Because the characteristic of a transition between specific electron orbitals in a particular element is energy of the emitted photon. The X-rays fluorescent can use to detect the elements sample.[57-58]

Figure 2.8 Basic components of X-ray fluorescence spectrometry [58].
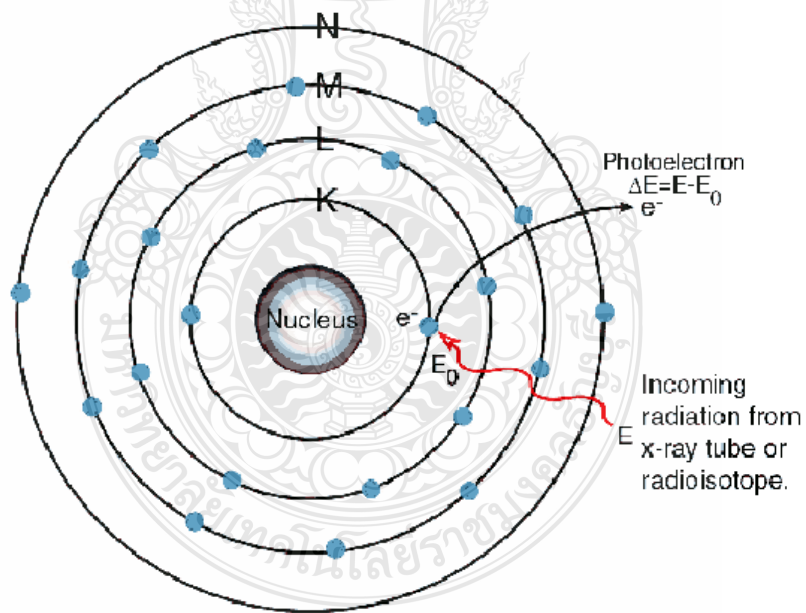
Figure 2.9 The generation of X-ray fluorescence radiation [59].

2.9 Scanning Electron Microscopy (SEM)

The scanning electron microscope (SEM) (Figure 2.10) is an instrument that produces a largely magnified image by using electrons instead of light to form an image. The principle scanning electron microscope start with the electron source generate electrons enter to the system. The electrons were accelerated by the electric field. Then the electrons fill through the condenser lens to make the electron beam and can be adapted to the size of the electron beam. The electron beam is scattering electrons of the sample. It will be the focus of the objective lens. Next, expanded and fit length of electron beams to display for projector lens create signal to translate picture. These signals include secondary electrons that produce SEM images The SEM techniques magnification f can be magnified range approximately from 20 to 300,000 magnified. [60-61].
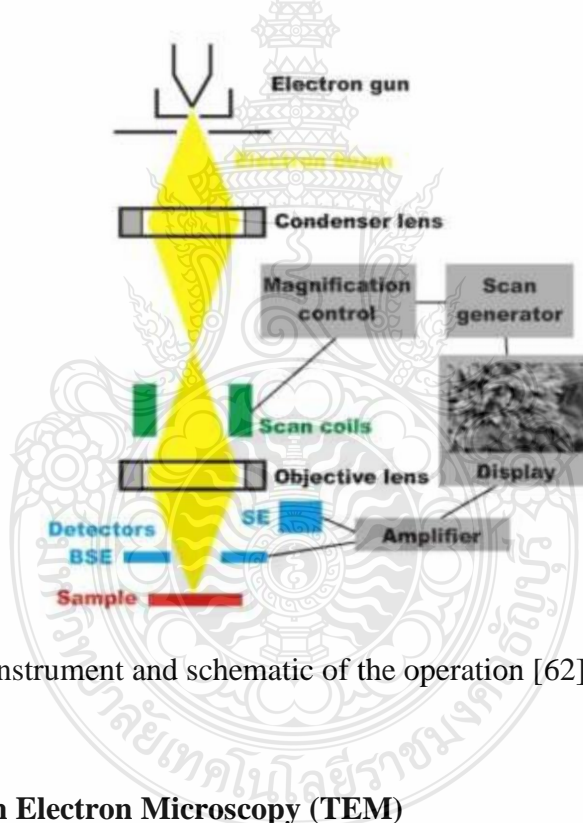
Figure 2.10 SEM instrument and schematic of the operation [62].

2.10 Transmission Electron Microscopy (TEM)

The transmission electron microscope is an instrument used electrons instead of light to create a magnified image and applied in photography to detail and high magnification. The principle transmission electron microscope start with the electron source generate electrons enter to the system. The electrons were accelerated by the electric field. Then the electrons fill through the condenser lens to make the electron beam and can be adapted to the size of the electron beam. The electron beam is through the flat and very thin sample when electrons pass through the sample and scattering

electrons. It will be the focus of the objective lens. Next, expanded and fit length of electron beams to display for projector lens create signal to translate picture. Figure 2.11. [63-64].
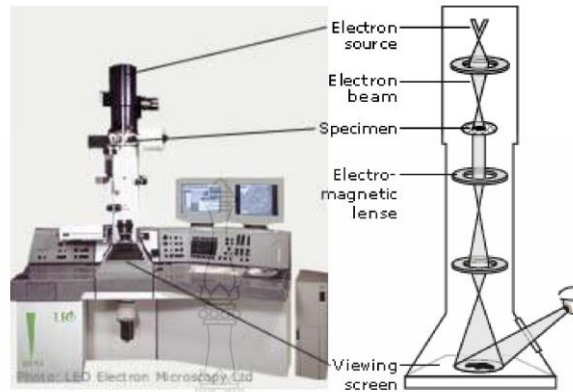
Figure 2.11 TEM instrument and schematic of the operation [65].

2.11 The Brunauer-Emmett-Teller Analysis (BET)

The Brunauer-Emmett-Teller (BET) (Figure 2.12) analysis specific surface area and pore volume. The Brunauer-Emmett-Teller generally have two cells, one containing sample and the other cells is reference cell sample before the test must provide heat to the cells to displace moisture and molecules contaminated of the surface material. Then evacuate cells to displace molecules and other gases. Next, dipping the two cells into the liquid nitrogen container to low temperatures stat. After, fill nitrogen gas into the cell to adsorption, nitrogen gas is adsorbs on the surface of the material. Then release nitrogen gas to desorption, nitrogen gas is desorbs out the surface of the material, The pursue Phenomenon of the relative pressure and volume of nitrogen gas to predict specific surface area and pore volume of sample material.. [66-67].
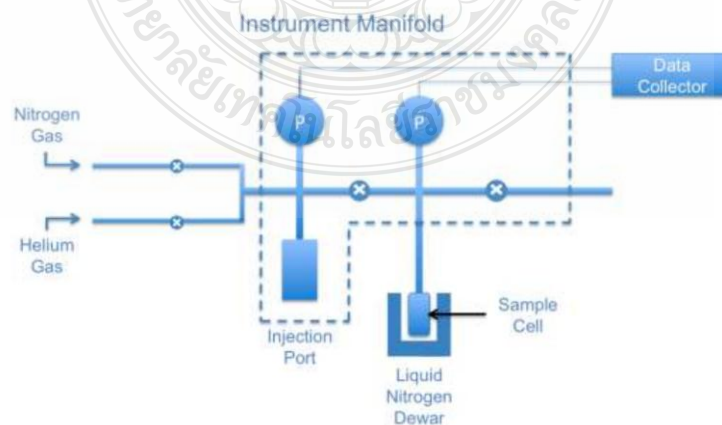
Figure 2.12 The schematic of the BET instrument [68].

2.12 UV-Vis Spectroscopy

UV/Vis spectrophotometer (Figure 2.13) is an instrument used to measure the amount of light and intensity light to pass through the sample in the region of ultraviolet (UV) and the visible light. The wavelength is related to the amount and type of the material sample. The sample mostly in organic, organic complexes and inorganic substances that can absorb light in this wavelength range. The sample light absorption properties is accelerated irradiate with UV light or white light with optimal energy to exited electrons. The atoms electrons will absorb the light and energy change the status to the high energy floor level. Then compare light that passes through or reflected from the sample with reference by Beer-Lambert law. The absorbance of the sample will vary depending on the number of absorb light molecules. T UV/Vis spectrophotometer can be measure light absorption in the wavelength range 190 to 900 nm. [69-70].
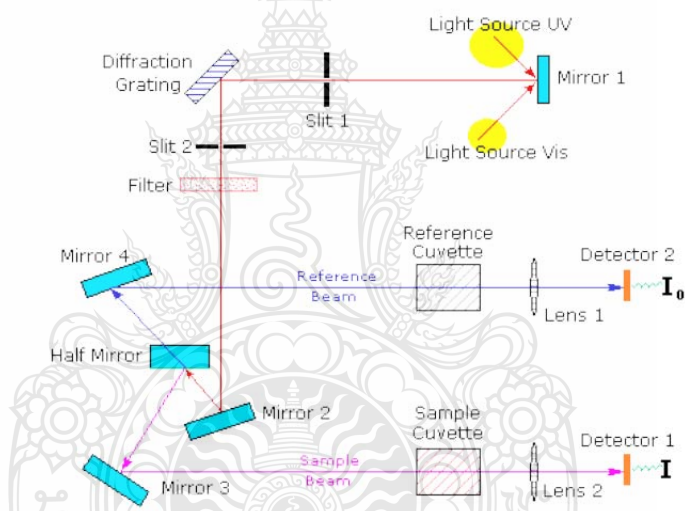
Figure 2.13 Basic components of UV-Vis spectrometer [70].

2.13 Electromagnetic Wave Absorption Measurement

The principle of electromagnetic wave absorption measurements uses Americium -241 for Grammar ray (γ- ray) primary X-ray sources to generate electromagnetic wave. When the electromagnetic wave move attack the sample some waves absorbs, some waves reflects and some waves transmits. The transmits waves go to electromagnetic detector. The electromagnetic detector receive electromagnetic wave and translate signal to analyze data. (Figure 2.14)
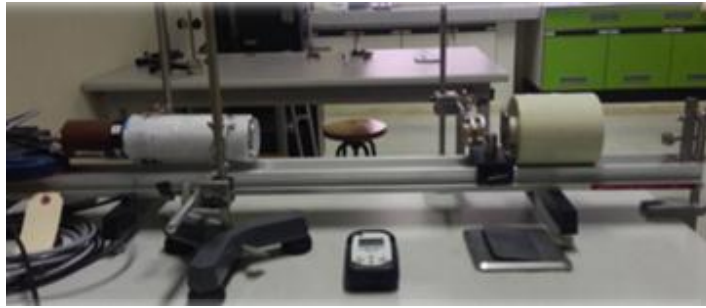
Figure 2.14 Electromagnetic wave absorption measurements.

2.14 Literature Review

Pavasupree, S. et al. [12] study of mesoporous nanosheets TiO_2 structure synthesize by hydrothermal method at 130 °C for 12 h. The morphology of nanosheets are flower-like structure have diameter about 500 nm to 2 μm (Figure 2.15). The TEM images show diameter of nanosheets TiO_2 is about 50-100 nm in width, thickness is several nanometers (Figure 2.16) and crystalline structure is anatase TiO_2 (Figure 2.17). The specific surface area and pore volume about 642 m^2/g and pore volume about 0.774 cm^3/g,. The structure of nanosheets was changed after heat treatment at 300–500 °C into nanorods/nanoparticles composite with anatase TiO_2 structure. The nanosheets showed almost nanoparticles with a mixture of anatase and rutile TiO_2 structure from increasing temperature to 600-700 °C. Nanosheet was about 7.08% with Jsc of 16.35 mA/cm^2 P-25 reached 5.82% with Jsc of 12.74 m A/cm^2.
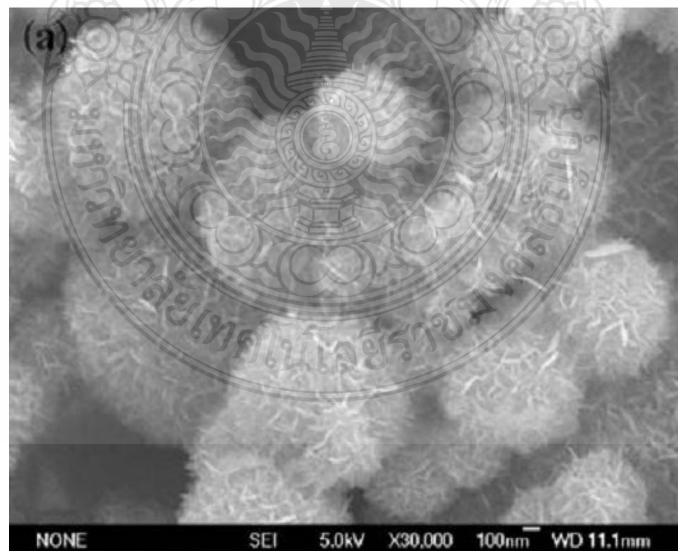
Figure 2.15 SEM images of flower-like nanosheets TiO_2 at (a) x 30,000 and (b) x 100,000 magnified [12].
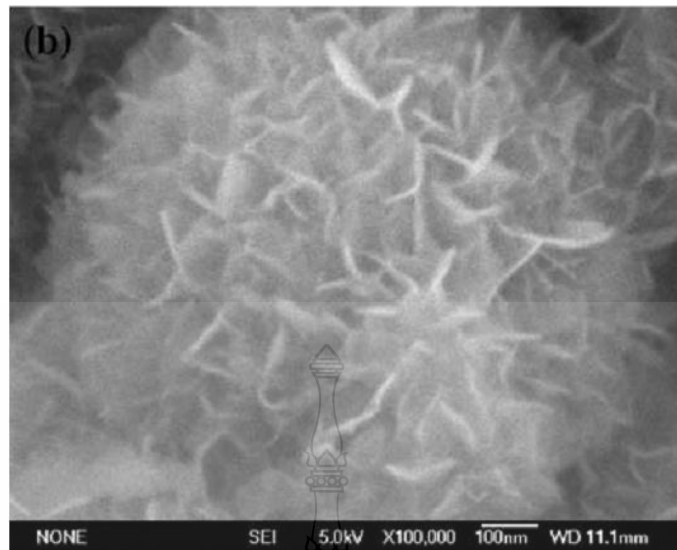
Figure 2.15 (cont.) SEM images of flower-like nanosheets TiO_2 at (a) x 30,000 and (b) x 100,000 magnified [12].
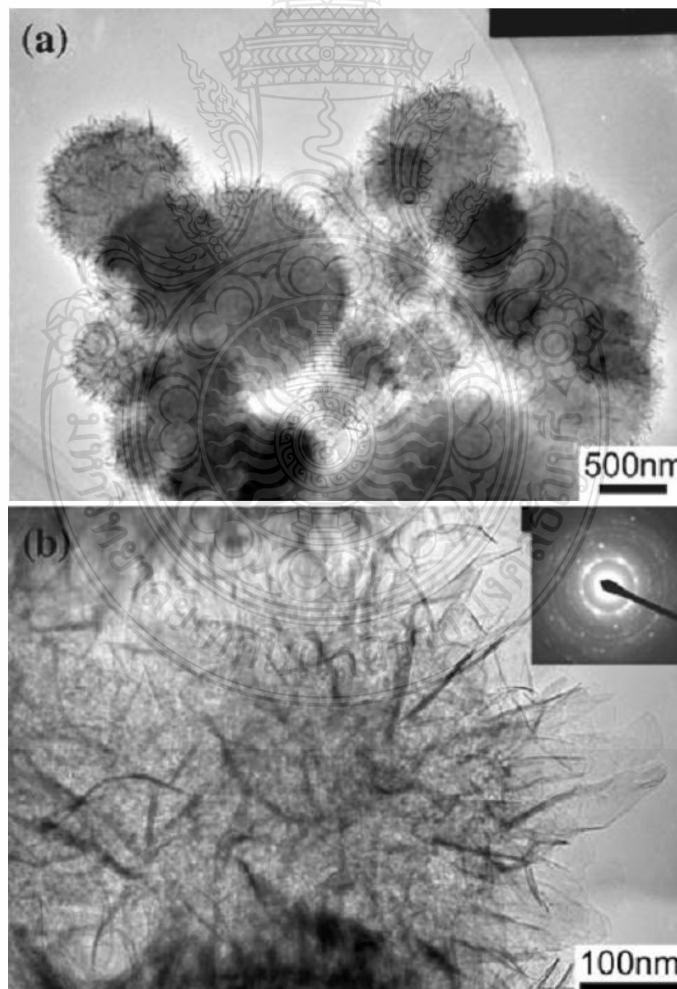
Figure 2.16 TEM images of (a-c) flower-like nanosheets TiO_2[12].
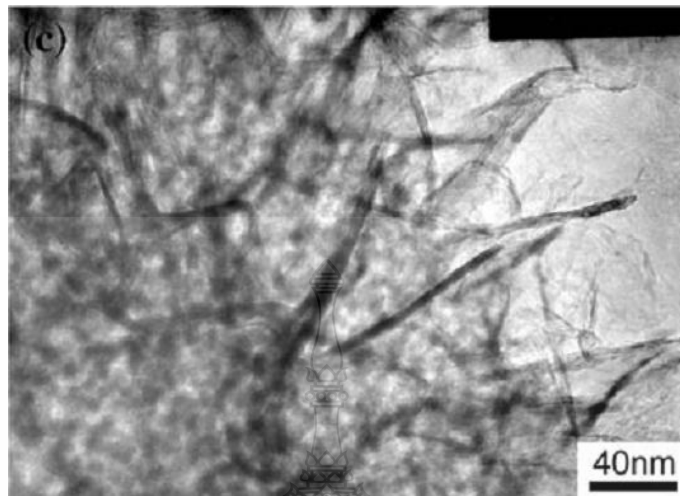
Figure 2.16 (cont.) TEM image of (a-c) flower-like nanosheets TiO_2[12]
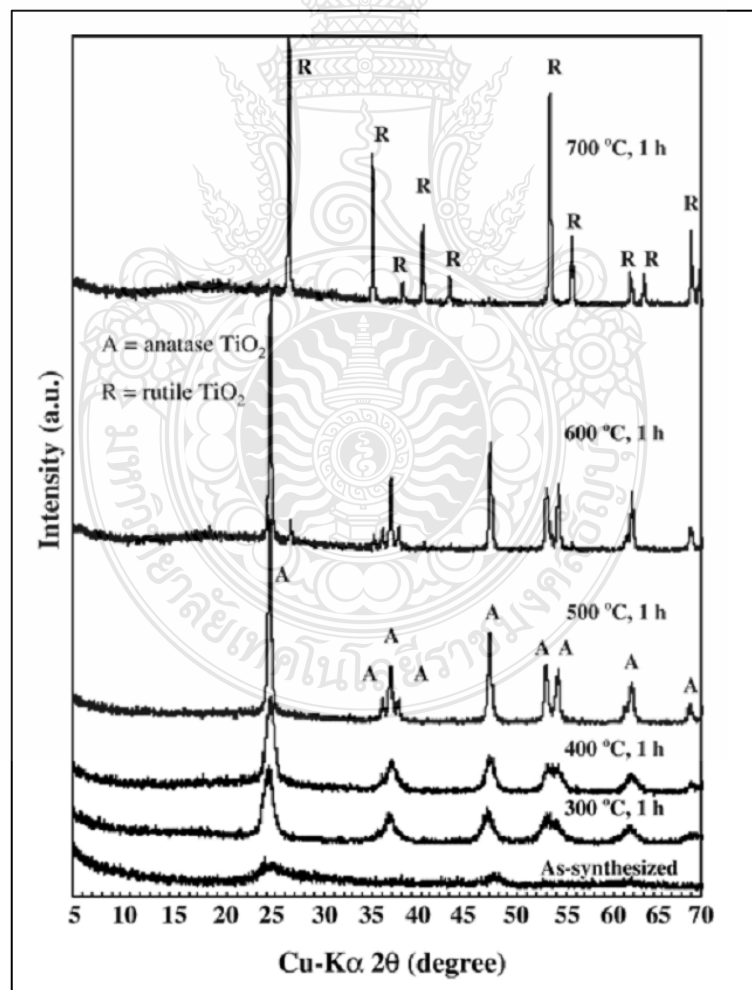
Figure 2.17 XRD patterns of flower-like nanosheets TiO_2[12]

32

Jitputti, J. et al. [13] study of superstructure flower-like titanate synthesize by hydrothermal method. The titanium tetraisopropoxide is starting material and the solution is ethanol and ammonia use temperature at 120 °C for 24 h. After, that washed by distilled water and ethanol. The diameter of flower-like titanate were 250-450 nm (Figure 2.18), the specific surface area were 350.7 m^2/g. Heat increasing temperature to treatments at 500 °C, the titanate nanosheets crystalline structure is convert into anatase TiO_2 with moderate deformation of their structures. The heat treated flower-like titanate at 500 °C showed high photocatalytic activity than the commercial grad TiO_2 anatase powder (ST-01) for H_2 evolution from water splitting reaction (Figure 2.19).
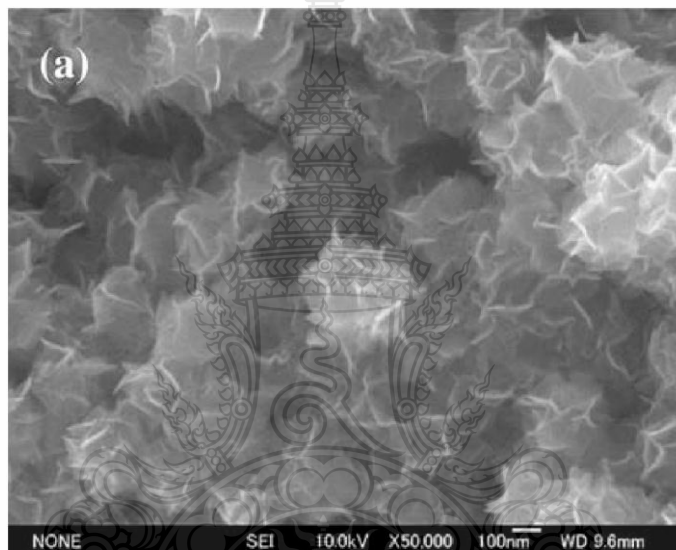
Figure 2.18 SEM image of flower-like nanosheets TiO_2 at x 50,000 magnified [13].
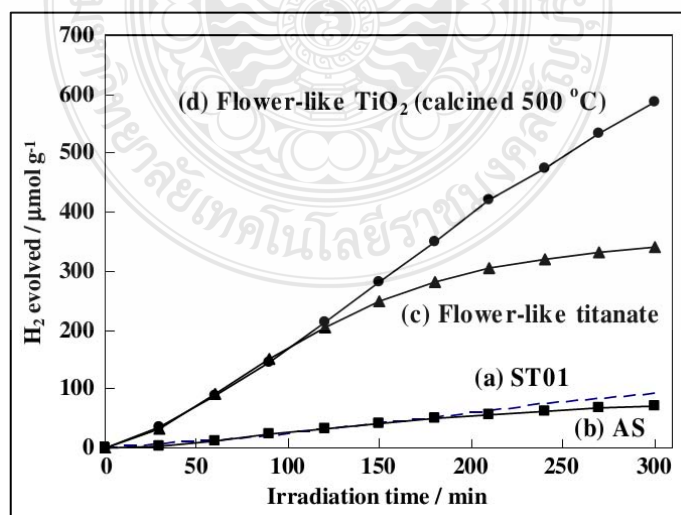
Figure 2.19 Photocatalytic activity for H_2 evolution from water splitting reaction of flower-like nanosheets and commercial nanoparticles TiO_2 [17].

Simpraditpan A. et al. [17] studied on the effect of calcination temperature of nanofibers. The nanofibers are synthesize by hydrothermal method at 130 °C for 72 h. The starting material is natural ilmenite mineral. The nanofibers diameter are 20–90 nm and length are 2–7 mm (Figure 2.20). The as-synthesize nanofibers calcination at 300–400 show $TiO_2(B)$, at 500 °C show a mixture of two phases of $TiO_2(B)$ and anatase, at high temperature of 600–1000 °C show a mixture of tri-crystalline of anatase, rutile, and Fe_2O_3 (Figure 2.21). The photocatalytic activity of the nanofibers calcination at 400 °C for 2 h is higher than the commercially TiO_2 nanoparticles powders (P-25, JRC-01, and JRC-03) (Figure 2.22).
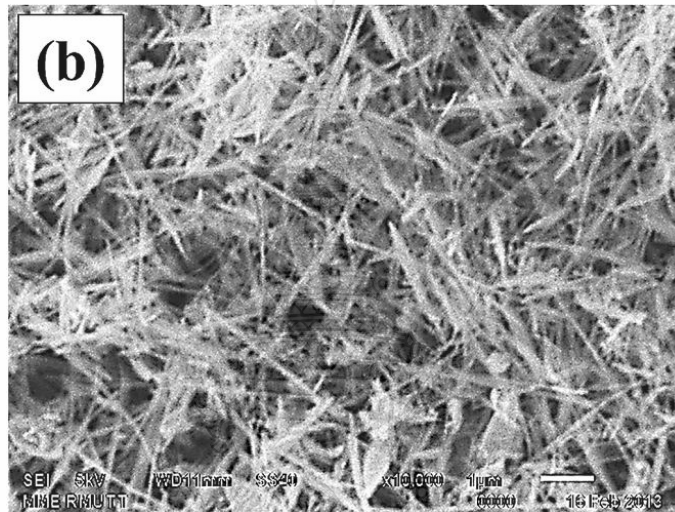
Figure 2.20 SEM image of nanofibers at x 10,000 magnified [17].
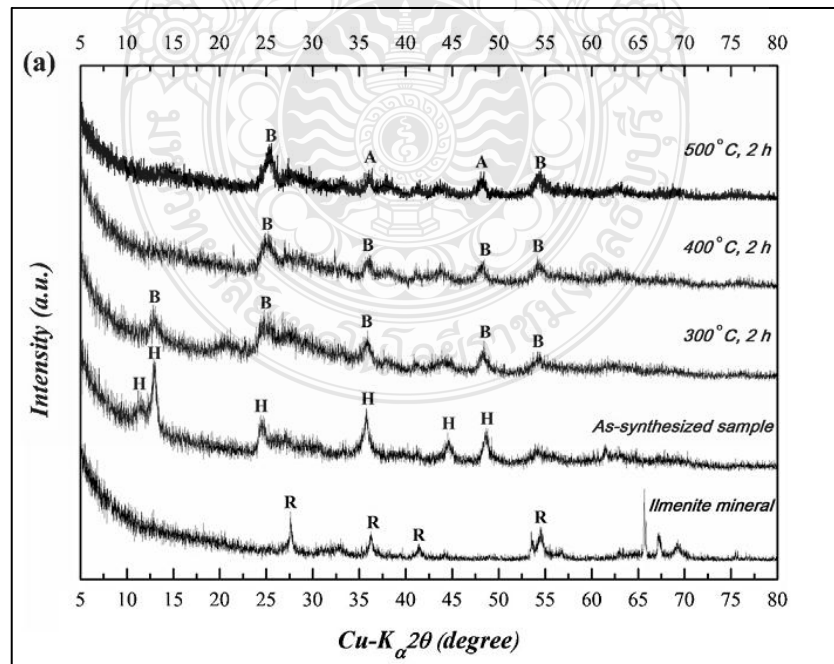
Figure 2.21 XRD patterns of nanofibers and calcined for 2 h at 100-1,000 °C [17].

34
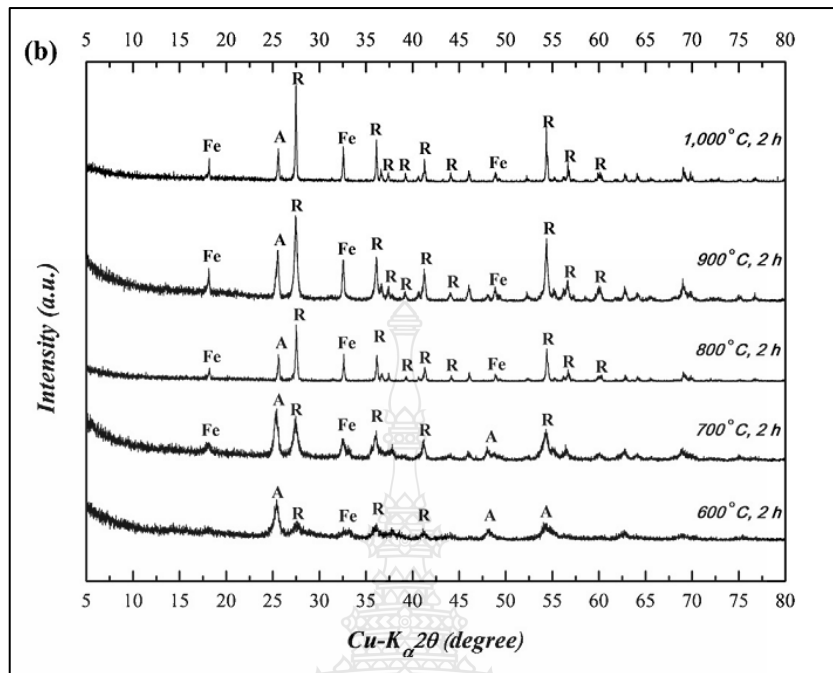
Figure 2.21 (cont.) XRD patterns of nanofibers and calcined for 2 h at 100-1,000 °C
[17].
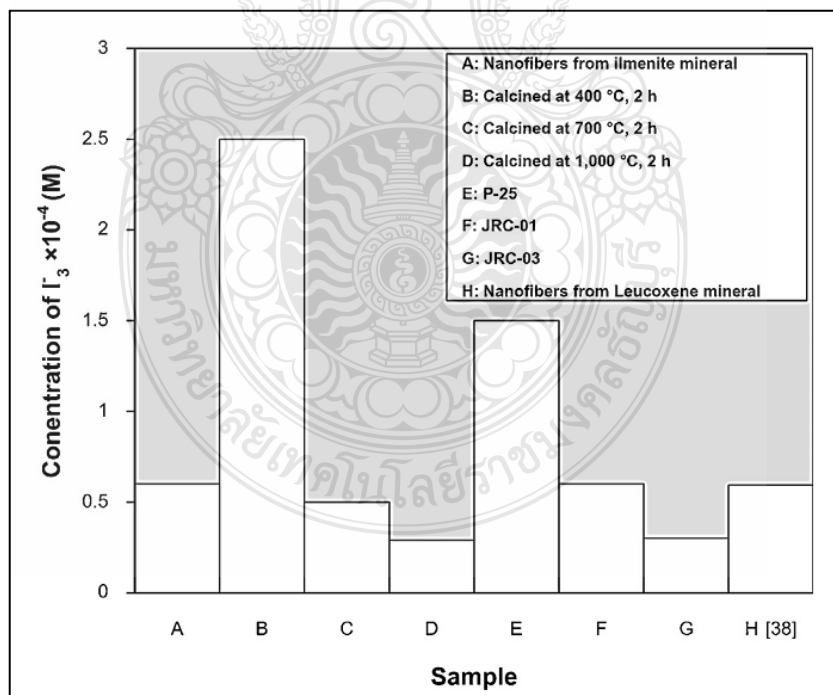
Figure 2.22 Photocatalytic activity of nanofibers, calcined nanofibers and commercial
nanoparticles TiO$_2$ [17].

Pavasupree, S. et al. [71] study of mesoporous anatase TiO_2 nanopowder synthesize by hydrothermal method at 130 °C for 12 h. The specific surface area BET about 193 m^2/g and average pore diameter 3-4 nm (Figure 2.23). The anatase TiO_2 showed photocatalytic activity higher than the nanofibers TiO_2 mesoporous TiO_2, nanorods TiO_2, and commercial TiO_2 nanoparticles (P25, JRC-03, and JRC-01) (Figure 2.24). In dye-sensitized solar cells application, the dye-sensitized solar cells efficiency of the cell using P-25 as working electrode was about 5.82%. while the mesoporous anatase TiO_2 showed efficiency about 6.30% (Figure 2.25).
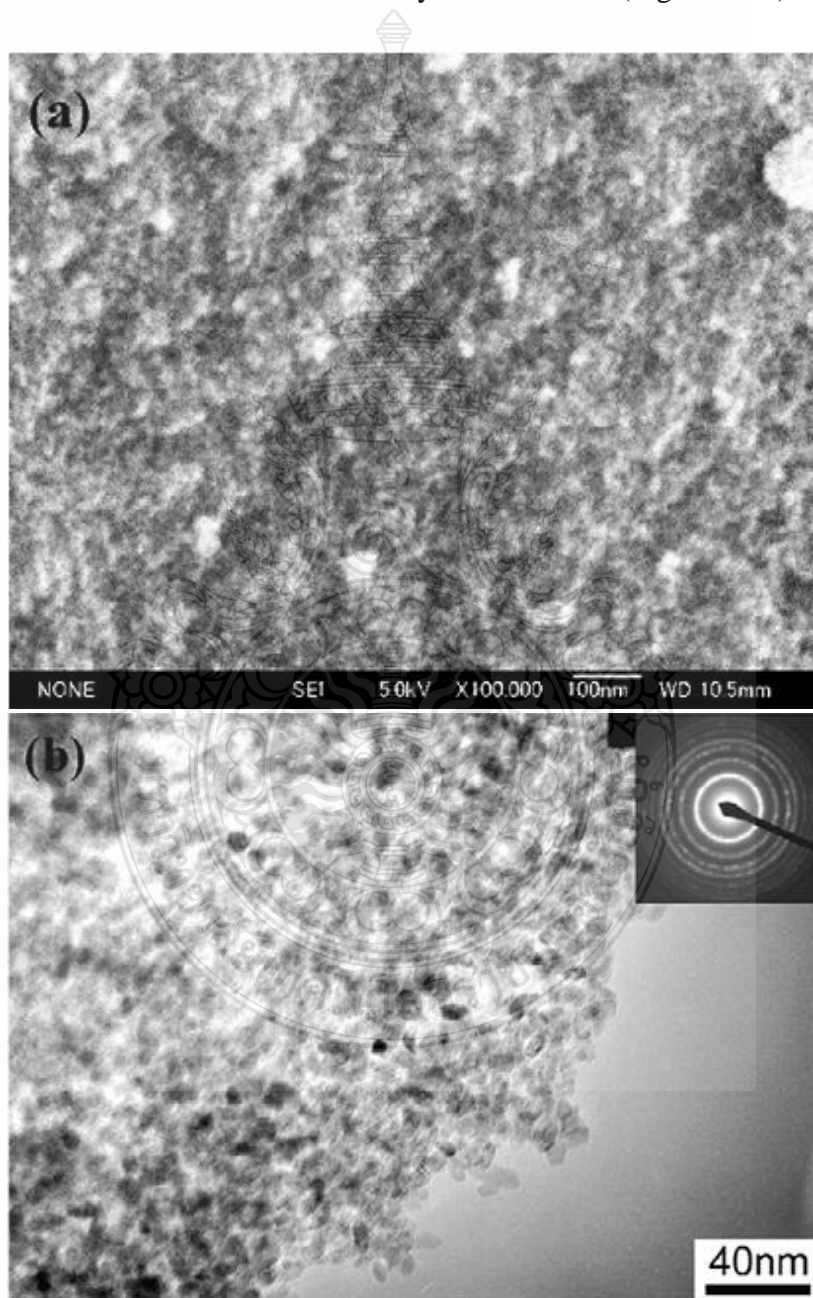
Figure 2.23 (a) SEM and (b) TEM images of mesoporous anatase TiO_2 nanopowder [71].
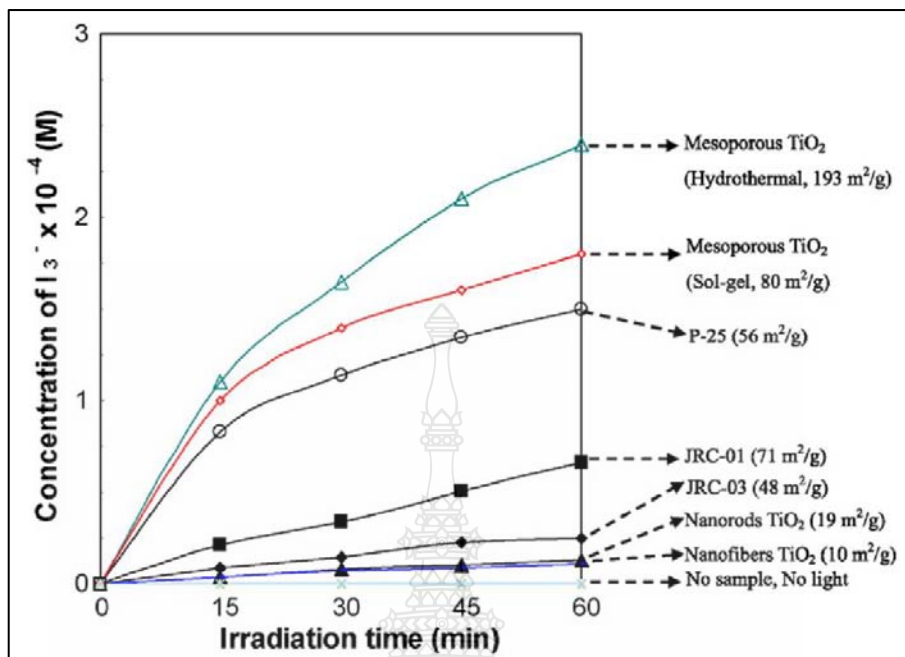
Figure 2.24 Photocatalytic activity of mesoporous anatase TiO_2 nanopowder and commercial nanoparticles TiO_2[71].
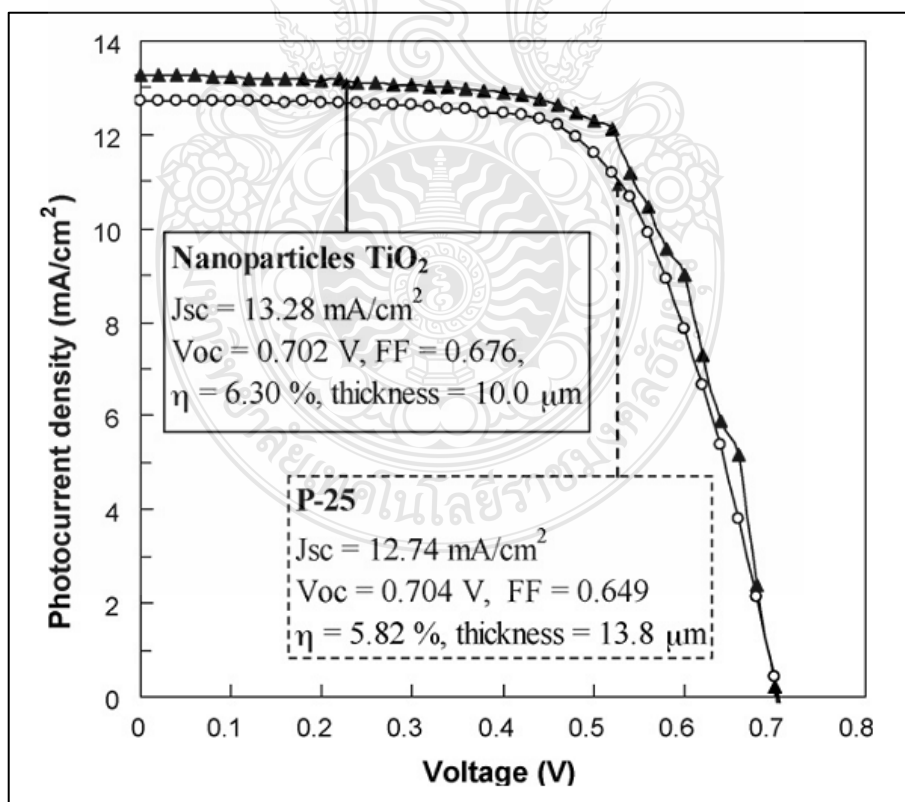
Figure 2.25 The dye-sensitized solar cells efficiency of mesoporous anatase TiO_2 nanopowder and commercial nanoparticles TiO_2 [71].

Jitputti, J. et al. [72] study of nanocrystalline mesoporous for photocatalytic activity to water-splitting application. The resultant show the crystalline size of as-synthesized is 8 nm (Figure 2.26) narrow pore size distribution and high specific surface area of 215 m^2/g (Figure 2.27). The calcined nanocrystalline mesoporous at 500 °C show high photocatalytic H_2 production activity than the commercial TiO_2 (Ishihara ST-01) (Figure 2.28).
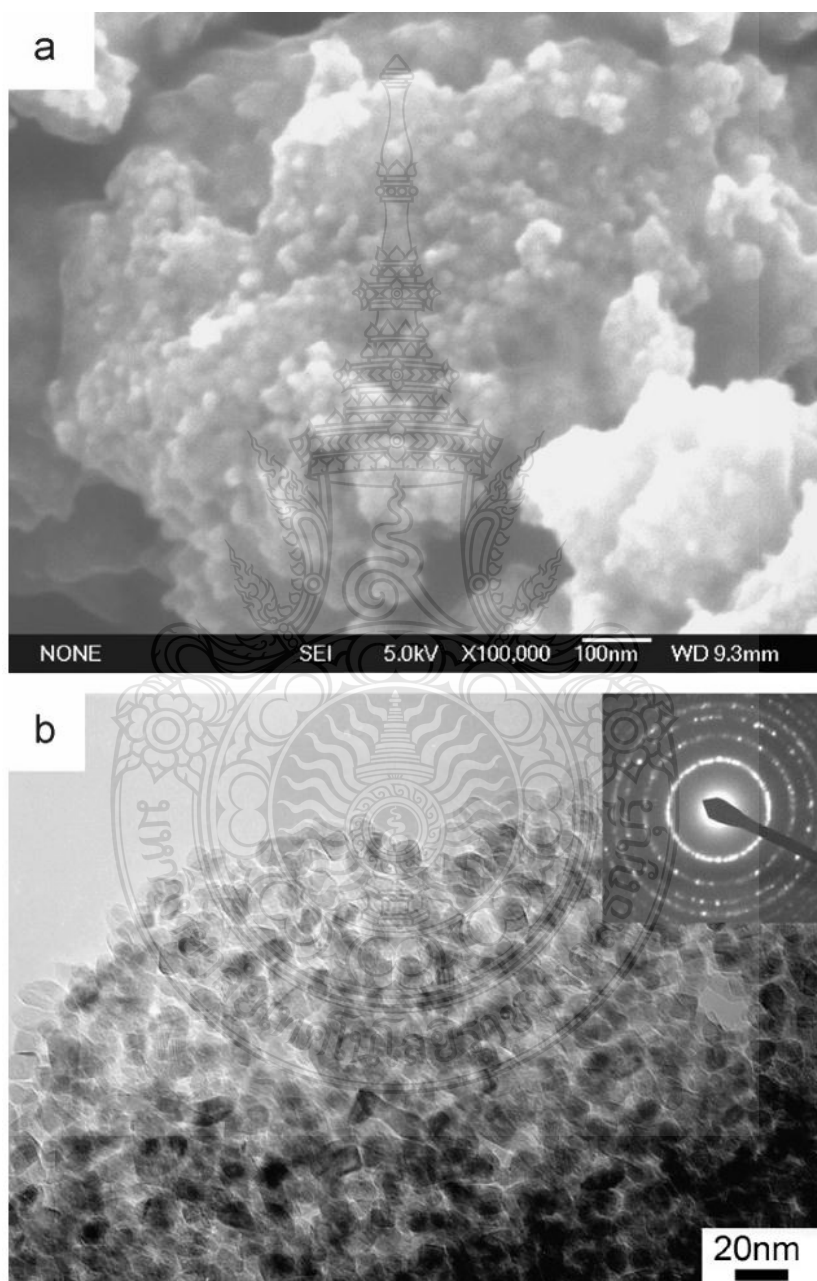
Figure 2.26 (a) SEM and (b) TEM images of nanocrystalline mesoporous TiO_2 [72].
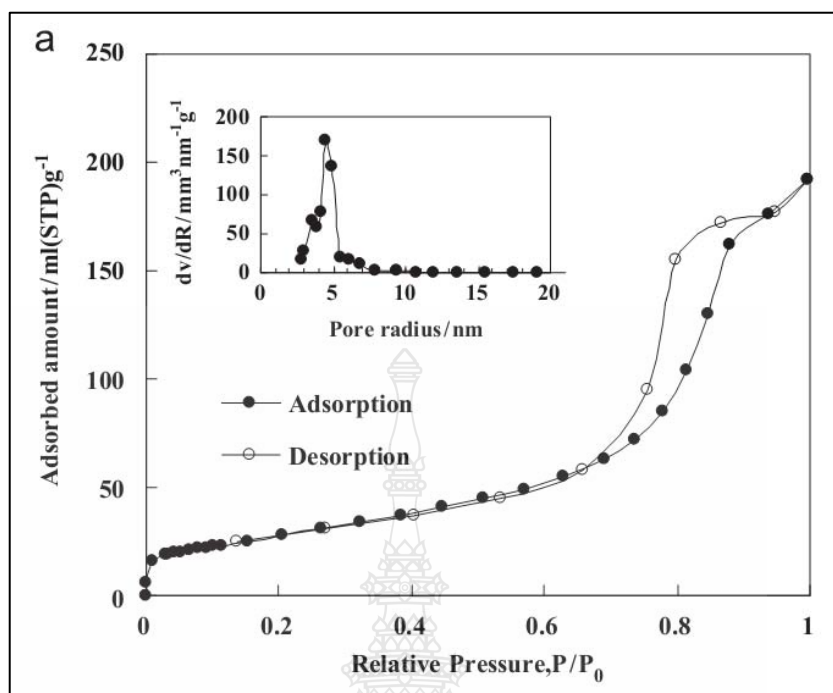
Figure 2.27 N$_2$ adsorption-desorption isotherm and pore size distribution of nanocrystalline mesoporous TiO$_2$ [72].
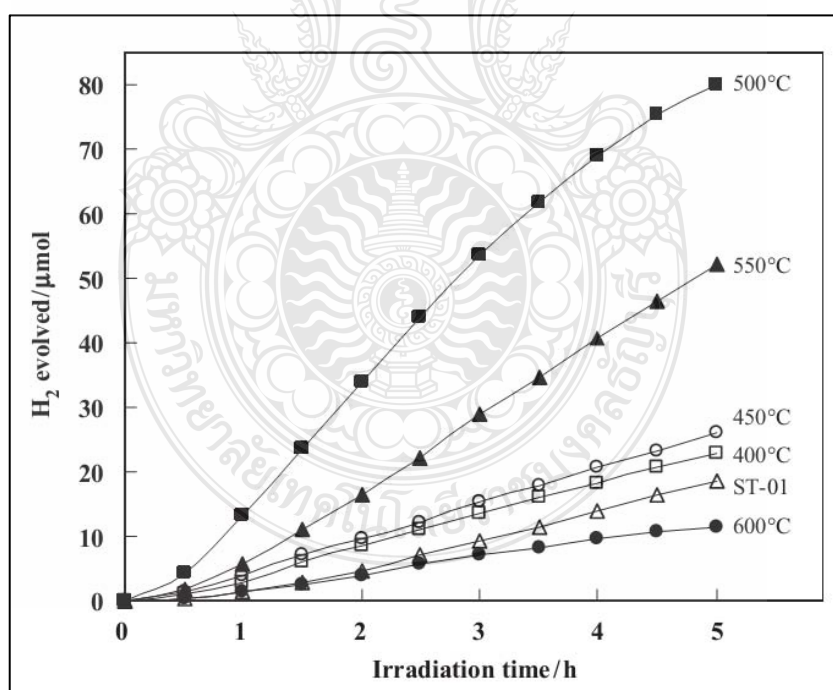
Figure 2.28 The photocatalytic H$_2$ production activity of nanocrystalline mesoporous TiO$_2$ and the commercial TiO$_2$ (Ishihara ST-01) [72].

Suzuki et al. [73] study of hydrothermal method to synthesize TiO_2 nanowire structure. The result shows after calcination heat treatment for 4 h air at 300 °C, the synthesized samples were 5-10 % nanowire/nanoparticle. Consisting of fine relatively large particles and nanowires. The composite nanowire/nanoparticle electrode showed higher dye-sensitized solar cells performance than the TiO_2 nanowire structured because high electron transfer a straightforward way is electron expressway concept (Figure 2.29).
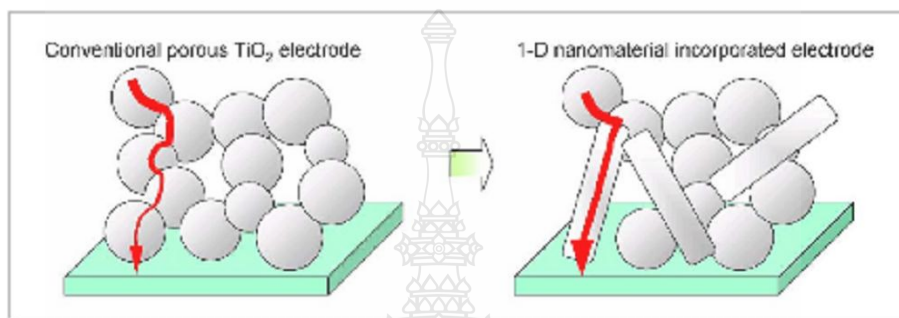
Figure 2.29 Electron expressway concept [73].

Fujian et al.[74] study of crystalline mesoporous TiO_2 self-assembly of poly 4-Vinylpyridine template and tetrabutyltitanate precursorbased under high temperature (180°C) hydrothermal conditions. The crystalline structure shows anatase phase of highly crystalline M-TiO_2-ns characters (Figure 2.30). The specific surface area about 120 m^2/g, large pore volumes about 0.34 cm^3/g and monolithic morphology with crystal sizes around 3–5 µm. The catalytic activities under UV light of M-TiO_2-ns in induced reduction of decabromodiphenyl and oxidation of Rhodamine B higher than those of M-TiO_2 template and nonporous crystalline TiO_2 compare with commercial P25 (Figure 2.31).
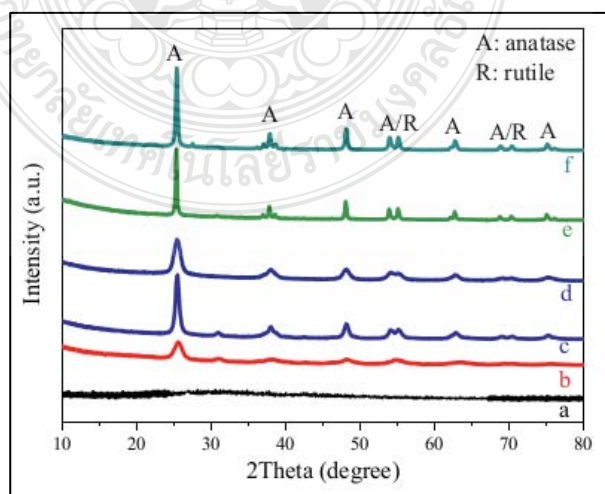
Figure 2.30 XRD patterns of crystalline mesoporous TiO_2 [74].
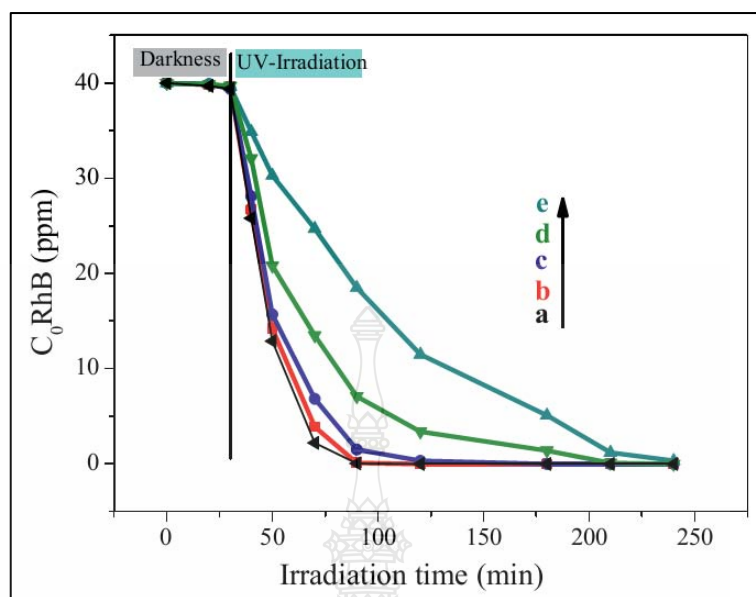
Figure 2.31 The photocatalytic activity of oxidation degradation of RhB over (a) P25,(b) M-TiO$_2$-195, (c) M-TiO$_2$-390, (d) M-TiO$_2$-F127 and (e) nonporousTiO$_2$ [74].

Taicheng An, et al.[75] study of Mesoporous TiO$_2$ photocatalysts, The resultant diameters of TiO$_2$ mesoporous structure between 13.3 and 17.0 nm and porous sizes from 9.6 to 13.3 nm. After heat treatment temperature from 450 to 650 $^\circ$C diameters of TiO$_2$ mesoporous changed from 9.8 to 18.4 nm with increase porous sizes from 8.0 to 10.0 nm (Figure 2.32). The photocatalysts activities represents a class of toxic brominated flame retardants used 2,4,6-tribrominated phenol of TiO$_2$ were depends on the structural characteristics and the phase of the resultant photocatalysts (Figure 2.33).
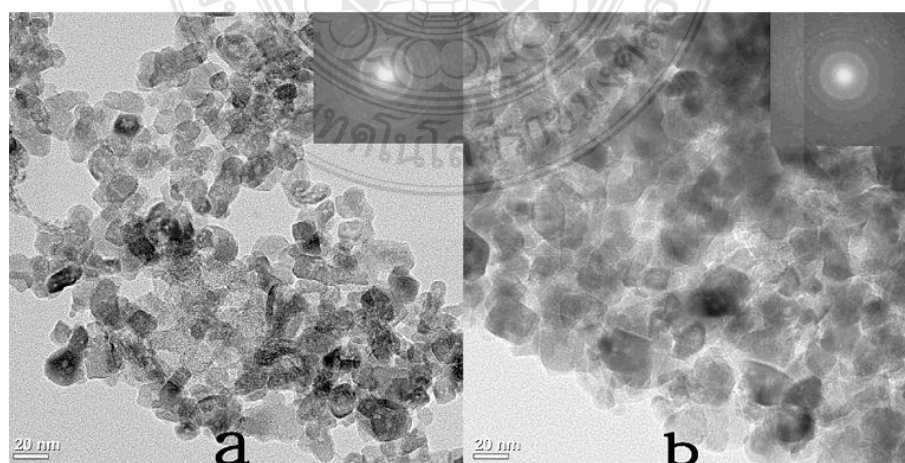
Figure 2.32 TEM images of M-TiO$_2$ with calcination at (a) 450 $^\circ$C and (b) 650 $^\circ$C [75].
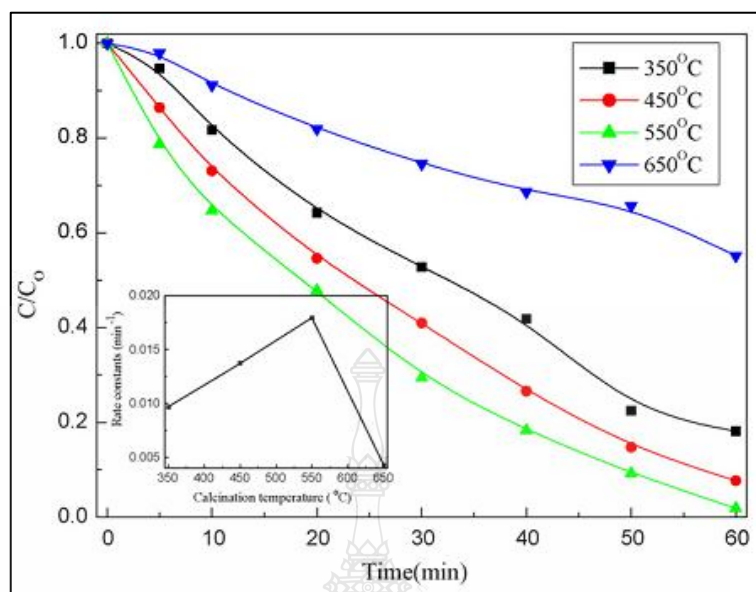
Figure 2.33 The photocatalytic activity degradation of TBP using M-TiO$_2$ with different calcination temperatures [75].

Huajun et al. [76] study of synthesize Metal-ions doped TiO$_2$ (M-TiO$_2$) for photocatalytic activity by hydrothermal method. The resultant photocatalytic activity performances of M-TiO$_2$, the manganese-ions doped TiO$_2$ (Mn-TiO$_2$) were highest degradation efficiency evaluated under whole solar-light irradiation (Figure 2.34) and visible-light (Figure 2.35) to degrading rhodamine b. the 3% manganese-ions doped TiO$_2$ (Mn-TiO$_2$) show highest photocatalytic activity performances because the most significant impacts of specific surface area(Figure 2.36).
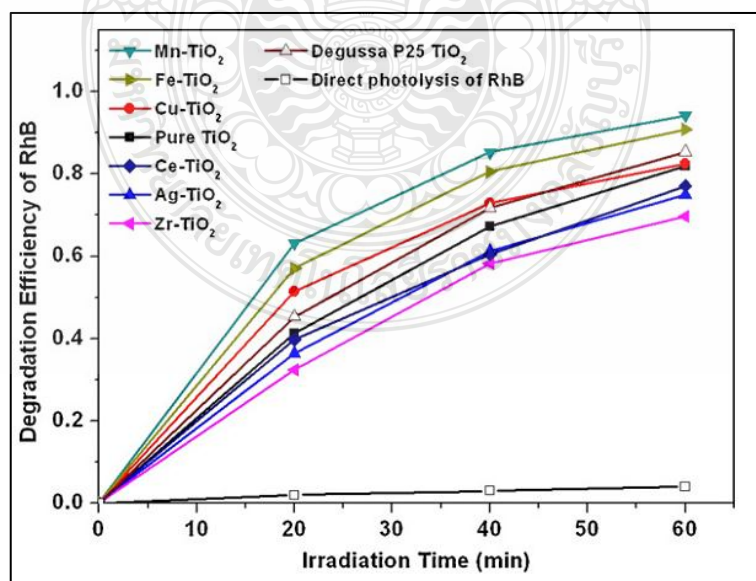
Figure 2.34 The photocatalytic activity degradation of pureTiO$_2$ and six synthesized M-TiO$_2$ under solar-light irradiation[76].

42
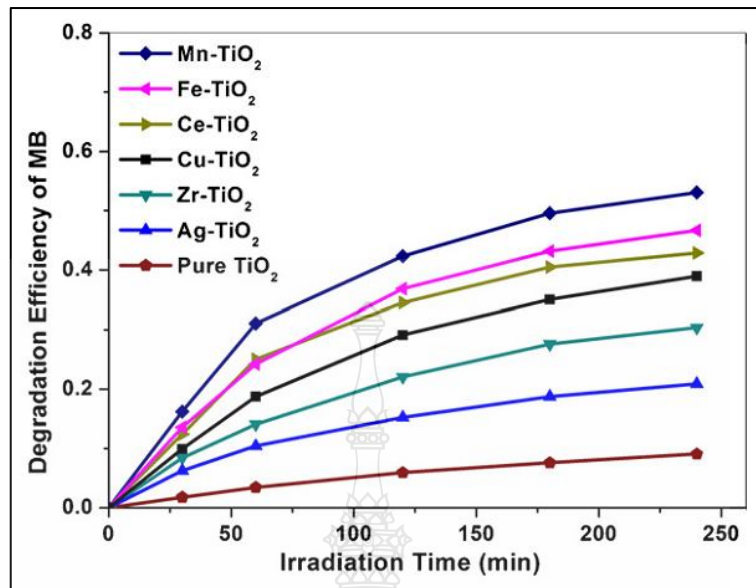
Figure 2.35 The photocatalytic activity degradation of pureTiO$_2$ and six synthesized M-TiO$_2$ under visible-light irradiation [76].
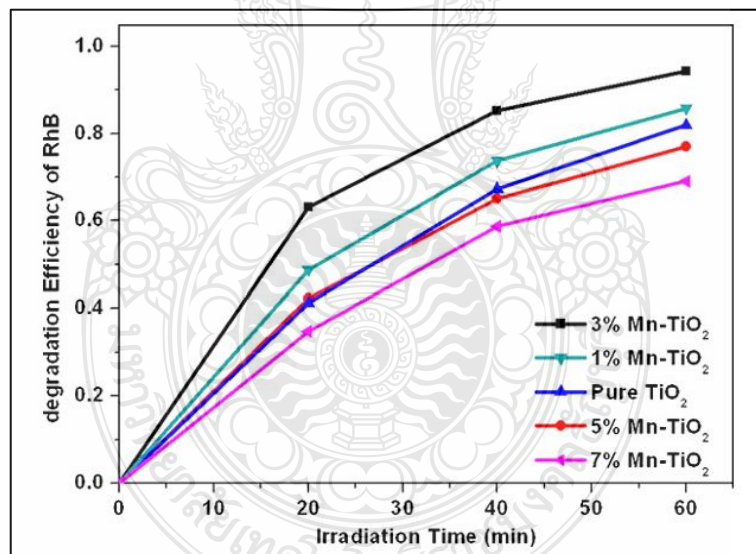
Figure 2.36 The photocatalytic activity degradation on effects of Mn doping concentrations under solar-light irradiation [76].

Lin Wan et al. [77] study of synthesize Fe-doped TiO$_2$ by hydrothermal method. The resultant photocatalytic activity of ultraviolet, visible light and Phase selection of absorption range of TiO$_2$ based materials. The ability to control particularly the competition, transformation and the structural evolution, between rutile and anatase phases. The photocatalytic activity of nano crystalline Fe-doped TiO$_2$ improved

43

significant visible light photocatalytic activity high than pure TiO_2 nanopowders in degradation effect of methylene blue (Figure 2.37).
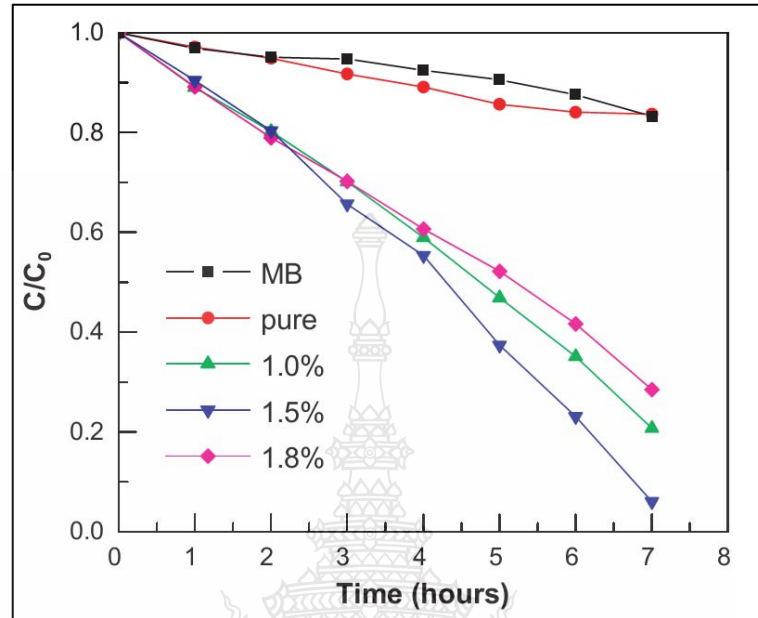
Figure 2.37 The photocatalytic activity methylene blue degradation of Fe-doped TiO_2
under visible-light irradiation [77].

      Xue Li et al. [78] study of photocatalytic activity synthesize of the nanopaticles TiO_2, Fe-TiO_2 single-doped and N-TiO_2 Fe-TiO_2 co-doped TiO_2 synthesized by hydrothermal method at 150 °C. The resultant crystalline structure for co-doped TiO_2 shows anatase phase. The N-TiO_2 Fe-TiO_2 co-doped TiO_2 specific surface area about 201 m^2/g. The Fe-TiO_2, N-TiO_2 and P-25 (Degussa) specific surface area are 150, 128 and 55 m^2/g respectively. The photocatalytic activity of methyl orange degradation co-doped TiO_2 was higher than un-doped TiO_2 and P-25 under visible-light irradiation (Figure 2.38).
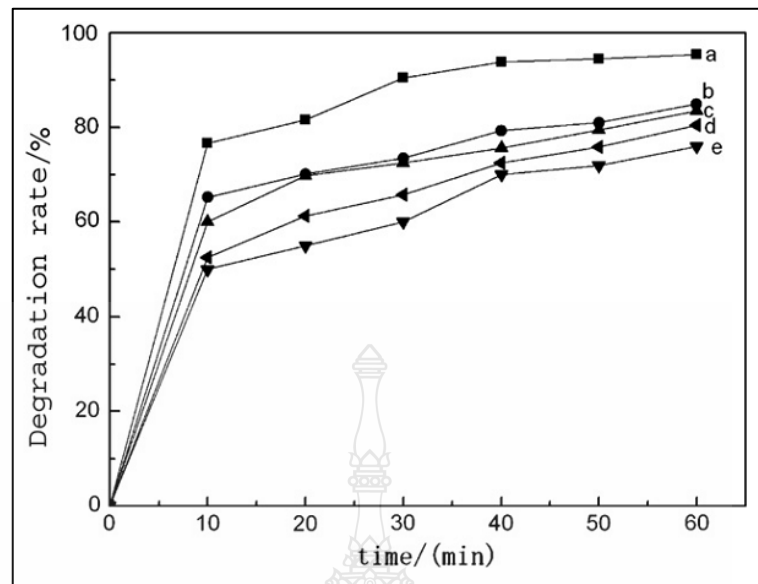
Figure 2.38 The photocatalytic activity methyl orange degradation of (a) N -Fe-TiO$_2$,(b) Fe-TiO$_2$, (c) N- TiO$_2$, (d) P-25 (Degussa) and (e) TiO$_2$ [78].

Swati Sood et al. [79] study of the concentrations of Fe doped nanoparticles TiO$_2$ in photocatalytic degradation. The results show crystals shape TiO$_2$ is smaller than dope Fe iron. The TiO$_2$ are grey particles, the Fe dopant is dark particle (Figure 2.39). The Fe iron dope nanoparticles TiO$_2$ to photocatalytic degradation for harmful chemical, para nitro phenol and toxic of 0.05 mol % Fe^{3+} can degradation 92% para nitro phenol in 5 h (Figure 2.40).
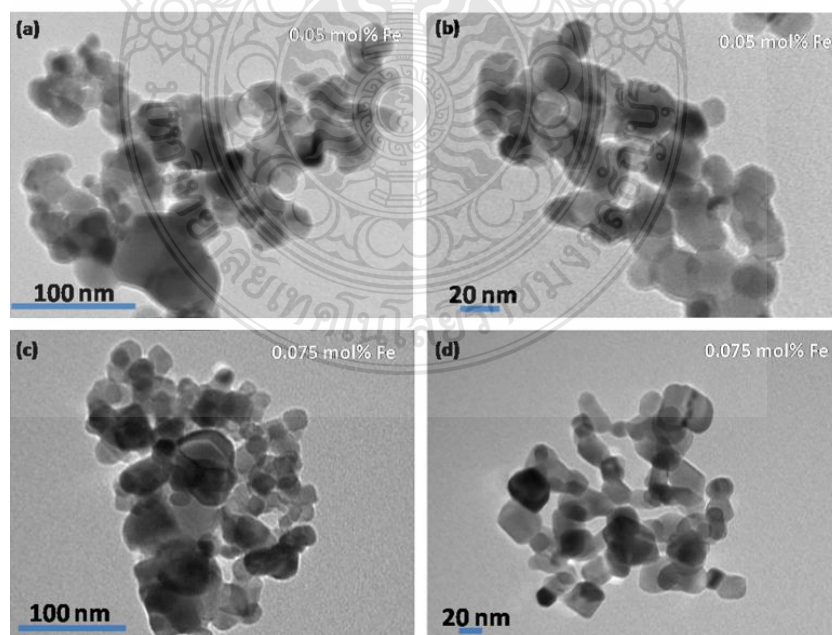
Figure 2.39 TEM images of Fe iron dope nanoparticles TiO$_2$ [79].
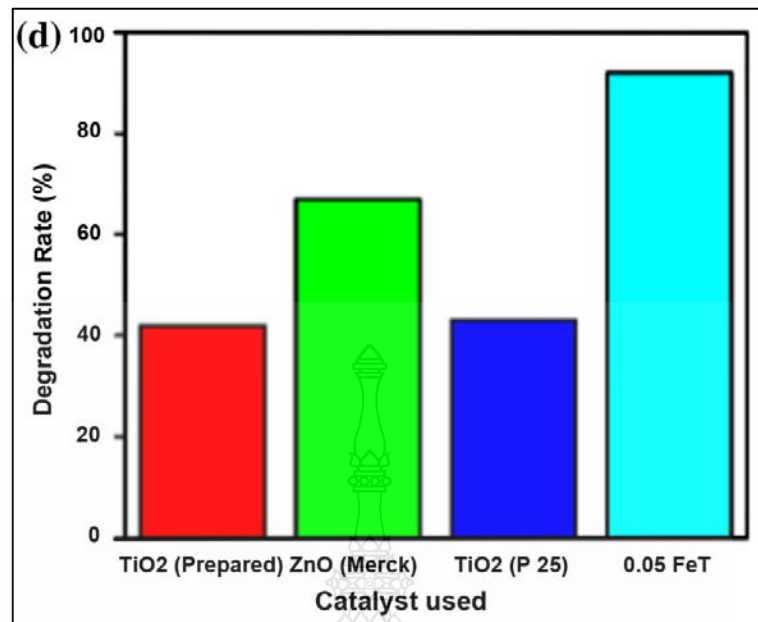
Figure 2.40 The photocatalytic activity para nitro phenol degradation of Fe iron dope nanoparticles TiO_2 [79].

Panbo Liu et al. [80] study of electromagnetic wave absorption properties of graphene @ Fe_3O_4@PANI decorated with TiO_2 nanosheets. The graphene @ Fe_3O_4@PANI decorated with TiO_2 nanosheets are prepare by hydrothermal method and in situ polymerization. The results show the TiO_2 nanosheets are disperse random orientation and form hierarchical structures on the top of grapheme @ Fe_3O_4@PANI (Figure 2.41). Electromagnetic (EM) wave absorption properties of grapheme @Fe_3O_4@PANI@ TiO_2nanosheets containing50wt% paraffin were investigated on the frequency of 2 - 18 GHz. The maximum reflection loss of the nano composites is up to -41.8 dB at 14.4 GHz of a thickness of 1.6 mm, and the absorption bandwidth of $R_L < -$10 dB is almost up to 3.5 GHz (Figure 2.42).
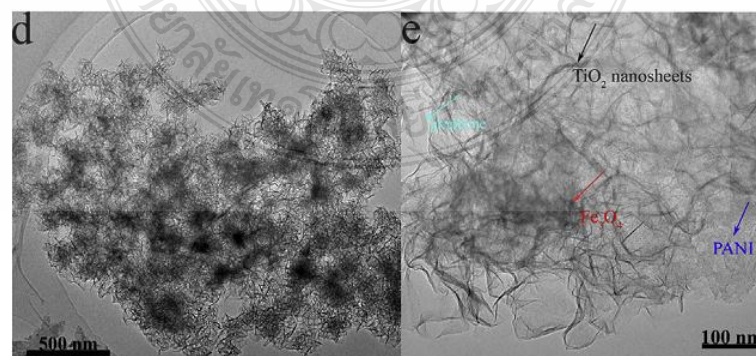
Figure 2.41 TEM images of GN@Fe_3O_4@PANI@TiO_2 nanosheets [80].
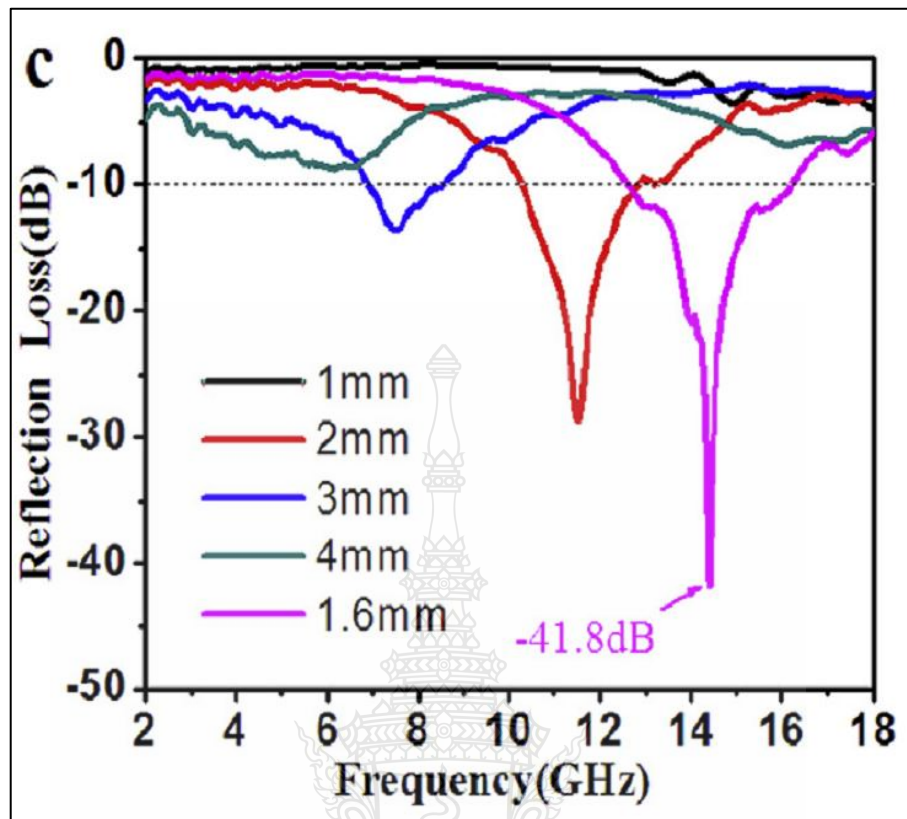
Figure 2.42 Electromagnetic (EM) wave absorption properties of graphene @ Fe$_3$O$_4$ @ PANI @ TiO$_2$ nanosheets[80].

Meng Zong et al. [81] study of microwave absorbing applications in coated Fe$_3$O$_4$ composite to grapheme oxide (RGO) composite. The TEM images show Fe$_3$O$_4$ grapheme oxide (RGO) composite, the Fe$_3$O$_4$ particle size is 15-25 nm(Figure 2.43). The microwave absorbing applications of RGO/Fe$_3$O$_4$ composite with the thickness of 3.9 mm shows the microwave absorption of − 44.6 dB at 6.6 GHz (Figure 2.44).

47
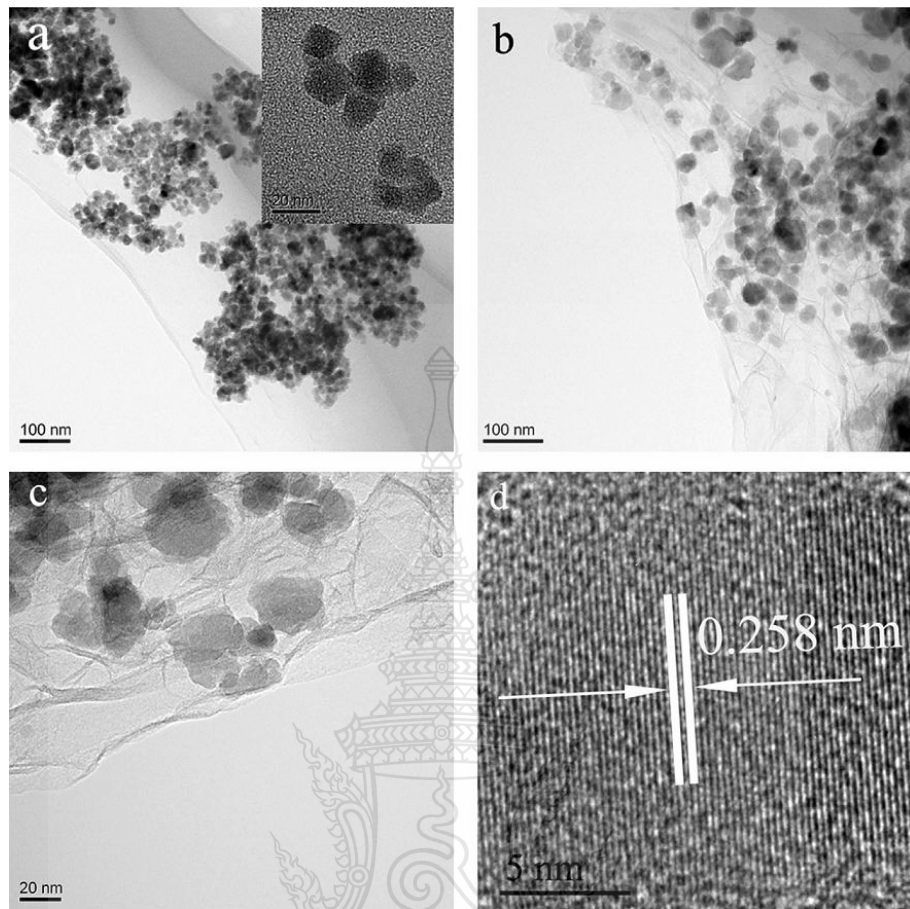
Figure 2.43 TEM images of Fe_3O_4 grapheme oxide (RGO) composite [81].
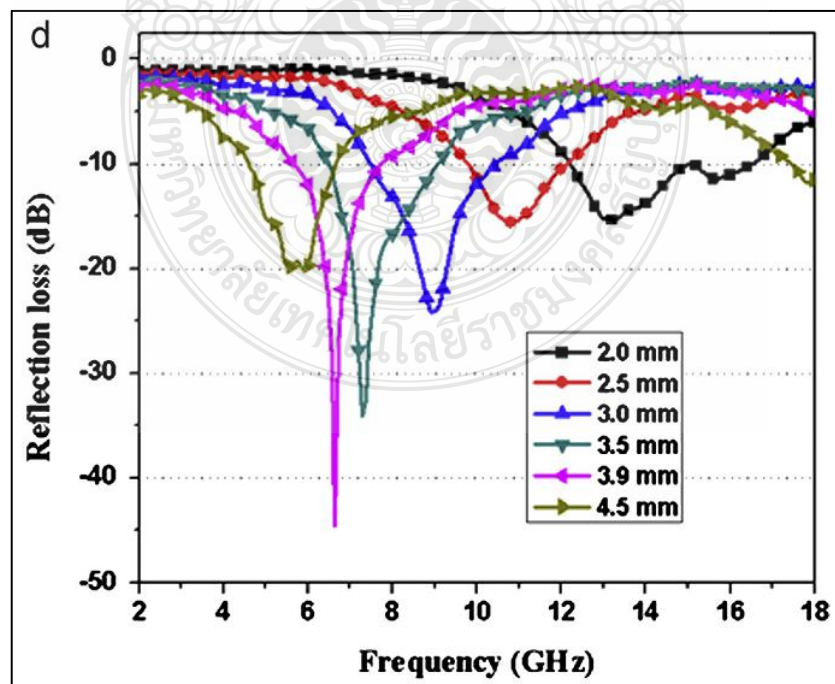
Figure 2.44 The microwave absorbing applications of RGO/Fe_3O_4 composite [81].

Kangle, Lv. et al. [82] study of calcination and photocatalytic activity of anatase TiO_2 nanosheets with hydrothermal method used tetra butyl titanate for starting material. The SEM images of the calcination of the sample show morphology is sheet shape and length about 100 nm (Figure 2.45). The photocatalytic activity decrease when increase temperature in calcination because specific surface area decrease when increase temperature in calcination (Figure 2.46).
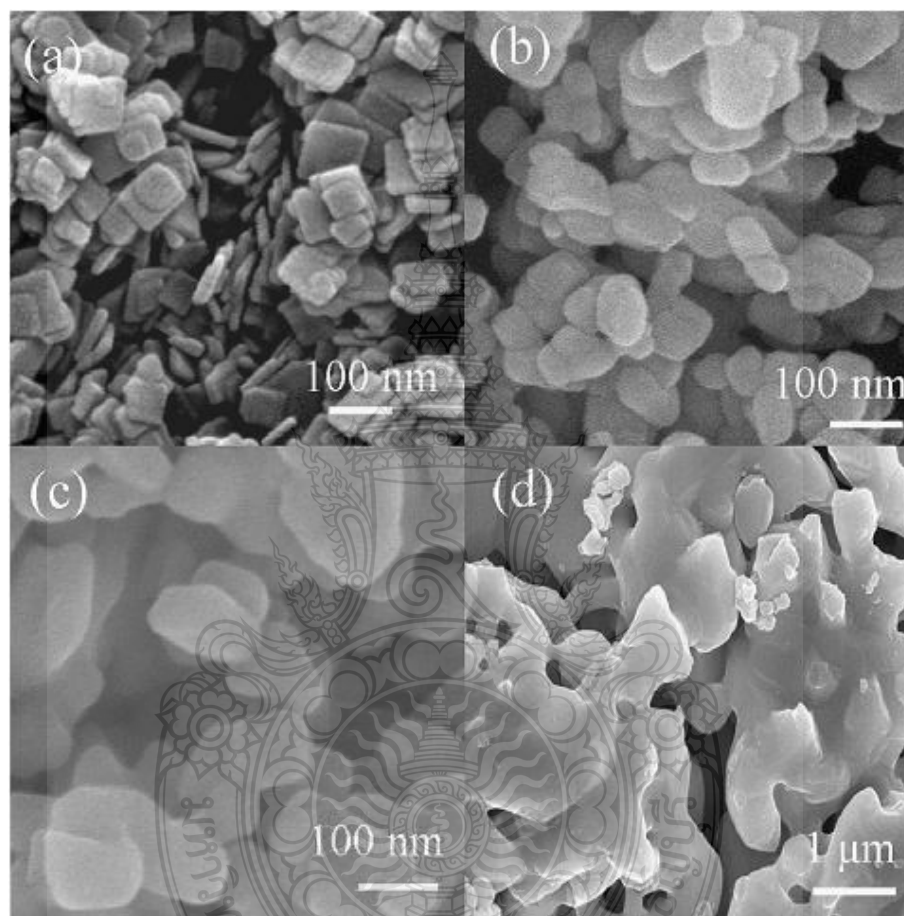
Figure 2.45 SEM images of (a) T200, (b) T800, (c) T1100, (d) T1250 [82].
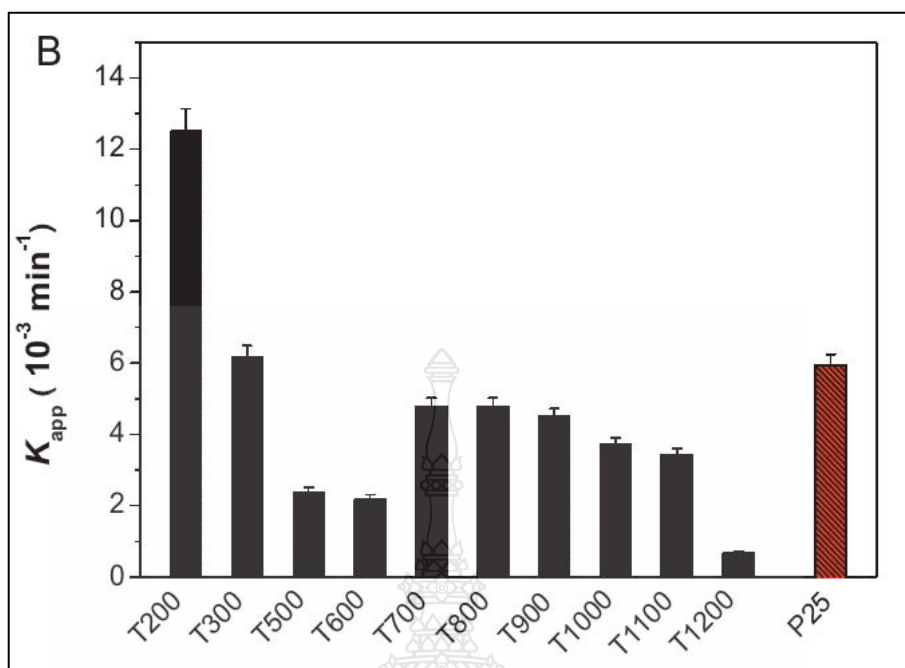
Figure 2.46 The photocatalytic activity of anatase TiO_2 nanosheets [82].

Wu J.M. et al. [83] study of dye effluent treatments with hydrothermal method used Ti (IV) ions for starting material. The titania microspheres are aggregate of nanowires diameter about 2 μm (Figure 2.47). The specific surface area were 45.4 m^2/g .The Photo degradation activity of rhodamine B were higher than P25 titania nanoparticles (Figure 2.48).
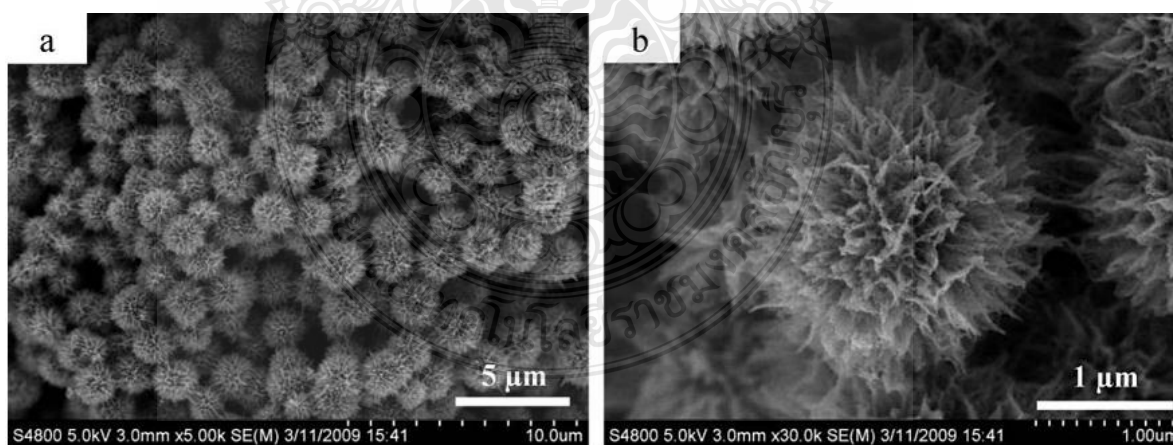
Figure 2.47 SEM images of titania microspheres[83].
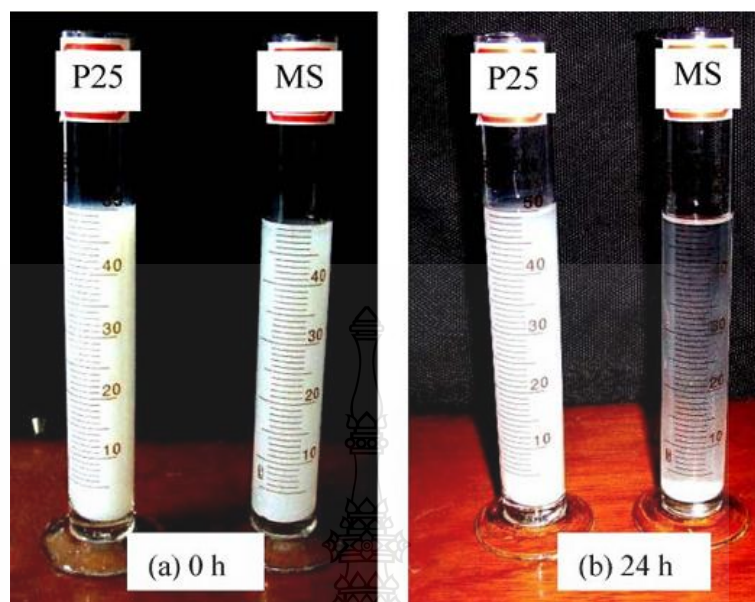
Figure 2.48 The photocatalytic activity rhodamine B degradation of titania microspheres [83].

Huang H. et al [84] study of TiO$_2$–B nanosheets for lithium-ion batteries with hydrothermal method used TiCl$_3$ aqueous solution for starting material. The resultant the flower-like porous TiO$_2$– B specific surface area were 214.6 m^2/g. the TiO$_2$– B material exhibits high capacity, good cycling stability and superior rate capability as LIBs anode materials (Figure 2.49).
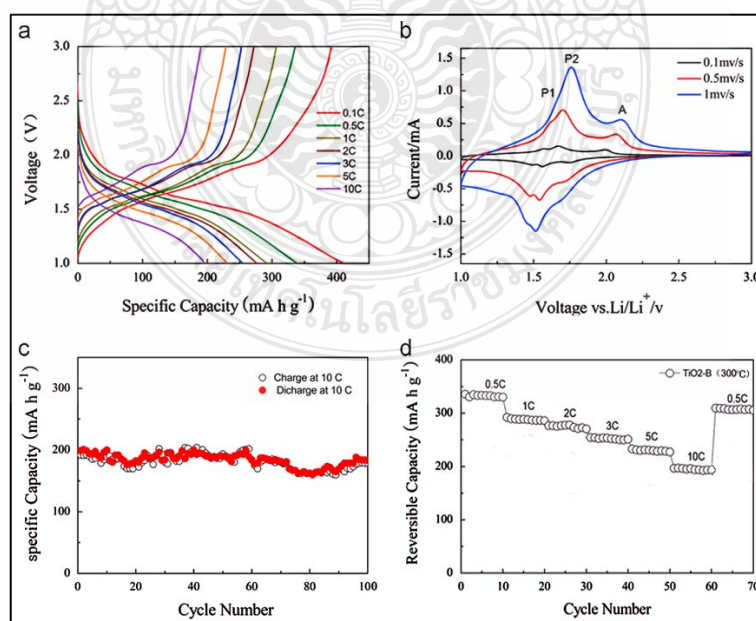
Figure 2.49 The lithium-ion batteries application of TiO$_2$–B nanosheets [84].

Chen K. et al. [85] study of the TiO$_2$ photocatalytic activity nanosheets to with hydrothermal method used Tetrabutyl titanate (98%) for starting material. The morphological of prepared is nanosheets TiO$_2$ (Figure 2.50). The photocatalytic degradation of RhB in visible light of TiO$_2$ nanosheets was higher than P25 nanoparticles (Figure 2.51).
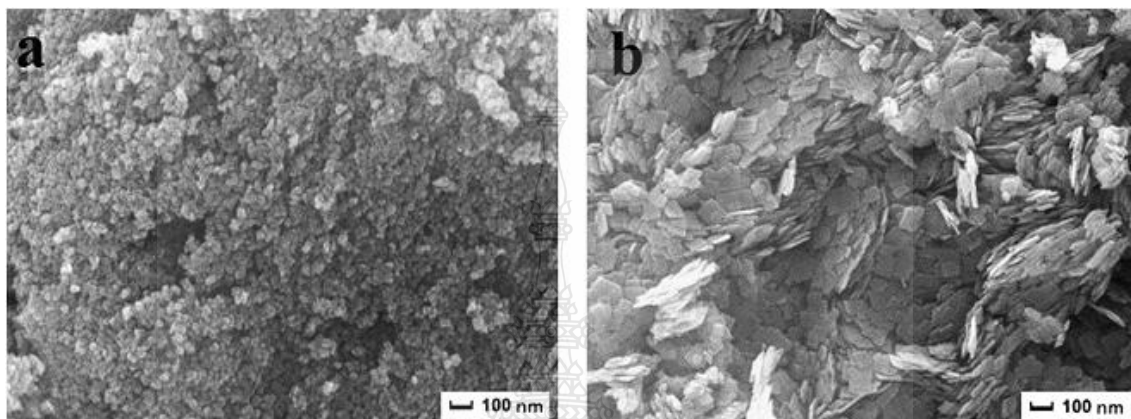
Figure 2.50 SEM images of nanosheets TiO$_2$ [85].
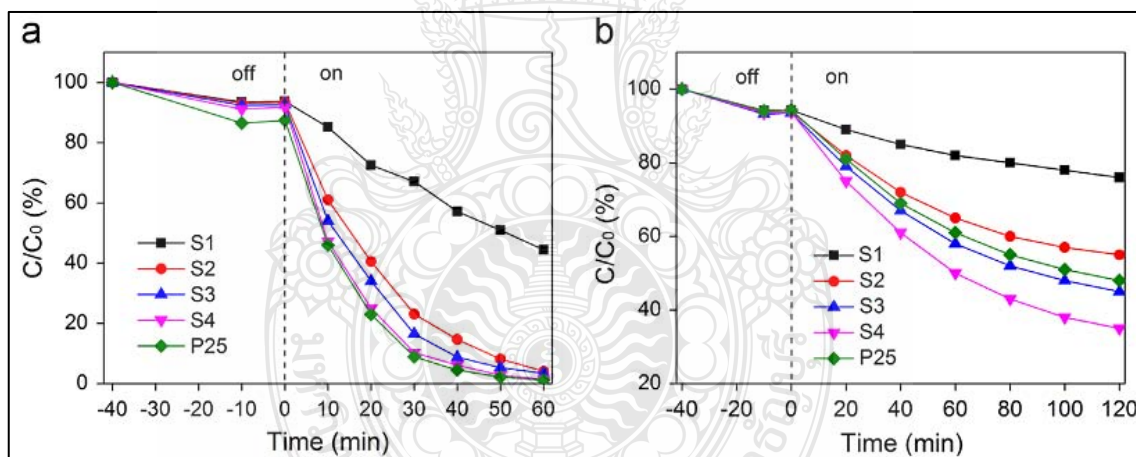
Figure 2.51 The photocatalytic activity of nanosheets TiO$_2$ under (a) UV and (b) visible light irradiation [85].

Que Y.-P. et al. [86] study of high crystalline nanosheets. The starting material is titanium isopropoxide TTIP and solution use hydro fluoric acid, polyvinyl pyrrolidone PVP, ethanol for hydrothermal method at 200 ∘C for 24 h. Next, Cool the sample to room temperature and wash with ethanol. The results show the morphology of the samples is uniform hierarchical flower-like 3D structures. The samples size is 700-800 nm thickness about 13 nm (Figure 2.52). The N$_2$ adsorption desorption isotherm show hysteresis loop type H3 and isotherms type IV. The specific surface area is 16.67 m^2/g and pores volume is 0.167 cm^3/g. The hierarchical flower-like 3D structures effect to photoelectric performance to improve electron collection efficiency,

facilitate electron transport and reduce electron recombination for dye-sensitized solar cells.
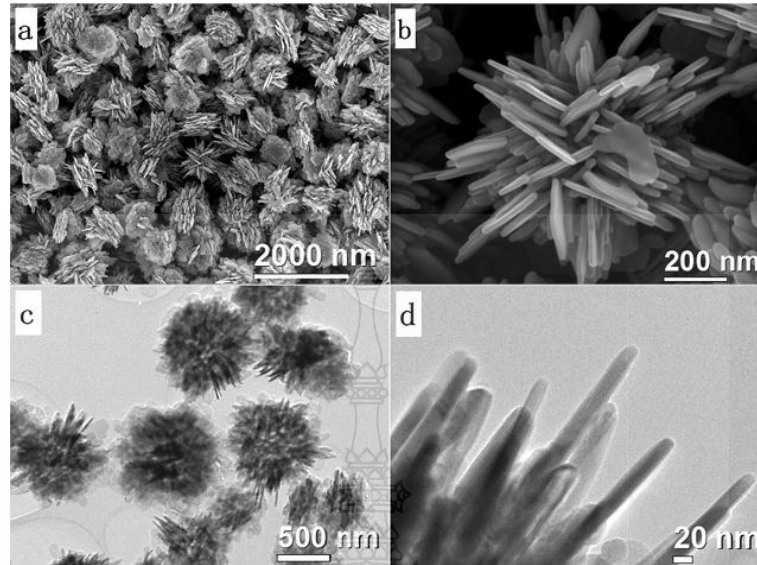
Figure 2.52 SEM images and TEM images of nanosheets [86].

Shen B. et al. [87] study of graphene oxide film and graphene foam for electromagnetic interference shielding. The graphene oxide film is prepare by evaporation of graphene oxide suspension under mild heating. The graphene foam is prepare by graphene oxide film and use hydrazine-foaming method. The results show the graphene foam high electromagnetic interference shielding in broadband frequency range of 8.2 - 59.6 GHz than the graphene oxide film. The maximum reflection loss is – 26.3 dB at 51 GHz (Figure 2.53). The graphene foam show performance competitive shielding electromagnetic broadband because porous graphene foams can repeat reflect at the cell interfaces due to the impedance between graphene layers and air can enhance transfer micro current energy to heat.
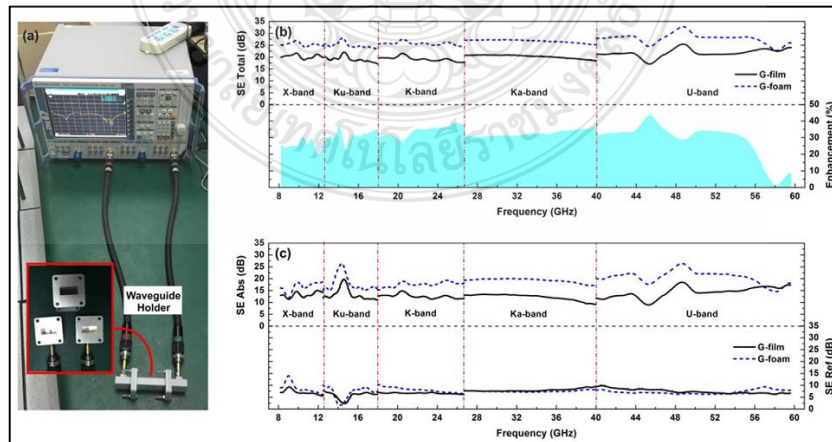
Figure 2.53 The electromagnetic interference shielding of graphene film and graphene foam [87].

Yang Y. et al. [88] study of graphene/Fe$_3$O$_4$ hydrogel for electromagnetic wave absorption. The composite hydrogels from Fe$_3$O$_4$ nanoparticles and graphene sheets are prepare by hydrothermal method. The nanoparticles Fe$_3$O$_4$ size about 13 nm and disperse randomly on the surface of the graphene sheets (Figure 2.54). The results show graphene/Fe$_3$O$_4$ hydrogel can removal Rhodamine B is 99.6%. The graphene/Fe$_3$O$_4$ hydrogel show strong and wide in the frequency range 2–20 GHz of electromagnetic wave absorption. The maximum reflection loss is −11 dB at 17.4 GHz. The composite hydrogels show organic pollutant adsorption property and electromagnetic wave absorption because high adsorption ability and the large surface area of graphene sheets and affect the magnetic properties of Fe$_3$O$_4$ materials (Figure 2.55).
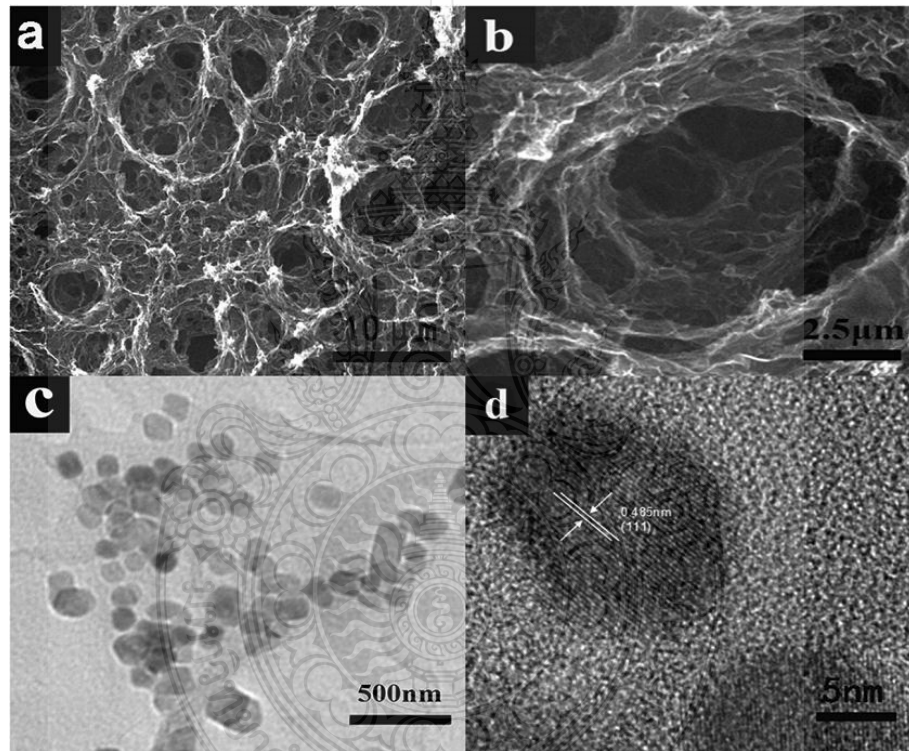
Figure 2.54 SEM images and TEM images of graphene/Fe$_3$O$_4$ hydrogel [88].
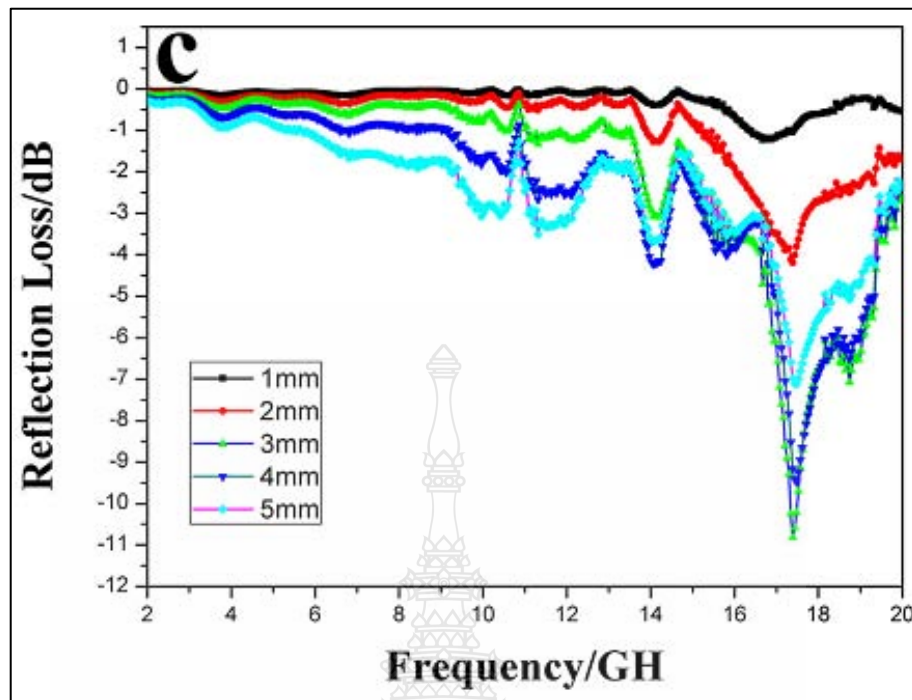
Figure 2.55 The electromagnetic wave absorption of graphene/Fe$_3$O$_4$ hydrogel [88].

Yuan, X. et al. [89] study of electromagnetic wave absorption from titanium carbide nanowires. The titanium carbide nanowires are prepared by chloride-assisted carbothermal reaction. The results show morphology and microstructure of titanium carbide nanowires have a diameter about 200–400 nm and lengths up to dozens micrometers (Figure 2.56). The specific surface areas about 186.7 m^2/g. The hybrids of titanium carbide nanowires and paraffin show electromagnetic wave absorption activity at 8.2–12.4 GHz in X-band. The sample at thickness of 1.7 mm show the maximum reflection loss is –51.0 dB at 11.8 GHz. and the bandwidth of 3.0 GHz reflection loss of < -10 dB (Figure 2.57).
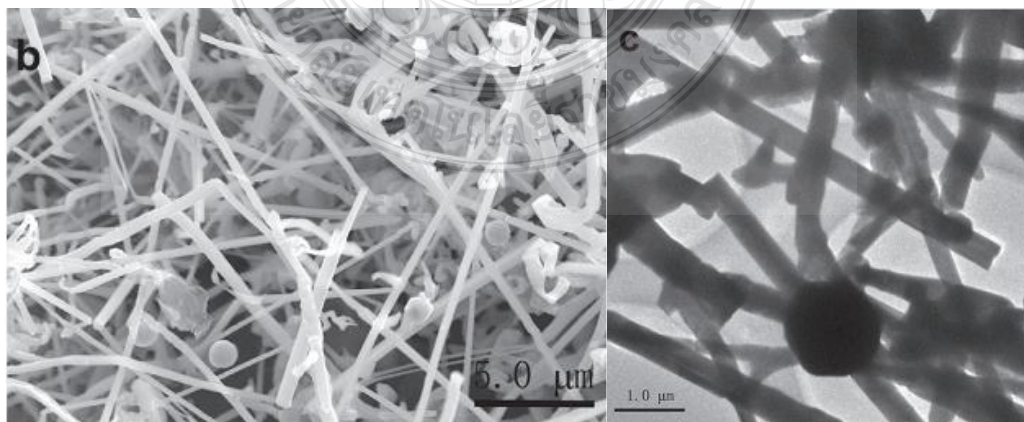
Figure 2.56 SEM images and TEM images of titanium carbide nanowires [89].
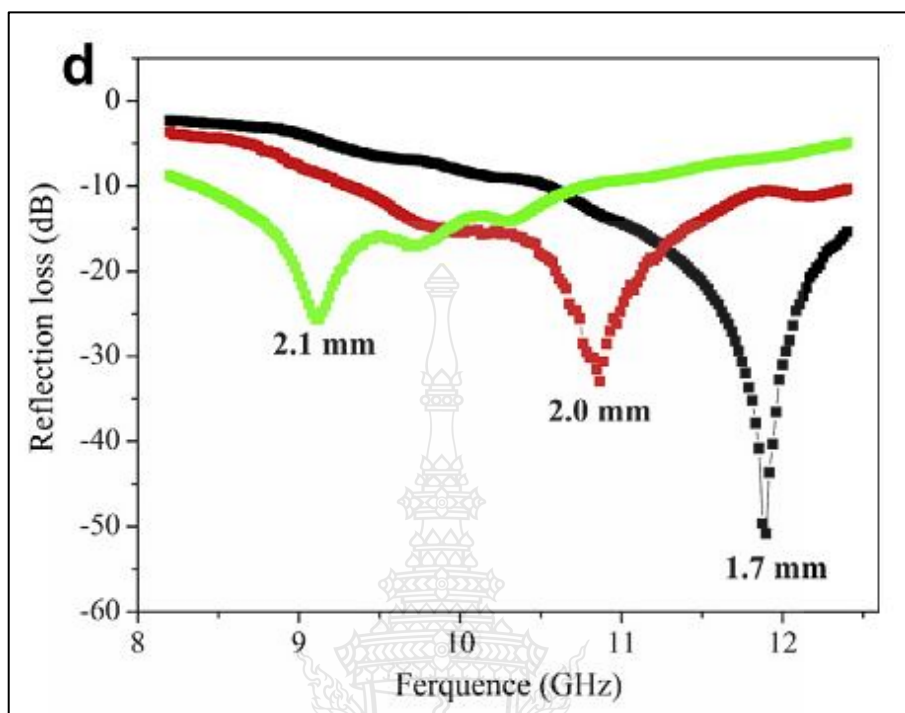
Figure 2.57 The electromagnetic wave absorption of titanium carbide nanowires [89].

Wang, H. et al. [90] study of electromagnetic interference shielding from porous polymeric composites. The porous polymeric composites three-dimensional (3D) networks are prepare by combination of hot-pressing and selective etching with poly(vinylidene fluoride)(PVDF) and multiwall carbon nanotubes (MWCNTs). The results show electrical conductivity of nano composites foam increase when the content of multiwall carbon nanotubes is 15 wt%. The electrical conductivity of pure poly(vinylidene fluoride) is 10^{-16} S/cm and the electrical conductivity of multiwall carbon nanotubes is 15 wt% is 1S/cm. The porous polymeric composites three-dimensional (3D) networks show the electromagnetic interference shielding at the frequency of 8 -12 GHZ. The shielding effectiveness is 56.72 dB at thickness about 2 mm and density of 0.79 g/cm^3 (Figure 2.58). The porous polymeric composites three-dimensional (3D) networks are electromagnetic interference shielding because the incident power reflect and scatter many times between multiwall carbon nanotubes and poly(vinylidene fluoride) interfacial areas.
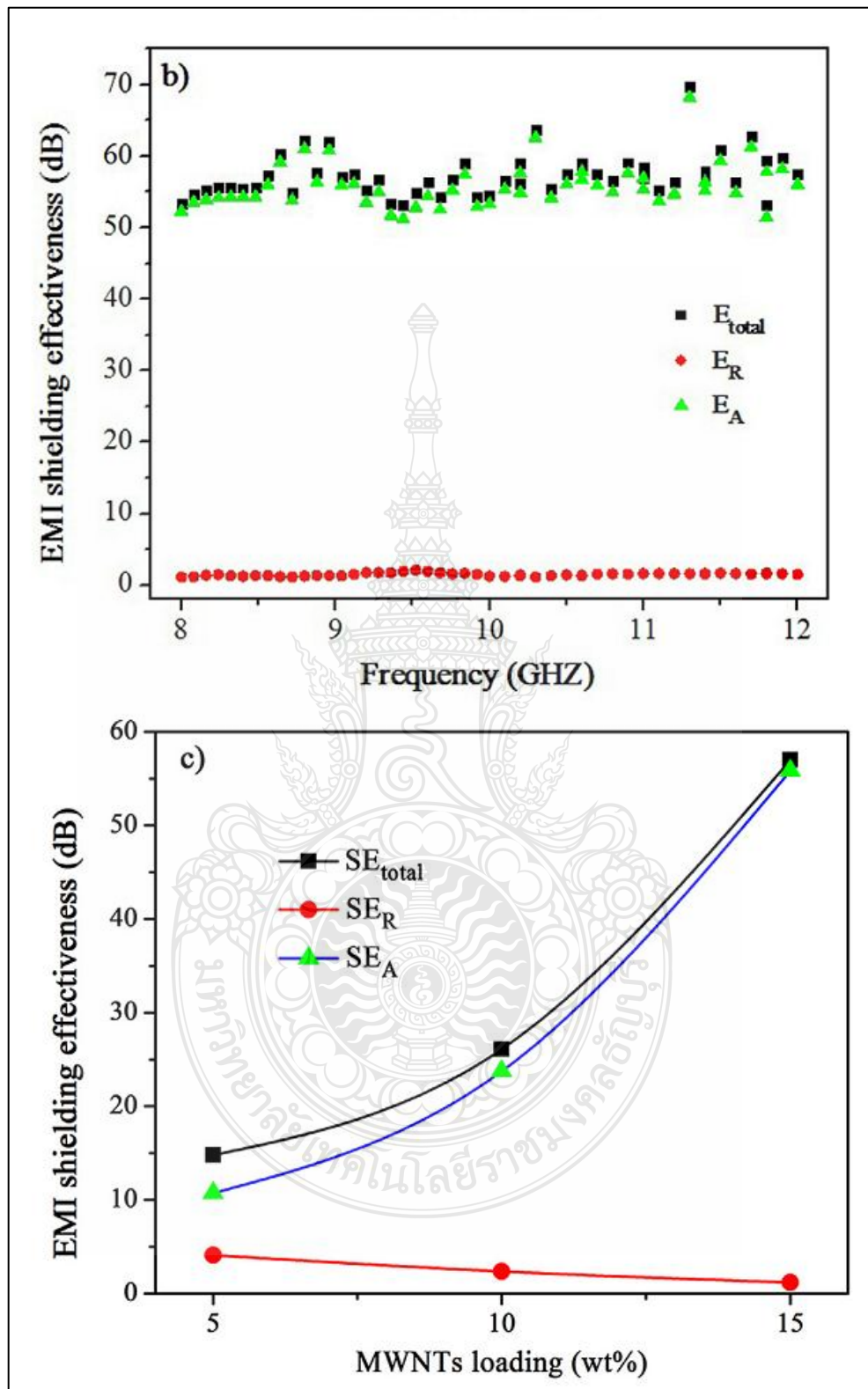
Figure 2.58 The electromagnetic interference shielding of porous polymeric composites [90].

Wang, Y. et al. [91] study of microwave absorption enhancement of Fe_3O_4 @ SnO_2/ reduced graphene oxide nanocomposite. The Fe_3O_4 @ SnO_2/ reduced graphene oxide nanocomposite are prepare by three-step hydrothermal method. The results show the diameter of Fe_3O_4 nanospheres are about 220 nm. The nanoparticles Fe_3O_4 @ SnO_2 core – shell disperse randomly on the surface of reduced graphene oxide (Figure 2.59). The electromagnetic microwave absorption show Fe_3O_4 @ SnO_2/ reduced graphene oxide nanocomposite can absorb microwave in the frequency range of 2 – 18 GHz at room temperature. The microwave absorption show The maximum reflection loss is – 45.5 dB at 6.4 GHz promising for application in microwave absorbers (Figure 2.60).
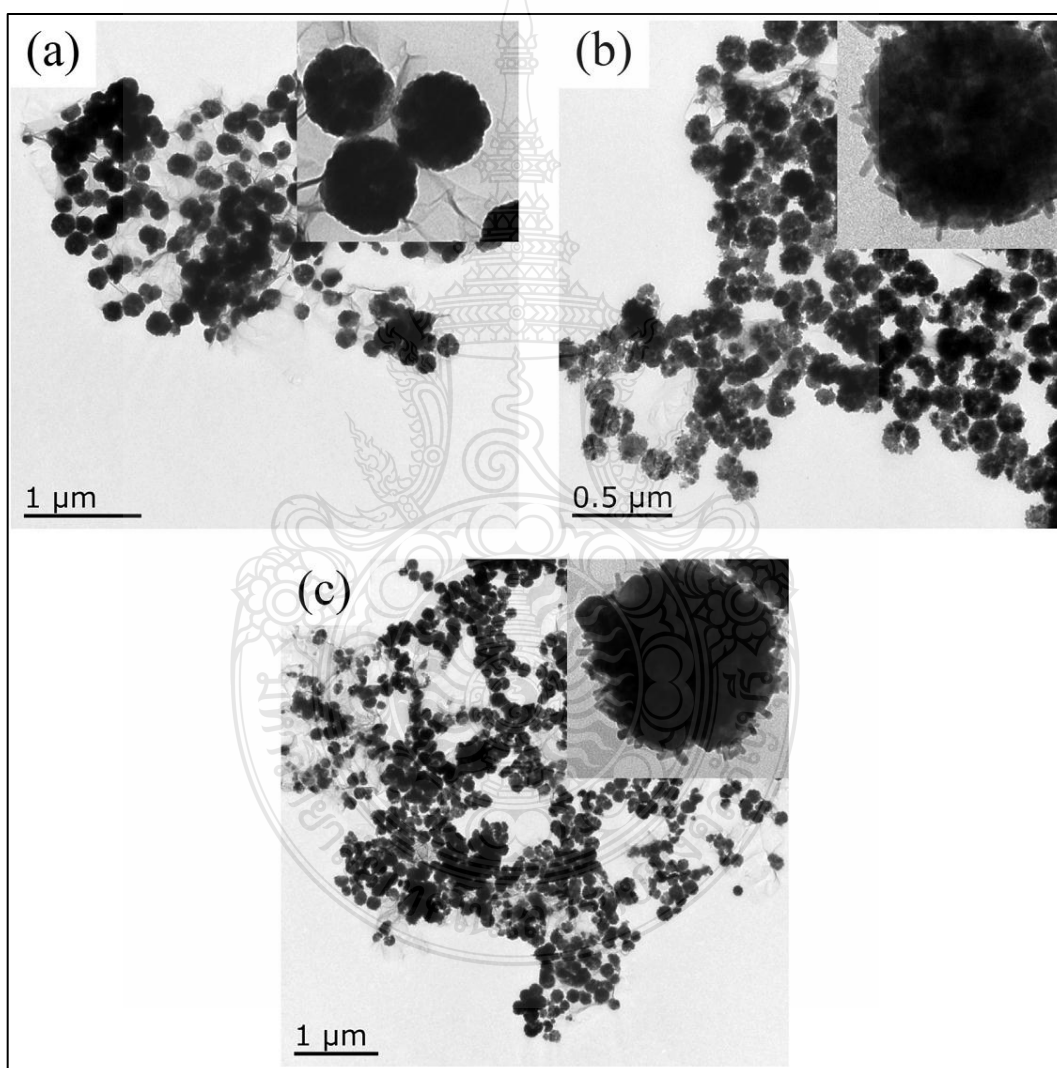
Figure 2.59 TEM images of Fe_3O_4 @ SnO_2/ reduced graphene oxide nanocomposite
        [91].
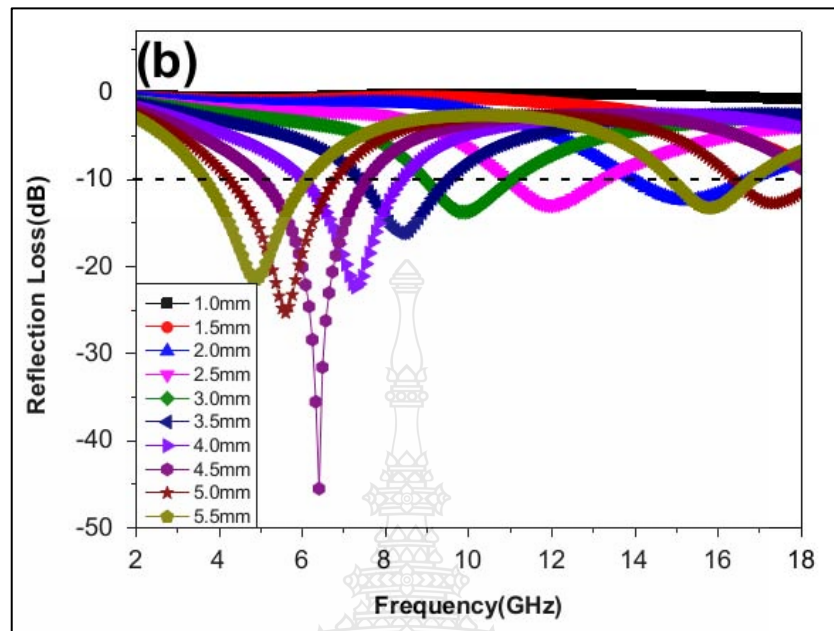
Figure 2.60 The microwave absorption enhancement of Fe_3O_4 @ SnO_2/ reduced
graphene oxide nanocomposite [91].

Yang, Z. et al. [92] study of TiO_2/Al_2O_3 ceramic for broadband electromagnetic absorbers. Rader absorbing materials are TiO_2/Al_2O_3 ceramic coatings with aluminum film. The results show TiO_2/Al_2O_3 ceramic coatings can absorb broadband electromagnetic frequency range of 8.2 -18 GHz. The maximum reflection loss on 10.6 GHz is -29 dB at the thickness of 1.7 mm from TiO_2/Al_2O_3 ceramic coatings material. The broadband electromagnetic absorbers property parameters depend on thickness period size diameter of TiO_2/Al_2O_3 ceramic coatings (Figure 2.61).
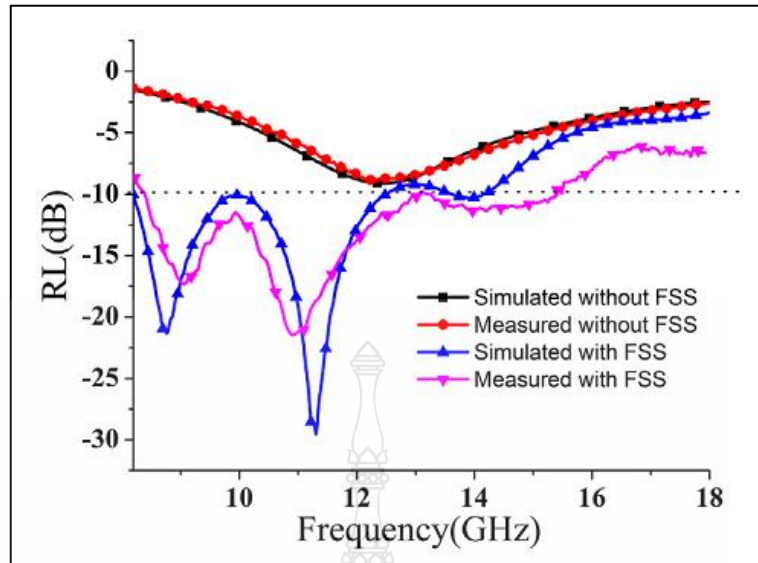
Figure 2.61 The broadband electromagnetic absorbers of TiO_2/Al_2O_3 ceramic [91].

Jia, Q. et al. [93] study of microwave absorption performance from TiO_2 /polyaniline /graphene oxide bouquet-like composites. The TiO_2 /polyaniline /graphene oxide bouquet-like composites are prepared by in-situ oxidation polymerization. The results show morphology of TiO_2 /polyaniline /graphene oxide composites are bouquet-like structures. The microwave absorption performance in the bandwidth absorption in the frequency range of 7.97 -11.88 GHz show the reflection loss is -51.74 dB from TiO_2 /polyaniline /graphene oxide composites at the frequency 9.67 GHz with the thickness of 3.12 mm (Figure 2.62).
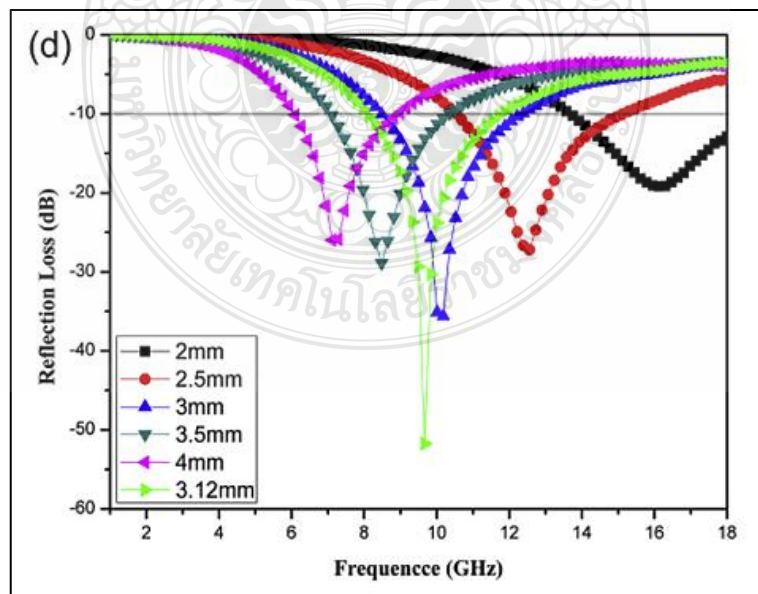
Figure 2.62 The microwave absorption performance of TiO_2 /polyaniline /graphene oxide bouquet-like composites [93].

60

Lu, L. et al. [94] study of electromagnetic wave absorbing application in concrete from TiO_2. The TiO_2 containing function aggregate electromagnetic wave absorber is preparing by disperse powder TiO_2 into clay and calcined. The results show the TiO_2 containing function aggregate electromagnetic wave absorber has high dielectric constant. The TiO_2 containing function aggregate electromagnetic wave absorber can absorb electromagnetic wave in the frequency range of 8–18 GHz and the maximum reflection loss -10 dB is larger than 8 GHz. The concrete is prepare by function aggregate show higher compressive strength 28 MPa (Figure 2.63). The concrete can use for structural material in the buildings.
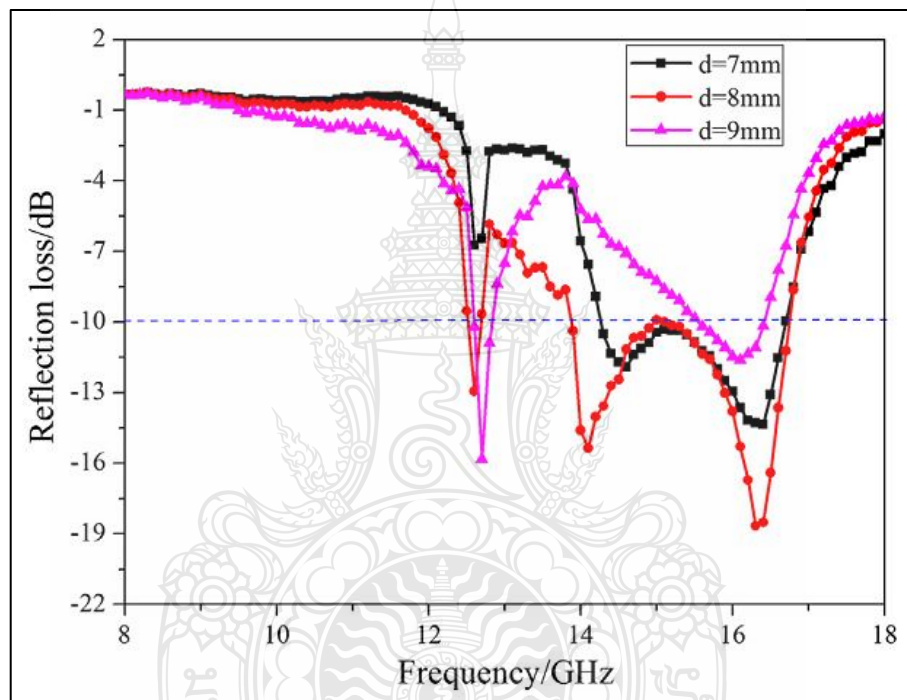
Figure 2.63 The electromagnetic wave absorbing application in concrete of TiO_2 [94].

Pawar, SP. et al. [95] study of polymeric nanocomposites for high frequency wave absorbers. This paper reviews the designing polymer nanocomposites with high electrical conductivity and for attenuation microwave absorption properties. This review article summarize the high frequency wave absorbing properties of polymer nanocomposites include from various nanoparticles such as graphene nanosheets, carbon nanotubes, reduced graphene oxide, $NiCoFe_2O_4$/ graphene oxide, Fe_3O_4, Barium ferrite, γ-Fe_2O_3 (50%) and TiO_2(25%), Copper nanowire, Fe_2O_3/graphene, Fe_3O_4@ graphene, TiO_2, $MnFe_2O_3$, Graphite copper and Ag@graphene. The polymer nanocomposites include from various polymer such as poly vinyl alcohol, poly ethylene oxide, UHMWPE, nitrile butadiene rubber, polyaniline, PEDOT: PSS, polyurethane, polyimide, PVDF, polystyrene, polystyrene and poly vinyl chloride. The polymer

nanocomposites show high dielectric constant, magnetic metal, ferrite nanoparticles for absorb microwave radiation.

The conclusion of literature review for the preparation focus on nanosheets structure by hydrothermal method is shown in Table 2.3. The conclusion of literature review for Photocatalytic activity is shown in Table 2.4. The conclusion of literature review for electromagnetic wave absorption is shown in Table 2.5.

Table 2.3 The conclusion of literature review for the preparation focus on nanosheets structure by hydrothermal method.

No.	Materials	Solution	Temperature	Time	Washed by	Morphology	Ref.
1	Titanium (IV) butoxide	Ammonia aqueous	130 ℃	12 h	HCl aqueous solution, 2-propanal distilled water	Nanosheets	12
2	Titanium tetra Iso propoxide	Ammonia aqueous	200 ℃	24 h	Distilled water and ethanol	Nanosheets	13
3	Tetrabutyl titanate	Hydro-fluoric acid solution	200 ℃	24 h	Distilled water	Nanosheets	82
4	Ti(IV) ions	10 M NaOH	120 °C	20 h	HCl aqueous solution	Nanosheets	83
5	TiCl$_3$ aqueous solution	Ethylene glycol	150 °C	4 h	Distilled water	Nanosheets	84
6	Tetrabutyl titanate	Hydro-fluoric acid	200 ℃	24 h	Distilled water	Nanosheets	85

Table 2.4 The conclusion of literature review for Photocatalytic activity.

No.	Photocatalytic activity	Compare with	Performance	Ref.
1	Dye-sensitized solar cell	P-25	Nanosheet was about 7.08% with Jsc of 16.35 mA/cm^2 P-25 reached 5.82% with Jsc of 12.74 mA/cm^2	12
2	The photocatalytic activity	P-25, JRC-01, and JRC-03	The photocatalytic activity of the nanofibers calcination at 400 °C for 2 h is higher than the commercially TiO_2 nanoparticles powders.	17
3	Dye-sensitized solar cell	P-25	Solar cells efficiency of the cell using P-25 as working electrode was about 5.82% while the mesoporous anatase TiO_2 showed efficiency about 6.30%.	70
4	H_2 evolution from water splitting reaction	ST-01	The heat treated flower-like titanate at 500 °C showed high photocatalytic activity than the commercial grad TiO_2 anatase powder (ST-01) for H_2 evolution from water splitting reaction.	71
5	Reduction of decabromodiphenyl and oxidation of rhodamine B	P-25	M-TiO_2-ns in induced reduction of decabromodiphenyl and oxidation of rhodamine B higher than those of M-TiO_2 template and nonporous crystalline TiO_2 compare with commercial P25.	74
6	Photocatalytic degradation for harmful chemical, paranitrophenol and toxic	-	Fe iron dope nanoparticles TiO_2 can degradation 92% paranitrophenol in 5 h.	79

Table 2.5 The conclusion of literature review for electromagnetic wave absorption.

No.	Absorber	Wavelength	Result	Ref.
1	Fe_3O_4 , TiO_2, polyaniline	2 - 18 GHz	The maximum reflection loss is up to -41.8 dB at 14.4 GHz	80
2	Fe_3O_4 , grapheme oxide	2 - 18 GHz	The maximum reflection loss is −44.6 dB at 6.6 GHz.	81
3	Graphene foam graphene oxide film	8.2 - 59.6 GHz	The maximum reflection loss is –26.3 dB at 51 GHz.	87
4	Graphene/Fe_3O_4	2–20 GHz	The maximum reflection loss is –11 dB at 17.4 GHz.	88
5	Titanium carbide nanowires	8.2–12.4 GHz	The maximum reflection loss is –51.0 dB at 11.8 GHz.	89
6	Multiwall carbon nanotubes	8 -12 GHZ	The shielding effectiveness is 56.72 dB at thickness about 2 mm at the frequency of 8 -12 GHZ.	90
7	Fe_3O_4 @ SnO_2/ reduced graphene oxide	2 – 18 GHz	The maximum reflection loss is –45.5 dB at 6.4 GHz.	91
8	TiO_2/Al_2O_3	8.2 -18 GHz	The maximum reflection loss is –29 dB at 10.6 GHz.	92
9	TiO_2 /polyaniline /graphene oxide	7.97 -11.88 GHz	The maximum reflection loss is –51.74 dB at 9.67 GHz.	93
10	TiO_2	8–18 GHz	The maximum reflection loss is –10 dB at >8 GHz.	94
11	Graphene, carbon nanotubes, $NiCoFe_2O_4$/, Fe_3O_4, barium ferrite, TiO_2 copper nanowire, TiO_2, $MnFe_2O_3$, graphite copper and Ag@graphene	1-20 GHz X-band and Ku-band	The maximum reflection loss is –57 dB .	95

CHAPTER 3

EXPERIMENTS

Hydrothermal synthesis, characterizations and applications of nanosheets from Thai natural magnetic leucoxene mineral

3.1 Experimental Procedure
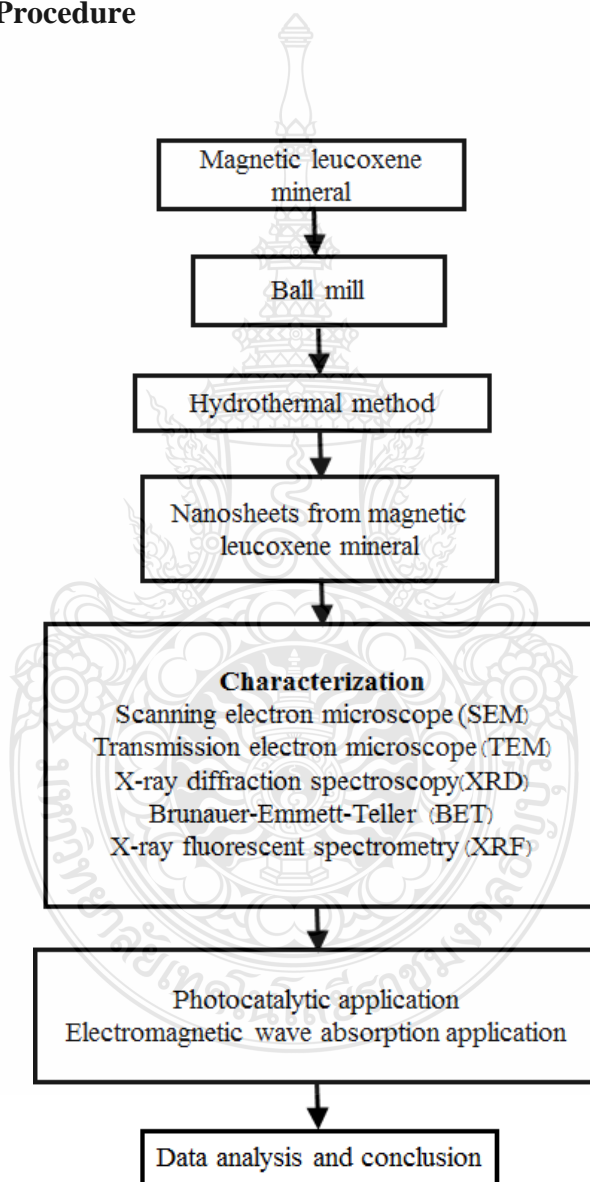
Figure 3.1 Experimental procedure of hydrothermal synthesis, characterizations and applications of nanosheets from Thai natural magnetic leucoxene mineral.

3.2 Equipments and Materials

3.2.1 Equipments

1) Hot plate stirrer

2) Digital weighting apparatus

3) Vacuum dryer

4) Thai made teflon-lined stainless steel autoclave and control unit

5) Hot air oven

Figure 3.2 Hot plate stirrer.

Figure 3.3 Digital weighting apparatus.

Figure 3.4 Vacuum filler.

Figure 3.5 Thai made teflon-lined stainless steel autoclave and control unit.

Figure 3.6 Hot air oven.

3.2.2 Materials for nanosheets synthesis

1) Magnetic leucoxene mineral have TiO_2 ~70 - 80 % in main component.
2) Sodium hydroxide (NaOH) is solution in hydrothermal method.
3) Hydrochloric acid (HCl) is washing solution distillated water is solution in hydrothermal method and washing solution.
4) Distillated water is solution in hydrothermal method and washing solution.

Figure 3.7 Magnetic leucoxene mineral.

Figure 3.8 Sodium hydroxide.
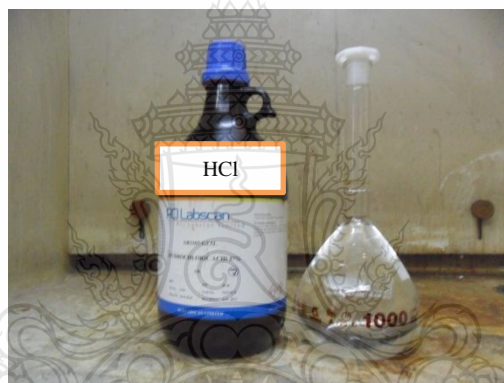
Figure 3.9 Hydrochloric acid.

Figure 3.10 Distillated water.

3.3 Experimental

3.3.1 Synthesis of TiO$_2$ nanosheets (Figure 3.11)

In this research, the nanosheets were hydrothermally synthesized using the naturally-mineral magnetic leucoxene (Sakorn Minerals, Thailand) as the starting material. In the synthesis process, 16g of the ball-milled (650 rpm for 15 minute) magnetic leucoxene mineral was deposited in a Teflon-lined stainless steel autoclave (Figure 1) and then filled with 2000 mL of 5 M NaOH (aq.) prior to heating at 105ºC for 24h under continuous stirring. The autoclave was then allowed to cool to room temperature, and the synthesized product was washed multiple times with a 0.1 M HCl (aq.) solution and subsequently with distilled water until the pH value was approximately 7.0. The product was then dried with hot air at 100ºC for 12h. Finally, calcination was performed at the temperature   range   of   100–1,100 ºC for 2h and cool to room temperature.

.
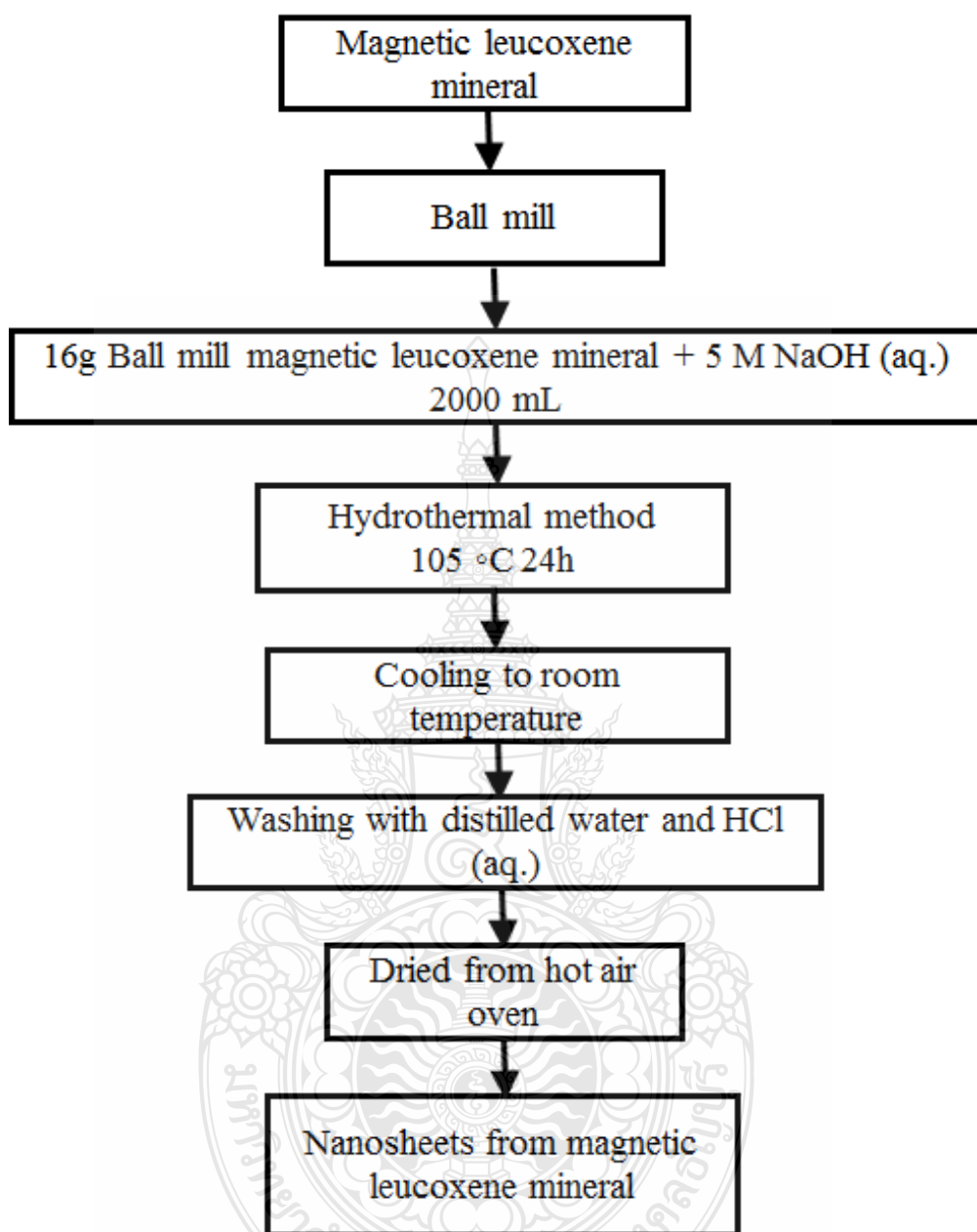
Figure 3.11 Experimental procedure synthesis of TiO_2 nanosheets.

3.4 Characterization

In this research, the characterization of the synthesized nanosheets (i.e. the as-synthesized sample) was carried out: the crystalline structure, chemical composition, shape, size and specific surface area. The crystalline structure and the chemical composition were respectively analyzed by the X-ray diffraction (XRD, PANalytical X'Pert PRO MRD) and X-ray fluorescence (XRF, Oxford, ED-2000) techniques. The shape and size of the as-synthesized sample were determined using a scanning electron microscope (SEM, JEM-6510, JEOL) with acceleration voltages of 5-20kV and a transmission electron microscope (TEM, JEOL JEM-2010 Electron Microscope). The Brunauer-Emmett-Teller technique (BET, Rubotherm, BELSORP-Mini) was used to determine the specific surface area.

3.4.1 Scanning electron microscope

Study the shapes and sizes with scanning electron microscope, SEM. (JEOL ,JEM-6510).

Figure 3.12 Scanning electron microscope.

3.4.2 X-ray diffraction spectroscopy

Study the phase and crystallinity crystal structure with X- ray Diffraction, XRD, (PANalytical, X'Pert PRO)
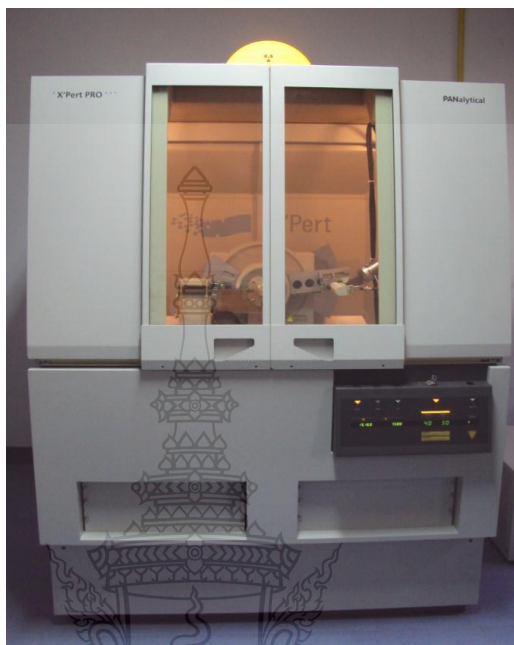
Figure 3.13 X-ray diffraction spectrometer.

3.4.3 Transmission electron microscope

Study the shapes and sizes with a transmission electron microscope, TEM (JEM-2010 JEOL).
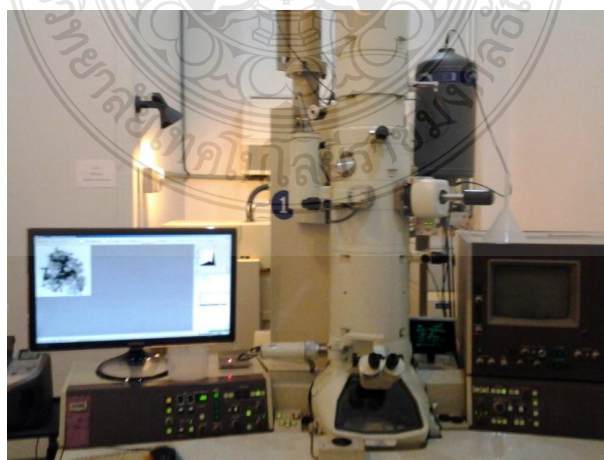
Figure 3.14 Transmission electron microscope.

3.4.4 X-ray fluorescent spectrometry

Study the chemical properties of nanosheets by X- ray fluorescence, XRF (PW-2404, Philips, 4 kW)

Figure 3.15 X-ray fluorescent spectrometer.

3.4.5 Ultraviolet–visible spectroscopy

Study the photocatalytic activity with UV-Vis spectroscopy

Figure 3.16 UV-Vis spectrometer.

3.4.6 Brunauer-Emmett-Teller analysis

Study the specific surface area by Brunauer-Emmett-Teller (BET, Rubotherm, BELSORP - Mini).

Figure 3.17 Brunauer-Emmett-Teller (BET).

3.4.7 Photocatalytic activity determination

The photocatalytic activity was determined using the I_3^- concentration from the photo oxidation reaction of I, which transformed into I_2 in excess of I [5, 27], as per Eqs. (1) and (2).

$$2\ I^- \longrightarrow I_2 + 2e^- \qquad (1)$$

$$I_2 + I^- \longrightarrow I_3^- \qquad (2)$$
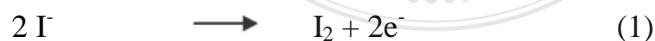
In the photocatalytic activity analysis, 50mg of the sample and 0.2M potassium iodide solution were filled into a cylindrical vessel. The Photocatalytic activity investigate in equilibrium reaction system after mixing the solution in dark for about 30 min. The vessel was then illuminated with a 15W UV and visible light under

constant stirring at room temperature for 1h. The solution was then separated by the centrifuge method and diluted 10 times prior to the measurement of ion by light absorption at 288nm using a UV–vis spectrometer. In this research, the intensity coefficient was 4.0×10^4 cm mol/l. [96]

3.4.8 Electromagnetic wave absorption measurement

Electromagnetic wave absorption measurements used Americium-241 for gamma ray (γ- ray) and primary X-ray sources. The distance between the gamma ray (γ-ray) and primary X-ray sources and sample, detector were 5, 60 cm respectively.

Figure 3.18 Electromagnetic wave absorption measurements.

CHAPTER 4

RESULTS AND DISCUSSION

4.1 Characterization Results

4.1.1 The physical property and morphology of magnetic leucoxene mineral

The as-sysnthesized sample is brown, where as the starting magnetic leucoxene mineral is black . This result indicates that a large portion of Fe impurities are remove by NaOH (aq.) hydrotermal treatment and the neutralization/washing process [31].

Figure 4.1(a) A SEM image of the starting magnetic leucoxene mineral is show in Fig. 4.1(a), this illustrates the granular structure of the material, with grain size of 150-300 µm while Figure 4.1(b) show the ball-mille magnetic leucoxene with the reduce grain size of about 0.5-10µm.
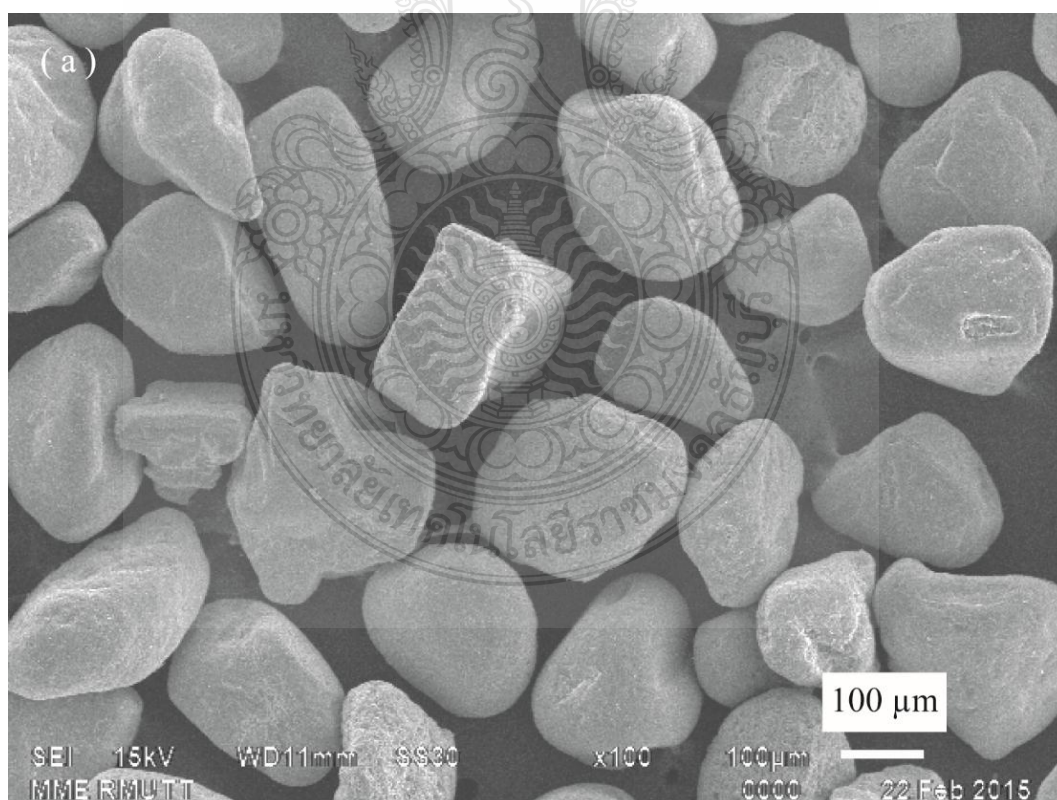
Figure 4.1 The SEM images of: (a) the magnetic leucoxene mineral (b) the ball-mille magnetic leucoxene.
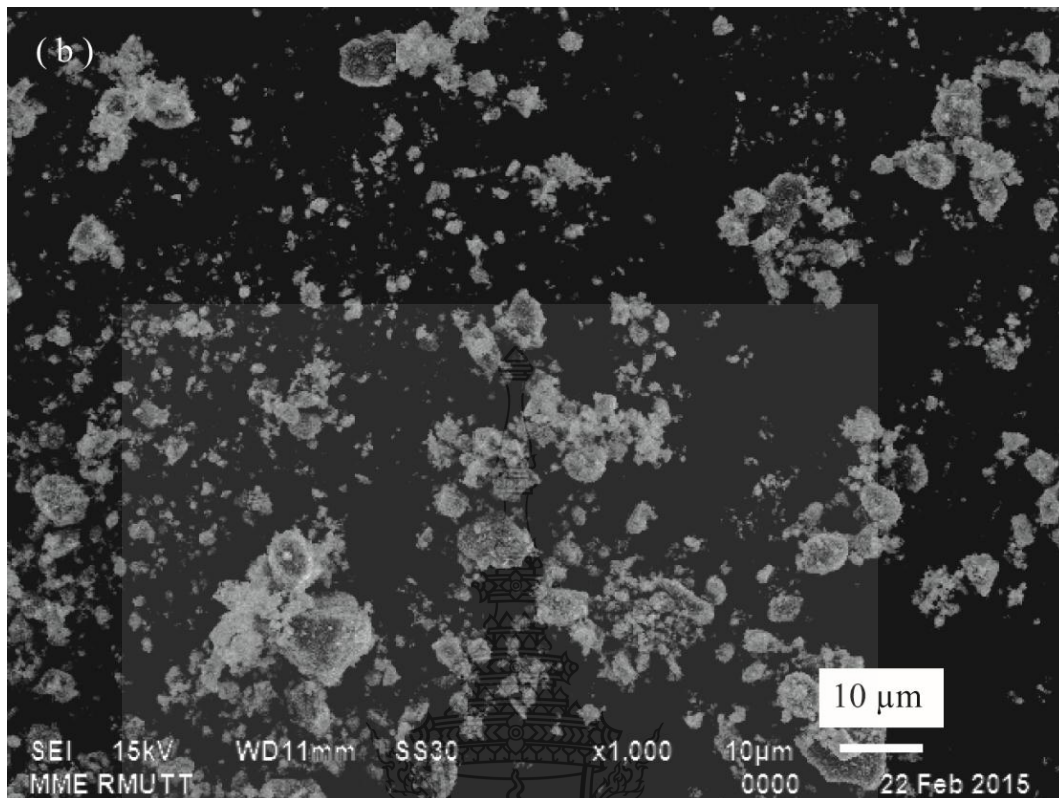
Figure 4.1 (cont.) The SEM images of: (a) the magnetic leucoxene mineral (b) the ball-mille magnetic leucoxene.

4.1.2 The XRD patterns of the starting magnetic leucoxene and the synthesized nanosheets

The XRD patterns of the starting magnetic leucoxene mineral and the synthesized sample are show in Fig. 4.2. The crystalline structure of the starting magnetic leucoxene mineral show the rutile phase, while the crystalline structure of the synthesized nanosheets show a layer hydrogen titanate $H_2Ti_xO_{2x+1}$ structure, most likely trititanate ($H_2Ti_3O_7$), indicating the existence of hydrogen in the as-synthesized nanosheets [28,31–32,99-102].
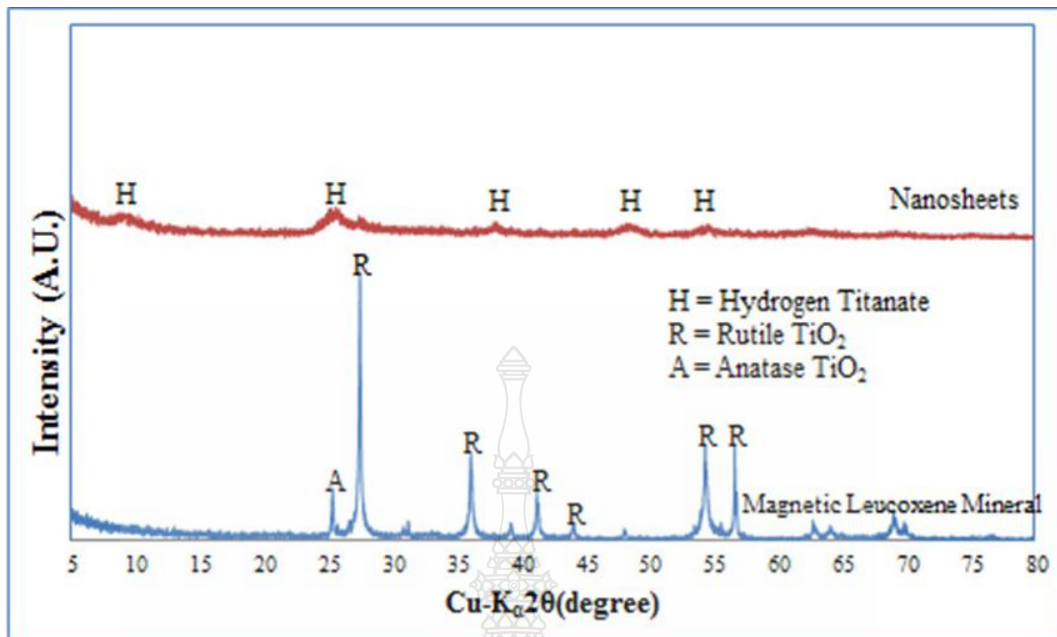
Figure 4.2 The XRD patterns of: (a) the magnetic leucoxene mineral, (b) the as-synthesized sample

4.1.4 The chemical composition of the starting magnetic leucoxene and the as-synthesized sample.

The chemical composition during the hydrothermal process , the quantities of impurities, such as Fe_2O_3, Al_2O_3, CaO, SiO_2, MnO, Nb_2O_5 and MgO decrease while the TiO_2 content increase from 79.8 to 83.2 wt%. This may be due to higher solubility of the impurities in the NaOH and HCl aqueous solutions during the preparation process shown in Table 4.1. [103-104].

Table 4.1 Chemical composition of the natural magnetic leucoxene mineral and the as-synthesized nanosheets

Composition	Magnetic leucoxene mineral	As-synthesized nanosheets
TiO_2	79.8%	83.2%
Fe_2O_3	9.59%	7.73%
CaO	0.981%	0.775%
ZrO_2	0.838%	0.685%
Nb_2O_5	0.467%	0.399%
SiO_2	1.95%	0.389%
MgO	0.319%	0.246%
SO_3	0.213%	0.187%
MnO	0.207%	0.185%
K_2O	0.179%	0.135%
Cr_2O_3	1730 PPM	929 PPM
Cl	972 PPM	750 PPM
Al_2O_3	1.95%	0.043%
Ta_2O_5	495 PPM	429 PPM
PbO	517 PPM	380 PPM
ThO_2	491 PPM	352 PPM
Sc_2O_3	240 PPM	180 PPM
Y_2O_3	213 PPM	121 PPM
SrO	44 PPM	39.7 PPM
Na_2O	0%	1.29%

4.1.4 The physical property and morphology of as-synthesized nanosheets from magnetic leucoxene mineral

Figures 4.3(a)-(c) respectively show the SEM images of the as-synthesized sample at 10,000x, 15,000x, and 50,000x magnification for the group of flower-like morphology. The flower-like structure have a diameter about 2 μm to 5 μm. the flower-like morphology compose of nanosheets. To confirm the formation of nanosheets are use TEM analysis, and a representative image show in Figures 4.4 (a)-(d). From the TEM images, it can be observed that the as-synthesize sample showed sheets –like stucture. The nanosheets structure is slightly curve and approximately 100 nm to 2 μm in width and several nanometers in thickness. The sheets radiated in all directions to form flower-like morphology, mainly as a result of the hydrothermally synthetic treatment [105].
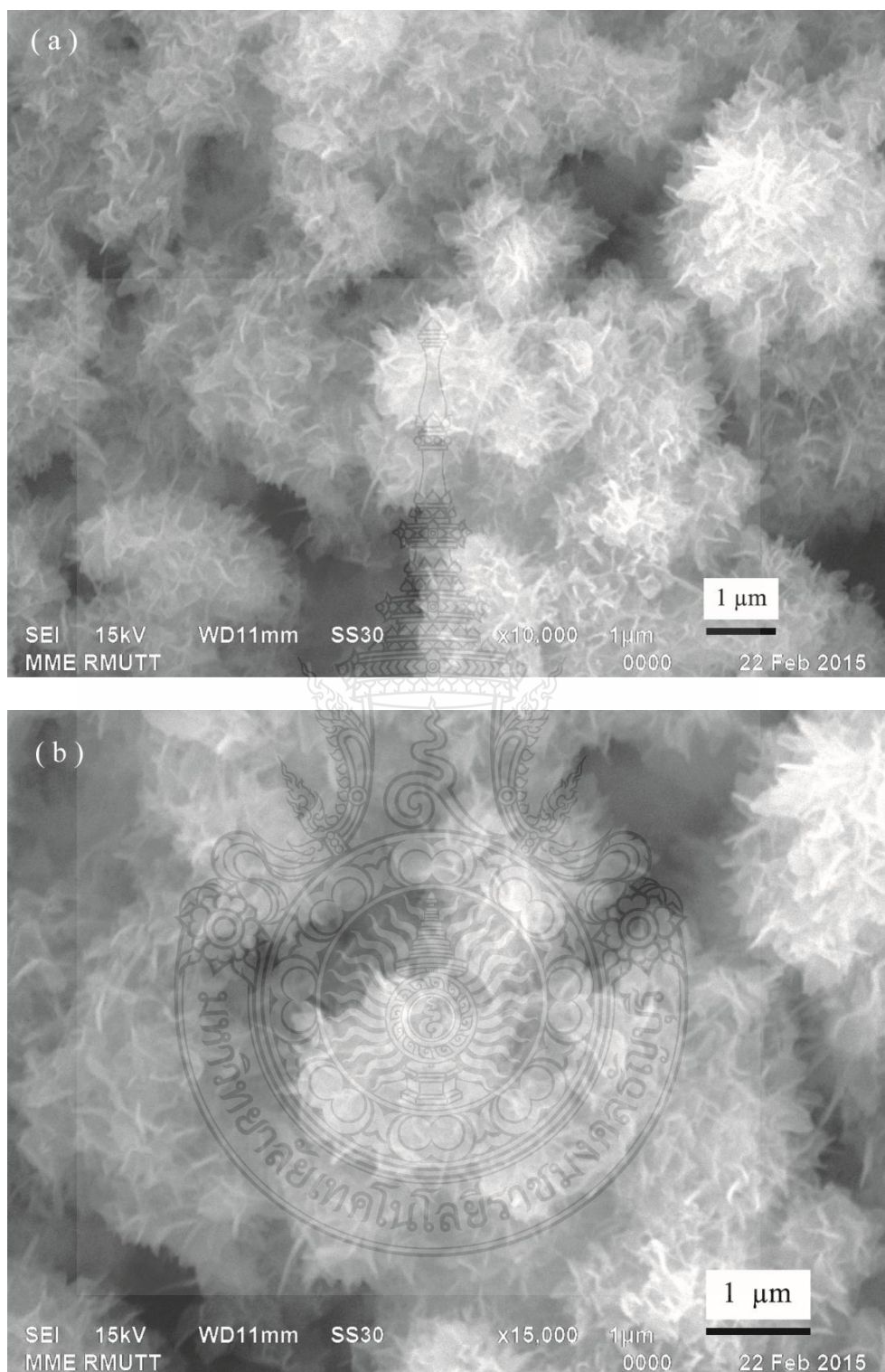
Figure 4.3 SEM images of the synthesized nanosheets: (a) 10,000x, (b) 15,000x, magnifications (c) 50,000x magnifications.
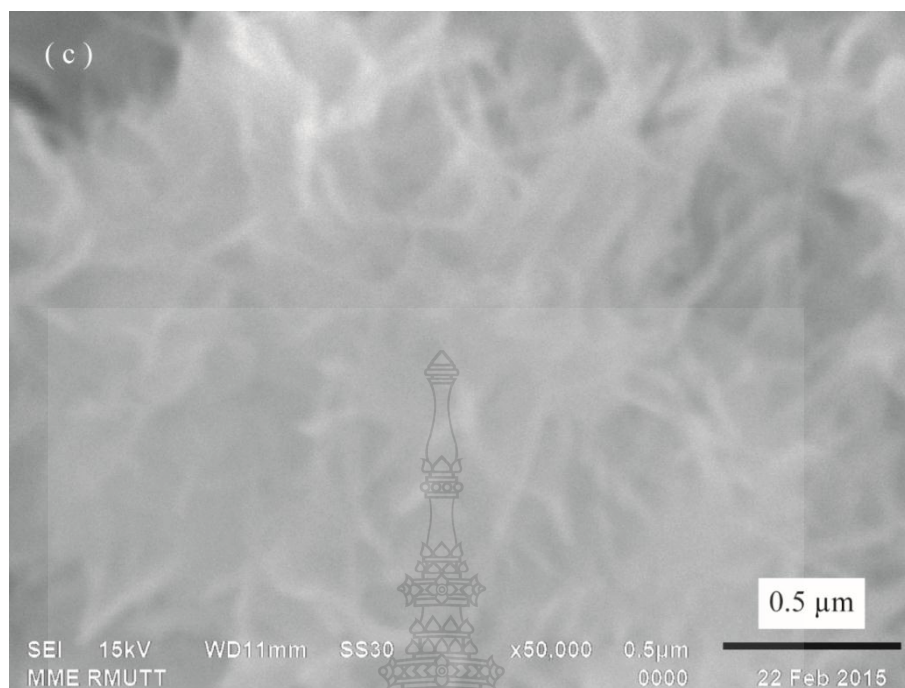
Figure 4.3 (cont.) SEM images of the synthesized nanosheets: (a) 10,000x, (b) 15,000x, magnifications (c) 50,000x magnifications.
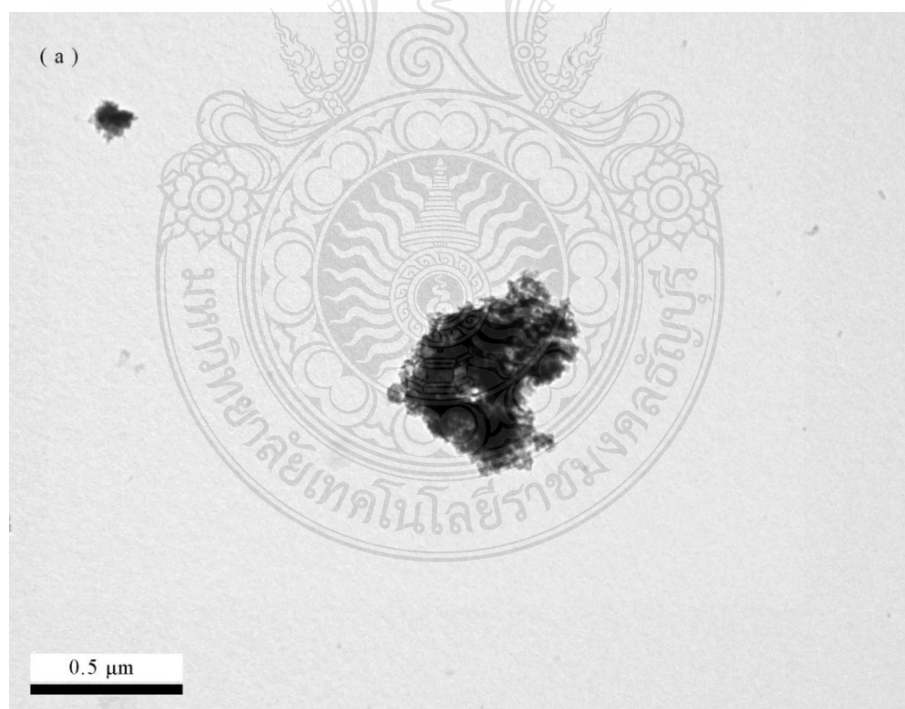
Figure 4.4 TEM images of the synthesized nanosheets: (a) 23,000x (b) 135,000x (c) 360,000x and (d) 500,000x magnifications.

(b)

50 nm

(c)

20 nm
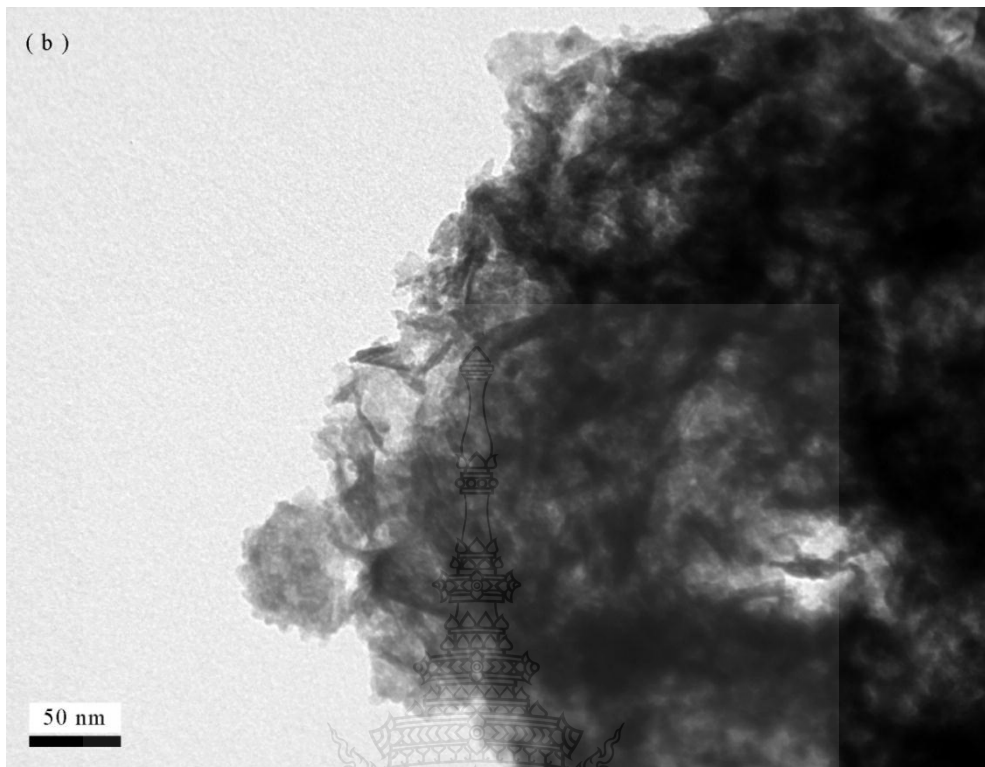
Figure 4.4 (cont.) TEM images of the synthesized nanosheets: (a) 23,000x (b) 135,000x (c) 360,000x and (d) 500,000x magnifications.
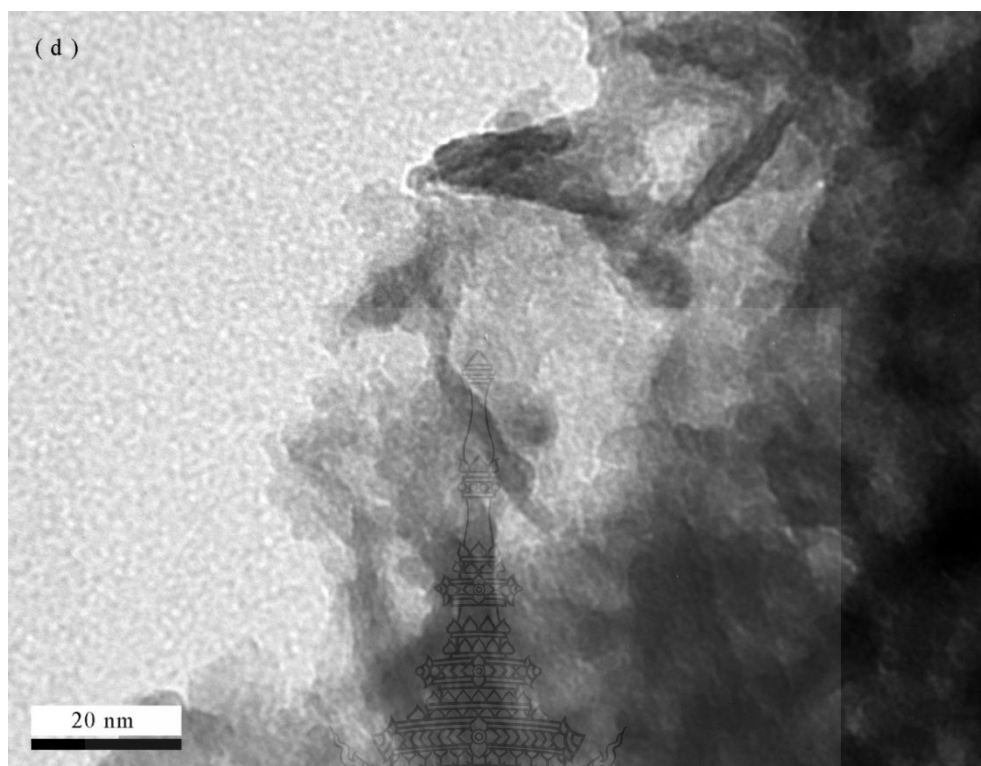
Figure 4.4 (cont.) TEM images of the synthesized nanosheets: (a) 23,000x (b) 135,000x (c) 360,000x and (d) 500,000x magnifications.

4.1.5 The mechanism transition of as-synthesized nanosheets from magnetic leucoxene mineral

Figures 4.5 illustrates the mechanism transition of as-synthesized nanosheets structures during the hydrothermal process. The hydrothermal reaction progresses, the ball-mille magnetic leucoxene have energy by heat and pressure, and then lamellar nanosheets are exfoliate from the particles of starting materials. Next, the lamellar nanosheets have energy by heat and pressure, and then then lamellar nanosheets are transformation to flower-like structure for more thermal stability [12, 26, 106-107].

Figure 4.5 Scheme of the transition process of the as-synthesized nanosheets structures
during the hydrothermal process.

4.1.5 The nitrogen adsorption isotherm of the as-synthesized nanosheets

Figure 4.6 depicts the nitrogen adsorption isotherm of the as-synthesized nanosheets which is of a typical IUPAC type IV pattern, with the sharp inflection of nitrogen adsorption volume at P/P0 of 0.40 (H2 type hysteresis loop), indicating the existence of mesoporous materials [4-5, 7, 103-104] with the pore size distribution of 3–35nm (the inset). The BET specific surface area and the pore volume of the as-synthesize nanosheets are 279.8 m^2/g and 0.513 cm^3/g, respectively. As a comparison, Figure 4.7 illustrates the nitrogen adsorption isotherm of the commercial TiO_2 nanoparticles (P-25). The isotherm is of an IUPAC type II with a H3 type hysteresis loop typical of macroporous materials [105], similar to that of TiO_2, and the pore size distribution (the inset) is about 3–65nm. The BET surface area and the pore volume of the P-25 specimen are 46.92 m^2/g and 0.306 cm^3/g, respectively.
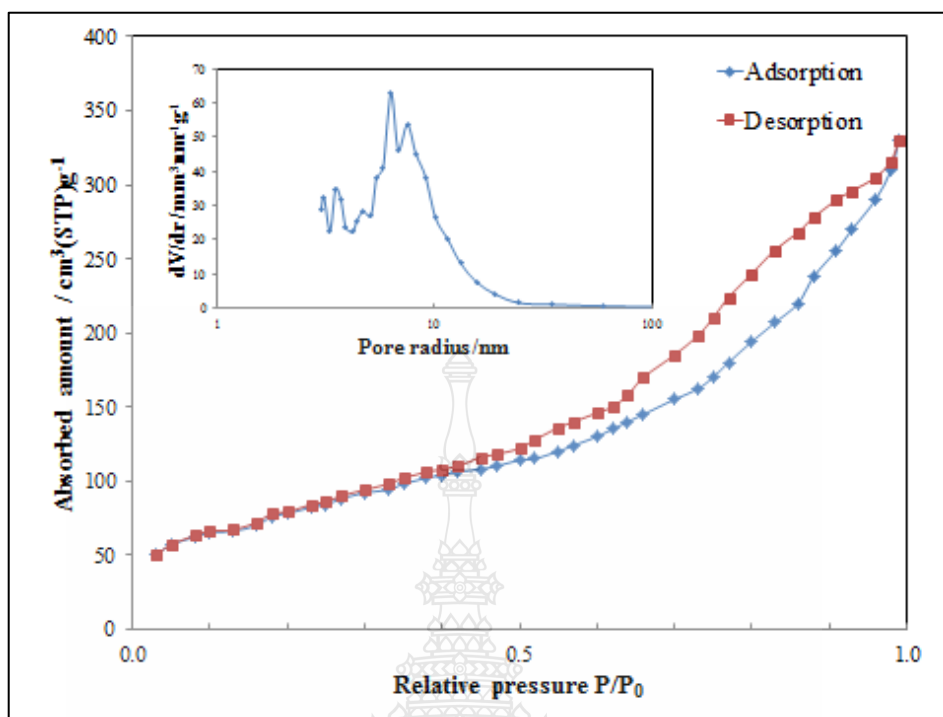
Figure 4.6 The nitrogen adsorption isotherm pattern of the as-synthesized nanosheets and the pore size distribution with the pore diameters of 3–35nm (inset)
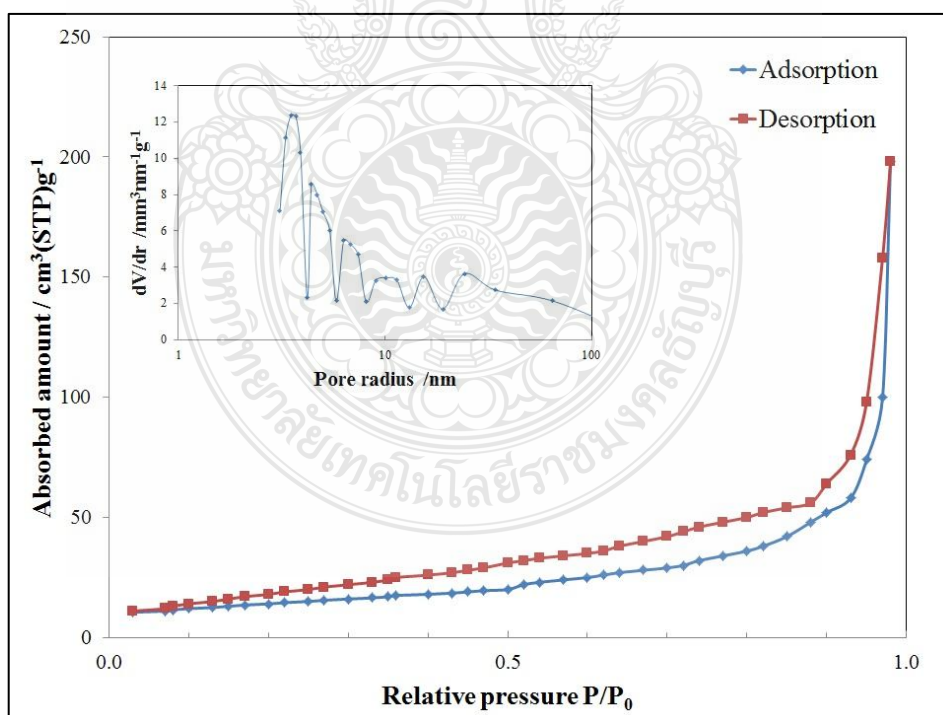
Figure 4.7 The nitrogen adsorption isotherm pattern of the commercial TiO_2 nanoparticles (P-25) and the pore size distribution with the pore diameters of 3–65nm (inset).

4.1.5 The BET specific surface areas of the starting material and the as-synthesized sample

Determination of the specific surface area of the starting materials and the as-synthesized sample that measure by the BET (Brunauer-Emmett-Teller) using adsorption of nitrogen. The starting materials are the specific surface area of around 0 m² / g. When the as-synthesized sample by hydrothermal process at temperature of 105 ℃ over a period of 24 h, the specimens are prepare with specific surface area and pore volume around. 279.8 m² / g and 0.513 cm^3 / g respectively, the as-synthesized nanofibers from previous works about 49 m² / g and 0.159 cm^3 / g respectively, commercial TiO$_2$ nanoparticles(P-25) about 46.97 m² / g and 0.306 cm^3 / g respectively. The specific surface area of the as-synthesized nanosheets samples are 270-280 times greater than the starting material and compare with commercial TiO$_2$ nanoparticles (P-25) were the specific surface area and pore volume are more than the as-synthesized nanofiber from previous works and the commercial TiO$_2$ nanoparticles(P-25) shown in Table 4.2.

Table 4.2 The BET specific surface areas and pore volumes

Samples	BET specific surface area (m^2/g.)	pore volume (cm^3/g.)
Magnetic leucoxene (starting material)	~ 0	-
Nanofibers (previous work)	49	0.159
Nanosheets (this study)	279.70	0.513
Commercial TiO$_2$ nanoparticles (P-25)	46.97	0.306

4.1.6 Photocatalytic activity

The Photocatalytic activity was investigate in equilibrium reaction system after mixing the solution in dark for about 30 min [96]. The I$_3^-$ concentration at 60 min of the irradiation period of the as-synthesized nanosheets is about 7.71×10^{-4} M. (Fig. 4.8) which is higher than that of the other synthesized (i.e., the white pigment TiO$_2$ and the commercial grade TiO$_2$ nanoparticles (P-25)) which exhibit I$_3^-$ concentration about $0.0.73 \times 10^{-4}$, and 3.29×10^{-4} M, respectively. The introduction of mesopore into titania photocatalyst substantially improve the photocatalytic performance [6]. The flower-like

titanate superstructure show high photocatalytic activity due to their unique structure [8]. The nanosheets have good crystallinity and well-defined chemical composition and exhibit distinctive physicochemical properties. Therefore, these nanosheets become a potential building block for the construction of nano materials in the fields of photocatalysis, photoluminescence, and photo electrochemistry. The integration of noble metal nanosheets at the surface of TiO_2 has been a widely successful strategy and recognize for improving the photocatalytic activity of TiO_2. The nanosheets of TiO_2, TiO_2/Fe_3O_4 in the composition has been promoting faster interfacial electron transfer cause of improve photocatalytic activity [97,108-110].
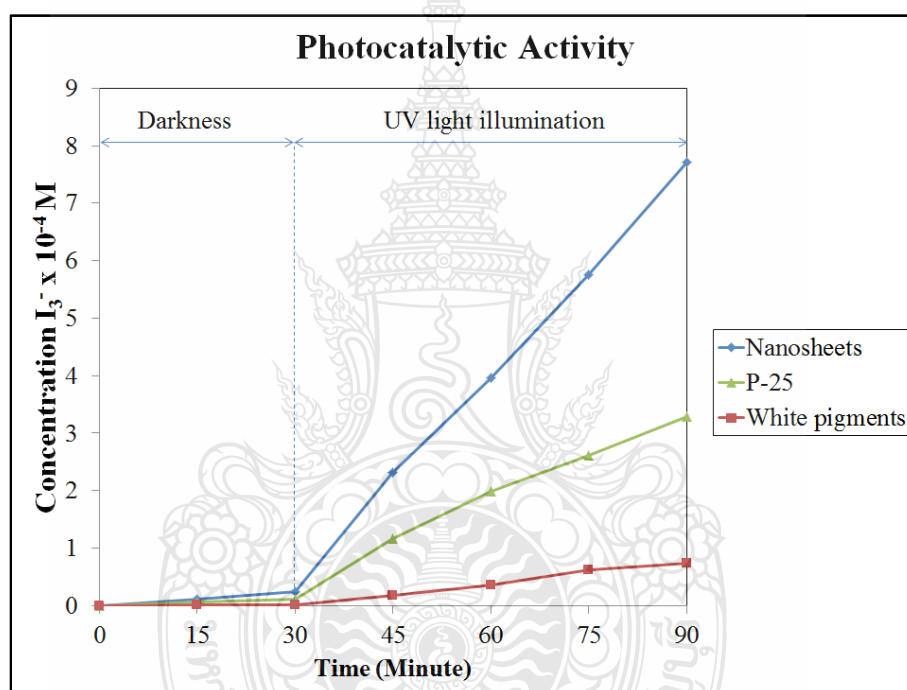
Figure 4.8 The photocatalytic activity (I_3^- concentration) of the nanosheets TiO_2, white pigment TiO_2, commercial TiO_2 nanoparticles (P-25).

4.2 Effect of Calcination Temperature on Structure and Photocatalytic Activity

4.2.1 The XRD patterns of the as-sysnthesized samples and the samples calcination for 2 h at 100 – 1,100 ºC.

The XRD patterns of the as-sysnthesized samples and the samples calcination for 2 h at 100 - 400 ºC is show in figure 4.9 (a). At 100 and 200 ºC, the crystalline structure of the as-sysnthesized nanosheets show a layer of hydrogen titanate $H_2Ti_xO_{2x+1}$ structure, most likely trititanate ($H_2Ti_3O_7$). At 300 and 400 ºC, the calcined samples

87

show TiO_2 (B). The nanosheets are dehydrate and recrystallize into the phase of TiO_2 (B). Moreover, the intensity peaks show the TiO_2 (B) decrease while the calcination temperatures increase. [28, 31–32, 99-102]

The XRD patterns of the as-sysnthesized samples calcination at 500–1100 ℃ for 2 h are show in Figure 4.9 (b). At 500 and 600 ℃, the calcination nanosheets show a bi-crystalline mixture consisting of anatase TiO_2 and TiO_2 (B). Recent research studies found a bi-crystalline mixture consisting of anatase TiO_2 and TiO_2 (B) nanostructure.[17] At 700–1000 ℃, the as-sysnthesized samples consist of a mixture of anatase and rutile. The phase of TiO_2 (B) disappears, and the transformation structure to anatase and rutile phaseTiO_2. In this temperature range the rutile phases TiO_2 begin demonstrate. The rutile phase is increases when the calcination temperatures increase. At 1100 ℃, The as-sysnthesized samples are consist a mixture of anatase, rutile phase of TiO_2, and Fe_2O_3 phase. [28, 31–32, 99-102]
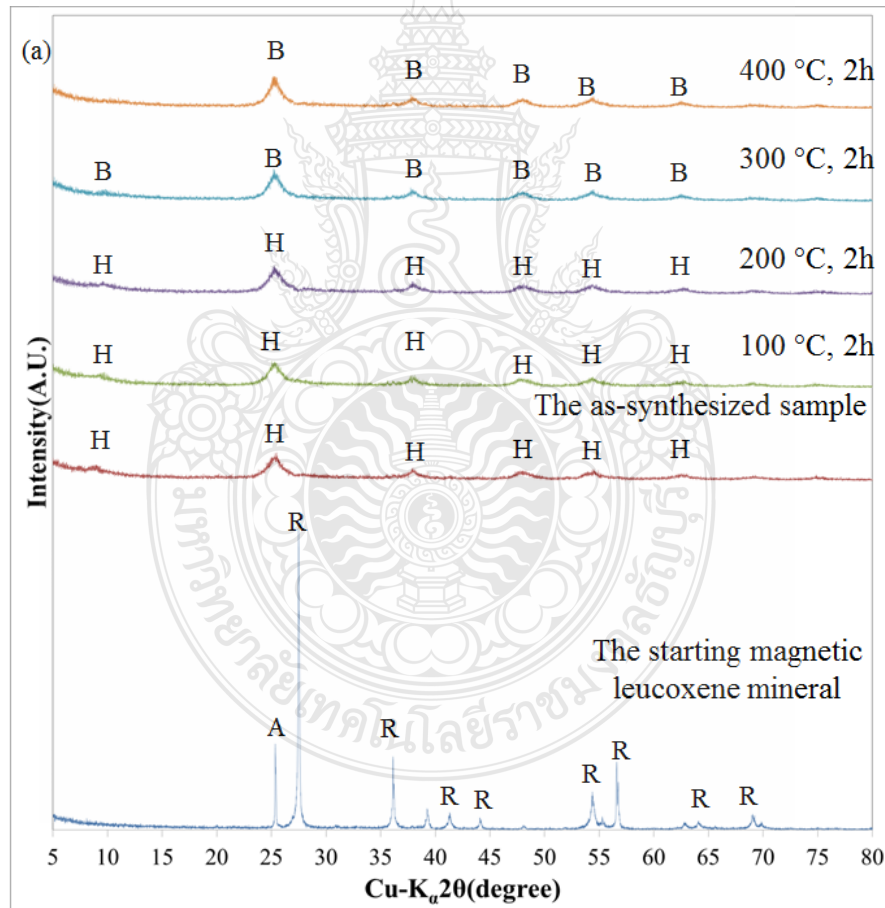
Figure 4.9 The XRD patterns of: (a) the magnetic leucoxene mineral, the calcination is perform at the temperature range of 100–400 ℃, (b) the calcination is perform at the temperature range of 500–1,100 ℃.
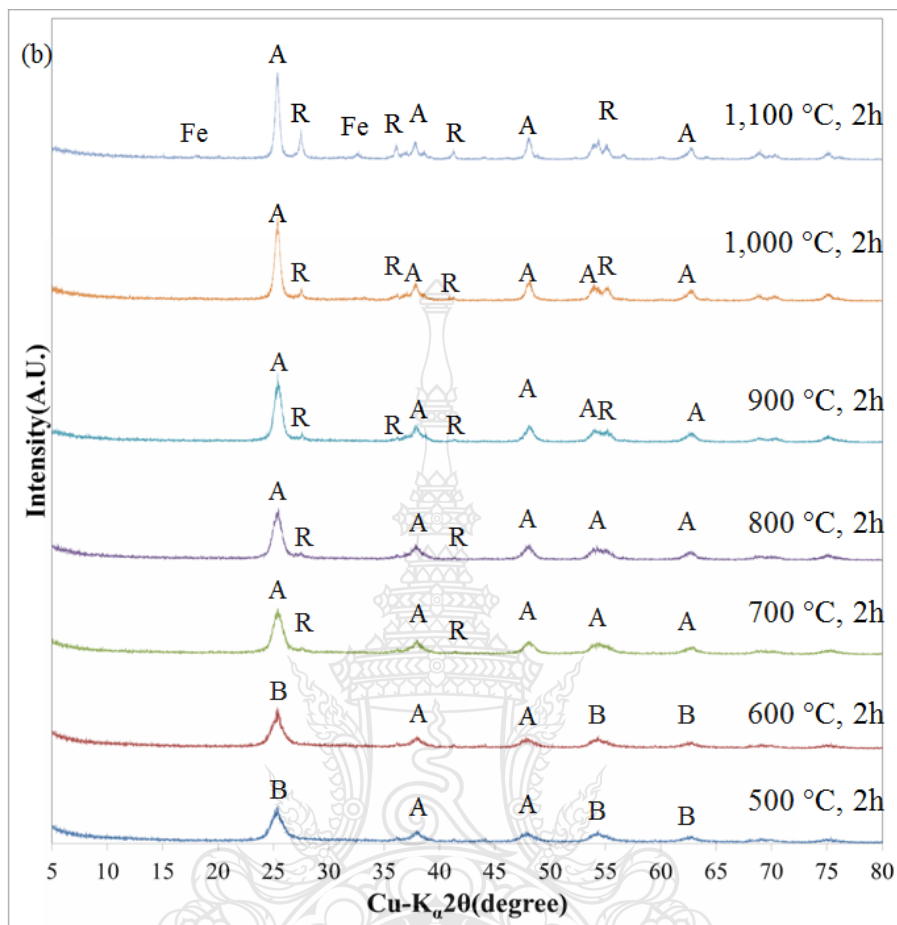
Figure 4.9 (cont.) The XRD patterns of: (a) the magnetic leucoxene mineral, the calcination is perform at the temperature range of 100–400 ℃, (b) the calcination is perform at the temperature range of 500–1,100 ℃.

    4.2.2 The physical property and Morphology of the as-sysnthesized samples and the samples calcination for 2 h at 100 – 1,100 ℃.

    To confirm the formation of nanosheets is use TEM analysis. As show in figure 4.10 (a), it can be observe that the as-sysnthesized sample show sheets–like structure. The nanosheets structure is slightly curve and approximately 100 nm to 2 μm in width and several nanometers in thickness. The sheets radiated in all directions to form flower-like morphology, accomplish mainly by hydrothermal synthesis. The structure may be the results of the orient attachment effect during crystal grow. The method control the self-assembly of nanostructures and obtain TiO_2 spheres, compose of nanosheets hierarchical structures to flower-like TiO_2 nanosheets [104].

Figure 4.10 (b–l) shows the TEM images of the as-sysnthesized samples and the samples calcination for 2 h at 100 to 1100 ºC. At 100 and 200 ºC, the morphology of sample show sheets–like structure. At 300–500 ºC, the sheets–like morphology become unstable and begin crack inside the sheets. At 600–900 ºC, the morphology of sample begins nanoparticles structure. At 1,000–1,100 ºC, the nanoparticles morphology is increasing size. At 300–1100 ºC, the calcination nanosheets become unstable and began to decompose and transform into nanoparticles and increasing size. The increasing sizes of nanoparticles decrease the specific surface area of the nanosheets cause by increasing calcination temperature. [14-15, 17]
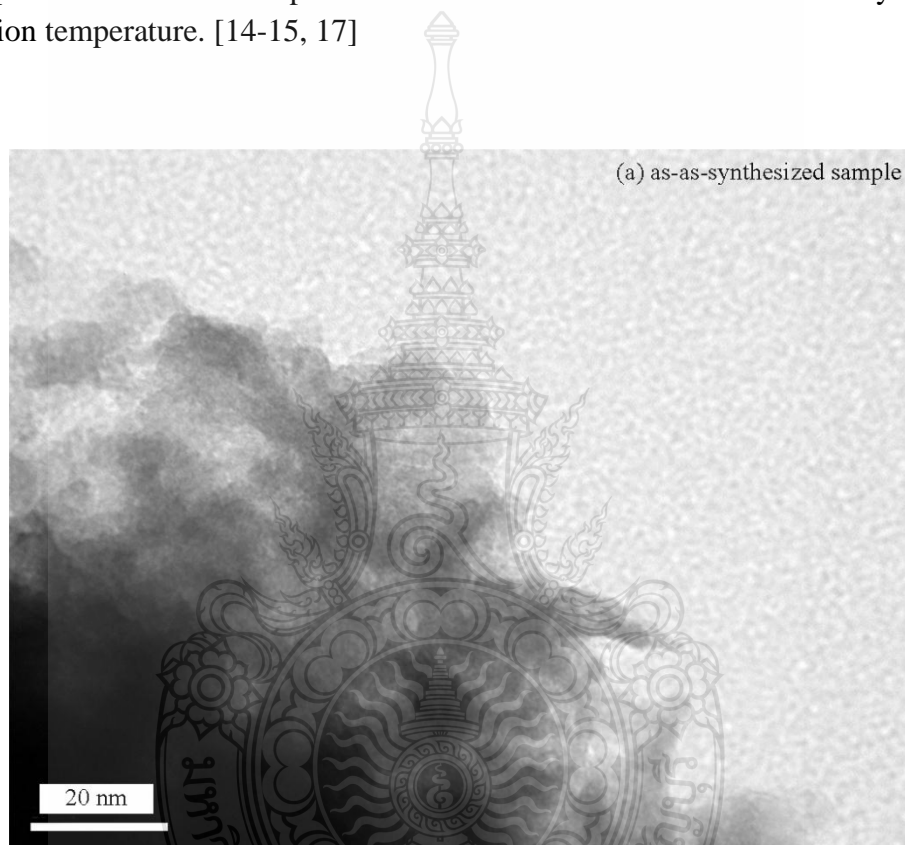
Figure 4.10 TEM images of (a) the as-synthesized nanosheets, the as-synthesized nanosheets calcination is perform at the temperature range of (b) 100 ºC, (c) 200 ºC, (d) 300 ºC, (e) 400 ºC, (f) 500 ºC, (g) 600 ºC, (h) 700 ºC, (i) 800 ºC, (j) 900 ºC, (k) 1,000 ºC, and (l) 1,100ºC.

Figure 4.10 (cont.) TEM images of (a) the as-synthesized nanosheets, the as-synthesized nanosheets calcination is perform at the temperature range of (b) 100 ℃, (c) 200 ℃, (d) 300 ℃, (e) 400 ℃, (f) 500 ℃, (g) 600 ℃, (h) 700 ℃, (i) 800 ℃, (j) 900 ℃, (k) 1,000 ℃, and (l) 1,100℃.

Figure 4.10 (cont.) TEM images of (a) the as-synthesized nanosheets, the as-synthesized nanosheets calcination is perform at the temperature range of (b) 100 ℃, (c) 200 ℃, (d) 300 ℃, (e) 400 ℃, (f) 500 ℃, (g) 600 ℃, (h) 700 ℃, (i) 800 ℃, (j) 900 ℃, (k) 1,000 ℃, and (l) 1,100℃.

(f) 500℃

20 nm

(g) 600°C

20 nm

Figure 4.10 (cont.) TEM images of (a) the as-synthesized nanosheets, the as-synthesized nanosheets calcination is perform at the temperature range of (b) 100 ℃, (c) 200 ℃, (d) 300 ℃, (e) 400 ℃, (f) 500 ℃, (g) 600 ℃, (h) 700 ℃, (i) 800 ℃, (j) 900 ℃, (k) 1,000 ℃, and (l) 1,100℃.

Figure 4.10 (cont.) TEM images of (a) the as-synthesized nanosheets, the as-synthesized nanosheets calcination is perform at the temperature range of (b) 100 ℃, (c) 200 ℃, (d) 300 ℃, (e) 400 ℃, (f) 500 ℃, (g) 600 ℃, (h) 700 ℃, (i) 800 ℃, (j) 900 ℃, (k) 1,000 ℃, and (l) 1,100℃.

Figure 4.10 (cont.) TEM images of (a) the as-synthesized nanosheets, the as-synthesized nanosheets calcination is perform at the temperature range of (b) 100 ℃, (c) 200 ℃, (d) 300 ℃, (e) 400 ℃, (f) 500 ℃, (g) 600 ℃, (h) 700 ℃, (i) 800 ℃, (j) 900 ℃, (k) 1,000 ℃, and (l) 1,100℃.

Figure 4.10 (cont.) TEM images of (a) the as-synthesized nanosheets, the as-synthesized nanosheets calcination is perform at the temperature range of (b) 100 ℃, (c) 200 ℃, (d) 300 ℃, (e) 400 ℃, (f) 500 ℃, (g) 600 ℃, (h) 700 ℃, (i) 800 ℃, (j) 900 ℃, (k) 1,000 ℃, and (l) 1,100℃.

4.2.3 The photocatalytic activity of the as-synthesized samples and the samples calcination for 2 h at $100 - 1,100$ ℃.

In this experimental research, the photocatalytic activity is determined using the I_3^- concentration. In figure 4.11, the I_3^- concentration of the as-synthesized nanosheets, give the 60-minute UV light irradiation period, is approximately 3.22×10^{-4} M, which is noticeably higher than those of the commercial micro-size TiO_2 (white pigment) and the commercial grade TiO_2 nanoparticles (JRC-01, JRC-03, ST-01 and P-25), whose I_3^- concentrations are respectively 0.43×10^{-4}, 1.08×10^{-4}, 0.66×10^{-4}, 1.30×10^{-4} and 1.80×10^{-4} M. The samples calcination for 2 h at $100 - 1,100$ ℃, I_3^- concentrations are respectively 3.18×10^{-4}, 3.13×10^{-4}, 3.06×10^{-4}, 3.03×10^{-4}, 2.75×10^{-4}, 2.73×10^{-4}, 2.67×10^{-4}, 2.68×10^{-4}, 2.72×10^{-4}, 2.81×10^{-4} and 2.87×10^{-4} M. While, The I_3^- concentration of the as-synthesized nanosheets, given the 60-minute visible light irradiation period, is approximately 2.21×10^{-4} M, which is noticeably higher than those of the commercial micro-size TiO_2 (white pigment) and the commercial grade TiO_2 nanoparticles (JRC-01, JRC-03, ST-01 and P-25), whose I_3^- concentrations are respectively 0.06×10^{-4}, 0.29×10^{-4}, 0.10×10^{-4}, 0.46×10^{-4} and 0.49×10^{-4} M. The samples calcination for 2 h at $100 - 1,100$ ℃, I_3^- concentrations are respectively 2.11×10^{-4},

$1.88{\times}10^{-4}$, 1.78×10^{-4}, $1.65{\times}10^{-4}$, $1.59{\times}10^{-4}$, 1.57×10^{-4}, $1.50{\times}10^{-4}$, $1.65{\times}10^{-4}$, 1.77×10^{-4}, $1.82{\times}10^{-4}$ and $1.85{\times}10^{-4}$M. In addition, the distinctive flower-like structure of the nanosheets contributes to the high photocatalytic activity [13]. The introduction of mesopore into the titanium-base photocatalyst substantially improved the photocatalytic performance [6]. After the samples calcination, the nanosheets structure become unstable and begin to decompose and transform into nanoparticles, that is the cause of specific surface area decrease and lower photocatalytic activity. At 900 – 1,100 °C, more anatase TiO_2 phase is high photocatalytic activity than rutile phase because the energy position of the conduction band edge of anatase is higher than that of rutile [14-15,17, 111]. Furthermore, the high proportion of Fe_2O_3 (9.59%) in the starting material (i.e. the naturally-occurring magnetic leucoxene) extends the photocatalyst's response into the visible region and at the same time improves the oxidation of several organic compounds, e.g. chloroform, toluene, benzene, alcohols and ethers, as opposed to many other starting materials that require the iron-doping [111].

The hydrothermally synthesized nanosheets afford us with the advantages of large specific surface area, confined atomic-level thickness and salient surface-chemical states, in addition to the distinct mechanical, thermal, electronic and optical properties [112]. Furthermore, the 2D nanostructured metal oxides could become a building block for the construction of nano-materials in the fields of photocatalysis [110] and photo-electrochemistry [109].
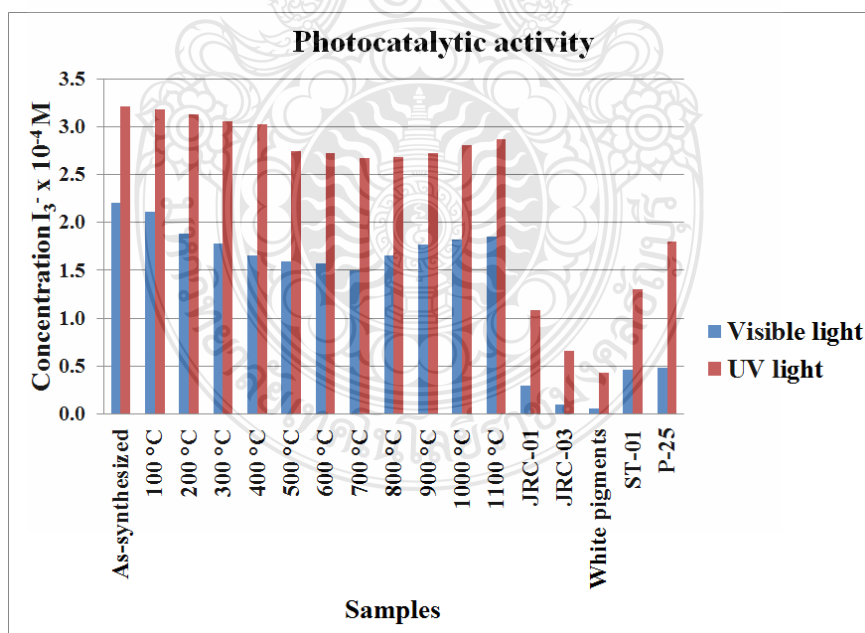
Figure 4.11 The photocatalytic activity (I_3^- concentration) of the as-synthesized nanosheets, the calcination is perform at the temperature range of 100–1,100 °C, the commercial micro-size TiO_2 (white pigment) and the commercial TiO_2 nanoparticles (JRC-01, JRC-03, ST-01 and P-25).

4.3 Electromagnetic Wave Absorption Activities

4.3.1 The XRD patterns of the electromagnetic wave absorber plates

The XRD patterns of the electromagnetic wave absorber plates are show in Figure 4.12. The crystalline structure of the electromagnetic wave absorber plates show the high crystallinity phase of polyethylene. The amount of crystalline phase of polyethylene decreases when the amount of the as-synthesized nanosheets increases. The nanosheets insert between chains of polyethylene affect to more space difficultly chains orientation cause of decrease crystallinity phase of polyethylene.
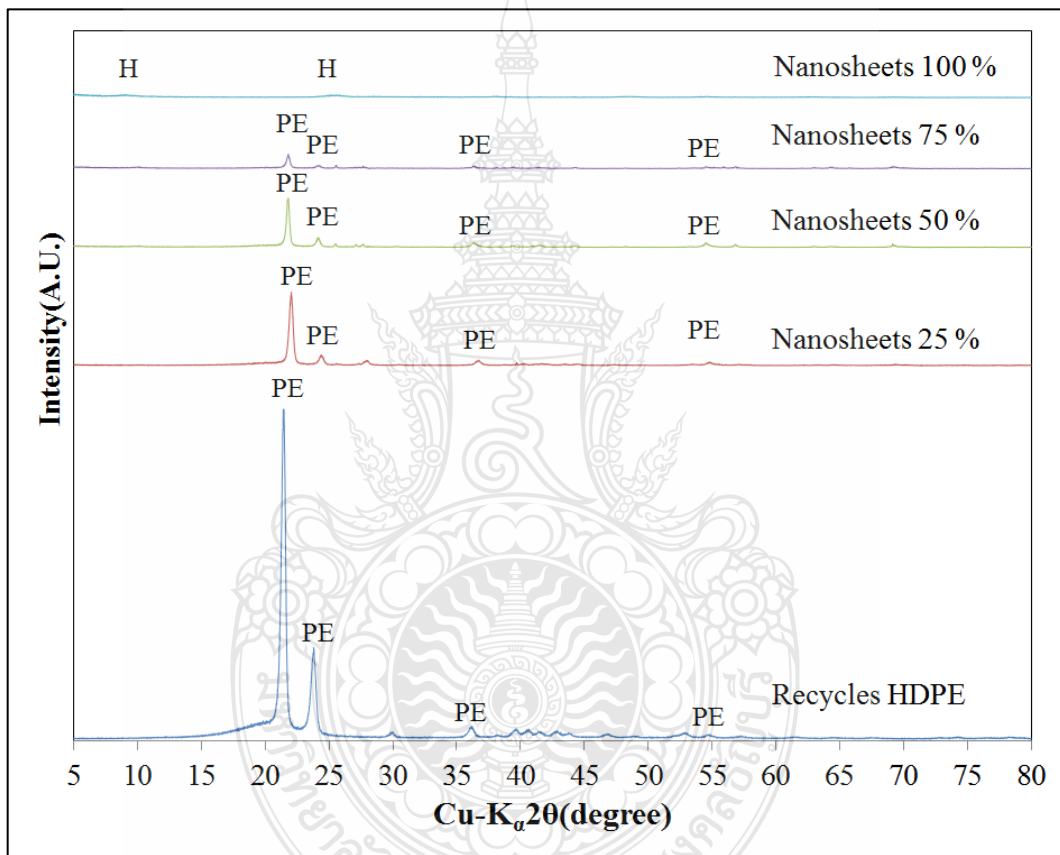
Figure 4.12 The XRD patterns of the electromagnetic wave absorber plates (a) the magnetic leucoxene mineral and the as-synthesized sample.

4.3.2 The electromagnetic wave absorption activities in gamma (γ) ray and x-ray region of electromagnetic wave absorber coin

The electromagnetic wave absorption activities in gamma (γ) ray and x-ray region of electromagnetic wave absorber coin are show in Figure 4.13. The electromagnetic wave absorber coin with nanosheets and the commercial TiO_2 nanoparticles (P-25) can absorb electromagnetic wave in gamma (γ) ray and x-ray

region from I0 18696 to 642 and 1892 counts per minute were 96.57 and 89.88% of the initial intensity, respectively. The percentage of electromagnetic wave absorption activities increase whiles the BET specific surface area increase and the electromagnetic wave absorption activities of electromagnetic wave absorber can be explained by material for electromagnetic wave absorber such as TiO_2, Fe/TiO_2 and Fe_3O_4/TiO_2 for electromagnetic waves absorber can absorb electromagnetic waves. [80-81, 87-95].
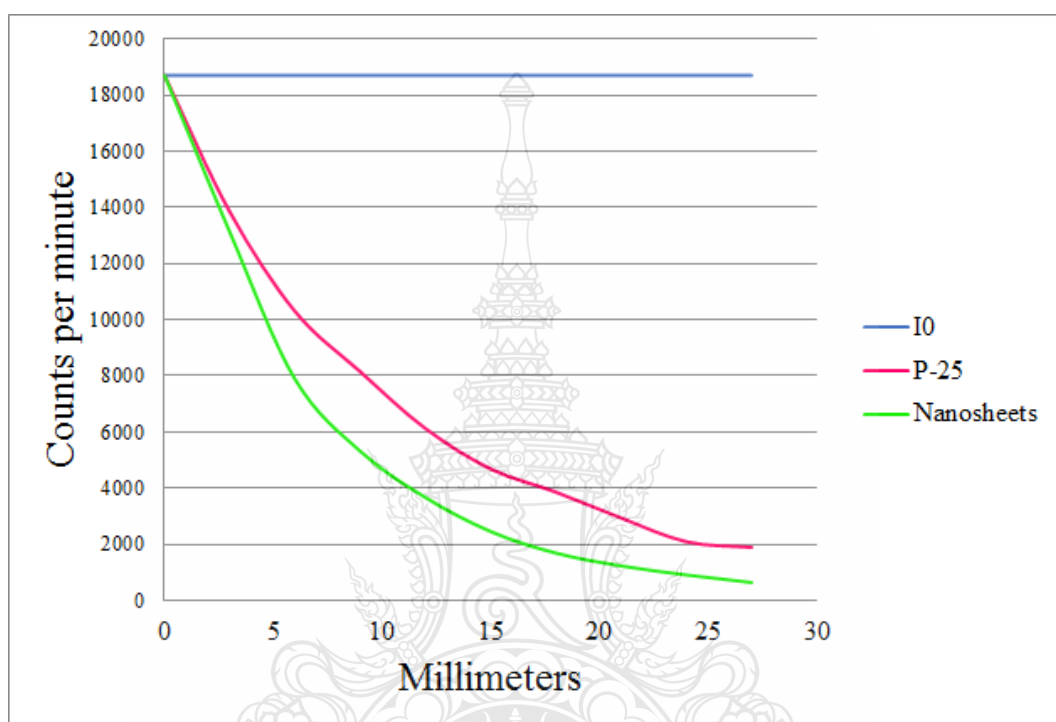
Figure 4.13 Electromagnetic wave absorption activities of electromagnetic wave absorber coin between the synthesized nanosheets and the commercial TiO_2 nanoparticles (P-25).

The electromagnetic wave absorption activities in gamma (γ) ray and x-ray region of electromagnetic wave absorber plates at the thickness 0-27 mm are shown in Figure 4.14. The electromagnetic wave absorber plates with 100 % recycled HDPE can absorb electromagnetic wave in gamma (γ) ray and x-ray region from I0 18,696 to 12,653 counts per minute was 32.32 % of the initial intensity. The electromagnetic wave absorber plates with 25, 50, 75 and 100 % nanosheets from magnetic leucoxene mineral can absorb electromagnetic wave in gamma (γ) ray and x-ray region from I0 18,696 to 7,567, 5,807, 3844 and 642 counts per minute were 59.53, 68.94, 79.44 and 96.57% of the initial intensity, respectively. The percentage of electromagnetic wave absorption activities increase while the nanosheets contain increase. The electromagnetic wave absorption activities of electromagnetic wave absorber can be explained by material for electromagnetic wave absorber such as TiO_2, Fe/TiO_2 and

Fe_3O_4/TiO_2 for electromagnetic waves absorber can absorb electromagnetic waves. [80-81, 87-95].
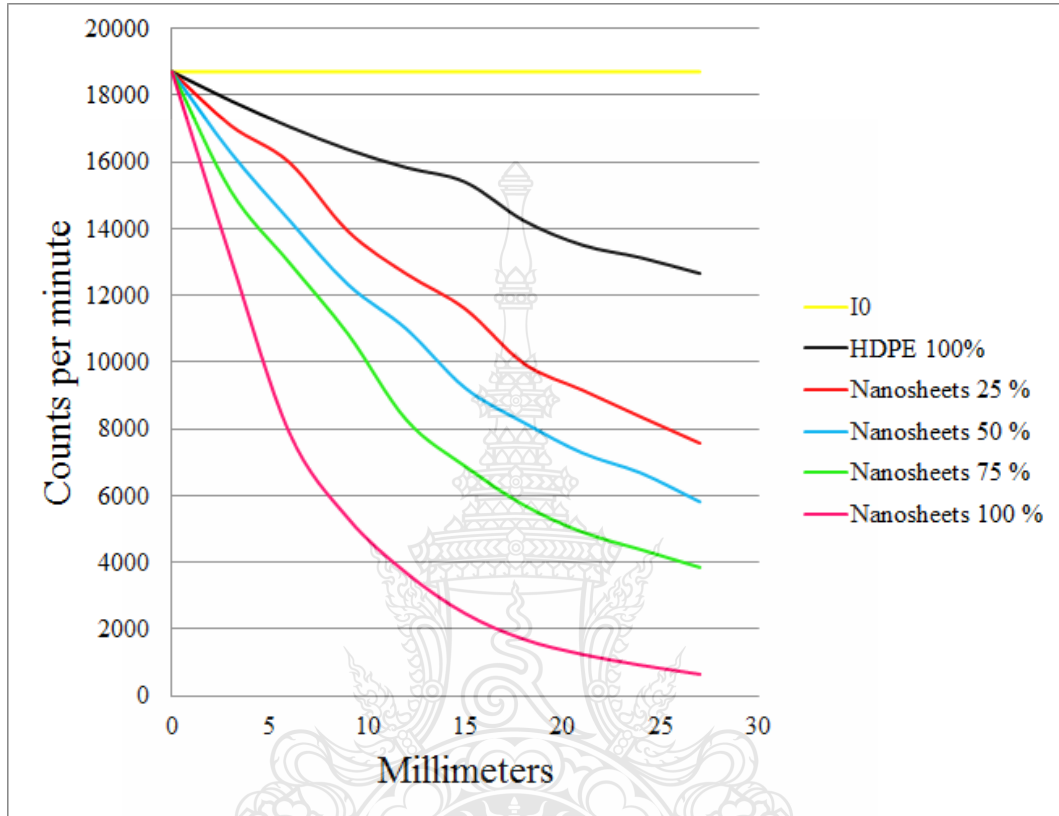
Figure 4.14 Electromagnetic wave absorption activities of electromagnetic wave absorber plates made from different ratios between the recycle HDPE and the synthesized nanosheets.

The scheme of electromagnetic wave absorption activities are shown in Figure 4.15. The initial electromagnetic wave going from Americium 241 primary source for gamma (γ)-ray and x-ray attack the electromagnetic wave absorber. Some initial electromagnetic wave had been reflection. Some initial electromagnetic wave hit particle of minerals has been reflection and multiple reflections to next minerals. Some electromagnetic wave can be absorption in electromagnetic wave absorber. Some electromagnetic wave can be transmitted. The transmission electromagnetic wave can be detected by detector.
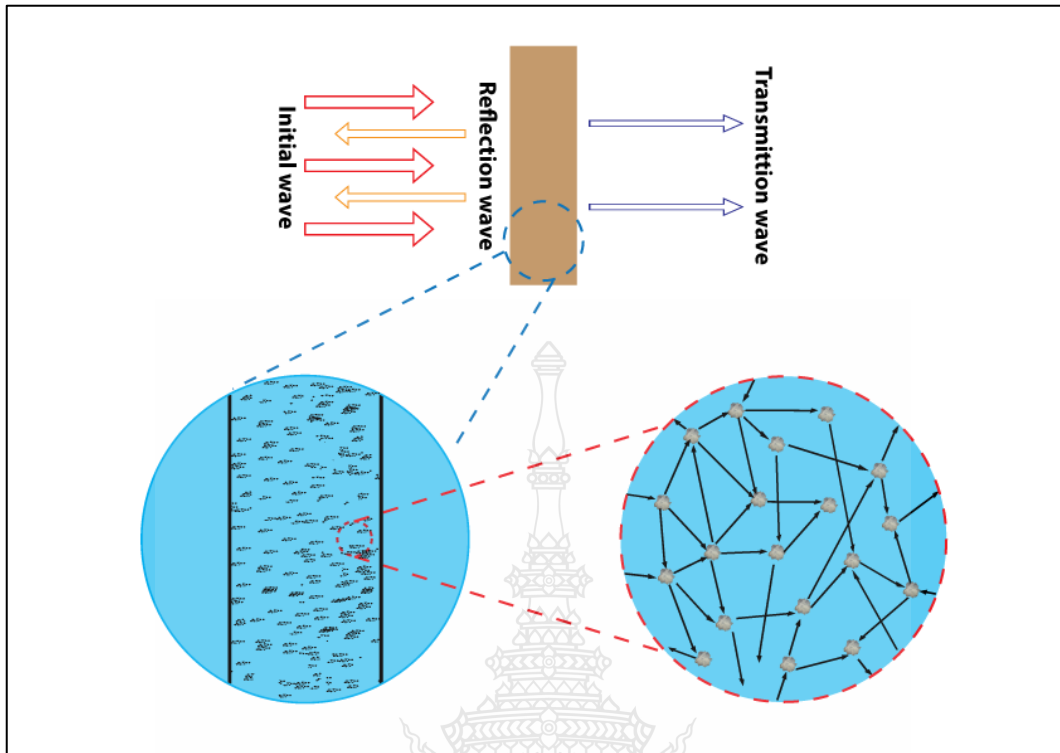
Figure 4.15 Scheme of the electromagnetic wave absorption activities.
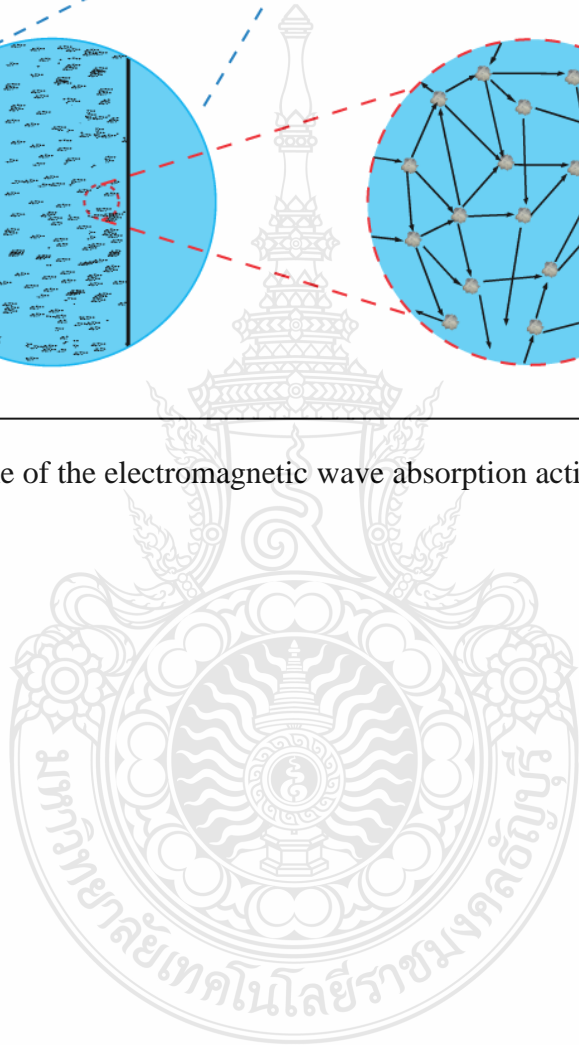
CHAPTER 5

CONCLUSIONS AND RECOMMENDATIONS

This experimental research has synthesized the nanosheets from the naturally-mineral magnetic leucoxene under the hydrothermal synthesis condition of 105ºC for 24h. The experiment opted for the naturally-mineral magnetic leucoxene as the starting material due to its high TiO_2 content (70-80%) and inexpensiveness (USD 0.5/kg).

The analysis results indicated that the magnetic leucoxene mineral is of rutile phase while the synthesized nanosheets are of titanate structure ($H_2Ti_xO_{2x+1}$) In addition, the hydrothermal treatment could remove parts of the impurities in the starting material, including Fe_2O_3, Al_2O_3, CaO, SiO_2, MnO, Nb_2O_5, MgO and SO_3, while increasing the TiO_2 content from 79.8 to 83.2wt%. The analysis also revealed that the flower-like structure of the nanosheets was slightly curved, with 100nm–2μm in width and 1-3nm in thickness. Moreover, the BET specific surface area and the pore volume of the synthesized nanosheets were respectively 279.8m^2/g and 0.609cm^3/g.

After calcination at the temperature range of 300 and 400 ºC, the calcined samples demonstrated TiO_2 (B). At 500 and 600 ºC, the calcined nanosheets revealed a bi-crystalline mixture consisting of TiO_2 (B) and anatase TiO_2. At 700–1000 ºC, the crystalline structure shows anatase and rutile phase. At 1100 ºC, the prepared samples consisted of a mixture of anatase, rutile phase of TiO_2, and Fe_2O_3 phase. At 100– 200 ºC showed sheets–like structure. At 300–1100 ºC, the calcined nanosheets became unstable and began to decompose and transform into nanoparticles. The increasing size of nanoparticle decreased the specific surface area of the nanosheets, caused by increasing calcination temperature. More importantly, the experimental nanosheets achieved the higher photocatalytic activity than did the commercial TiO_2 nanoparticles (JRC-01, JRC-03, ST-01 and P-25).

The electromagnetic wave absorber coin with nanosheets and the commercial TiO_2 nanoparticles (P-25) can absorb electromagnetic wave in gamma (γ) ray and x-ray region were 96.57 and 89.88% of the initial intensity, respectively. The electromagnetic wave absorber plates with 100 % recycled HDPE can absorb electromagnetic wave in gamma (γ) ray and x-ray region was 32.32 % of the initial intensity. The electromagnetic wave absorber plates with 25, 50, 75 and 100 % nanosheets from magnetic leucoxene mineral can absorb electromagnetic wave in gamma (γ) ray and x-ray region were 59.53, 68.94, 79.44 and 96.57% of the initial intensity, respectively. The electromagnetic wave absorber plates made from the as-synthesized nanosheets

could be used for the electromagnetic wave absorption activities in gamma (γ) ray and x-ray region.

Recommendations

        This research is hydrothermal synthesis, characterizations, and applications of nanosheets from Thai natural magnetic leucoxene mineral. The future work includes the development of nanomaterials with unique structures and properties from Thai minerals. For example, the using of the other minerals in Thailand as the starting materials and the increasing of reactor size for pilot plant and commercial products. Evaluate these materials as an electrode in solar cells and optimize the synthesis for this application.

List of Bibliography

[1]   Grätzel, M., (2001). Photoelectrochemical cells. **Nature,** *414(6861),* 338–344.

[2]   Fujishima, A. Rao, TN. and Tryk, DA. (2000). Titanium dioxide photocatalysis. **Journal of Photochemistry and Photobiology C: Photochemistry Reviews,** *1(1),* 1–21.

[3]   Ngamsinlapasathian, S., Sreethawong, T., Suzuki, Y., Yoshikawa, S., (2005). Single and double-layered mesoporous TiO_2/P25 TiO_2 electrode for dye-sensitized solar cell. **Solar Energy Materials and Solar Cells,** *86(2),* 269–282**.**

[4]   Pavasupree, S., Suzuki, Y., Pivsa-Art, S., Yoshikawa, S., (2005). Preparation and characterization of mesoporous MO_2 (M=Ti, Ce, Zr, and Hf) nanopowders by a modified sol-gel method. **Ceramics International,** *31(1),* 959–963.

[5]   Pavasupree, S., Suzuki, Y., Pivsa-Art, S., Yoshikawa, S., (2005). Preparation and characterization of mesoporous TiO_2–CeO_2 nanopowders respond to visible wavelength. **Journal of Solid State Chemistry**, *178,* 128-134.

[6]   Sreethawong, T., Suzuki, Y., Yoshikawa, S., (2005). Synthesis, characterization, and photocatalytic activity for hydrogen evolution of nanocrystalline mesoporous titania prepared by surfactant-assisted templating sol-gel process. **Journal of Solid State Chemistry**, *178(1),* 329–338.

[7]   Wu, Z., Dong, F., Zhao, W., Wang, H., Liu, Y., Guan, B., (2009). The fabrication and characterization of novel carbon doped TiO_2 nanotubes, nanowires and nanorods with high visible light photocatalytic activity. **Nanotechnology,** *20,* 235701.

[8]   Dong, F., Zhao, W., Wu, Z., (2008). Characterization and photocatalytic activities of C, N and S co-doped TiO_2 with 1D nanostructure prepared by the nano-confinement effect. **Nanotechnology,** *19,* 365607.

[9]   Mirmasoomi, S.R., Ghazi, M.M., Galedari, M., (2017). Photocatalytic degradation of diazinon under visible light using TiO_2/Fe_2O_3 nanocomposite synthesized by ultrasonic-assisted impregnation method. **Separation and Purification Technology**, *175,* 418–427.

[10]   Cheng, L., Qiu, S., Chen, J., Shao, J., Cao, S., (2017). A practical pathway for the preparation of Fe_2O_3 decorated TiO_2 photocatalyst with enhance d visible-light photo activity. **Materials Chemistry and Physics**, *190,* 53-61.

[11]   Thongsuwan, W., Singjai P., (2016). In fluence of TiO_2/Fe_2O_3 interfacial layers on optical properties under visible light. **Surface and Coatings Technology**, *306,* 49–53.

List of Bibliography (Continued)

[12]   Pavasupree, S., Ngamsinlapasathian, S., Suzuki, Y., Yoshikawa, S., (2007). Preparation and characterization of high surface area nanosheet titania with mesoporous structure. **Materials Letters,** *61(14-15),* 2973–2977.

[13]   Jitputti, J., Rattanavoravipa, T., Chuangchote, S., Pavasupree, S., Suzuki, Y., Yoshikawa, S., (2009). Low temperature hydrothermal synthesis of monodispersed flower-like titanate nanosheets. **Journal of Catalysis Communications,** *10,* 378–382.

[14]   Simpraditpan, A., Wirunmongkol, T., Pavasupree, S., Pecharapa, W., (2013). Simple Hydrothermal Preparation of Nanofibers from a Natural Ilmenite Mineral. **Ceramics International***, 39,* 2497-2502.

[15]   Aphairaj, D., Wirunmongkol, T., Pavasupree, S., Limsuwan, P., (2012). Synthesis of titanate nanotubes from Thai leucoxene mineral. **Procedia Engineering,** *32,* 1068–1072.

[16]   Chainarong, S., Niyomwas, S., Sikong, L., Pavasupree, S., (2012). The Effect of molar ratio of TiO_2/WO_3 nanocomposites on visible light prepared by hydrothermal method. **Advanced Materials Research,** *488-489,* 572–577.

[17]   Simpraditpan, A., Wirunmongkol, T., Pavasupree, S., Pecharapa, W., (2013). Effect of calcination temperature on structural and photocatalyst properties of nanofibers prepared from low-cost natural ilmenite mineral by simple hydrothermal method. **Materials Research Bulletin,** *48,* 3211–3217.

[18]   Chen, X., Mao, SS., (2006). Synthesis of titanium dioxide (TiO_2) nanomaterials. **Journal of Nanoscience and Nanotechnology***, 6(4),* 906-925.

[19]   Li, D., Xia, Y.N., (2003). Fabrication of titania nanofibers by electrospinning. **Nano Letters***, 3(1),* 555–560.

[20]   Yoo, S., Akbar, S.A., Sandhage, K.H., (2004). Oriented Single Crystal Titania nanofibers via nanocarving with hydrogenbearing gas. **Advanced Materials***, 16,* 260–264.

[21]   Hoyer, P., (1996). Formation of titanium dioxide nanotube array. **Langmuir,** *12,* 1411–1413.

[22]   Imai, H., Takei, Y., Shimizu, K., Matsuda, M., Hirashima, H., (1999). Direct preparation of anataseTiO2 nanotubes in porous alumina membranes. **Journal of Materials Chemistry***, 9,* 2971–2972.

[23]   Sun, J., Gao, L., Zhang, Q.H., (2003). TiO2 tubes synthesized by using ammonium sulfate and carbon nanotubes as templates. **Journal of Materials Science Letters***, 22,* 339–341**.**

[24]   Kobayashi, S., Hanabusa, K., Hamasaki, N., Kimura, H., Shirai, M., Shinkai, S., (2000). Preparation of TiO2 hollow–fibers using supramolecular assemblies. **Chemistry of Materials***, 12,* 1523–1525.

[25]   Gong, D., Grimes, C.A., Varghese, O.K., Hu, W.C., Singh, R.S., Chen, Z., Dickey, E.C., (2001). Titanium oxide nanotube arrays prepared by anodic oxidation. **Materials Research Bulletin**, *16,* 3331–3334.

[26]   Kasuga, T., Hiramatsu, M., Hoson, A., Sekino, T., Niihara, K., (1998). Formation of titanium oxide nanotube. **Langmuir**, *14(12),* 3160–3163.

[27]   Kasuga, T., Hiramatsu, M., Hoson, A., Sekino, T., Niihara, K., (1999). Titania nanotubes prepared by chemical processing. **Advanced Materials**. *11(15),* 1307–1311.

[28]   Pavasupree, S., Laosiripojana, N., Chuangchote, S., Sagawa, T., (2011). Fabrication and utilization of titania nanofibers from natural leucoxene mineral in photovoltaic applications. **Japanese Journal of Applied Physics**, *50(1),* 01BJ16-1–01BJ16-4.

[29]   Pavasupree, S., Ngamsinlapasathian, S., Yoshikawa, S., (2006). Synthesis and dye-sensitized solar cell performance of nanorods/nanoparticles TiO_2 from high surface area nanosheet TiO_2. **Journal of Nanoscience and Nanotechnology**, *6 (12),* 3685-3692.

[30]   Adachi, M., Murata, Y., Okada, I., Yoshikawa, S., (2003). Formation of titania nanotubes and applications for dye-sensitized solar cells. **The Electrochemical Society**, 150, *G488–G493.*

[31]   Suzuki, Y., Pavasupree, S., Yoshikawa, S., Kawahata, R., (2005). Natural rutile derived titanate nanofibers prepared by direct hydrothermal processing. **Journal of Materials Research**, *20,* 1063–1070.

[32]   Pavasupree, S., Suzuki, Y., Yoshikawa, S., Kawahata, R., (2005). Synthesis of titanate, TiO_2 (B), and anatase TiO_2 nanofibers from naturalrutile sand. **Journal of Solid State Chemistry**, *178,* 3110–3116.

[33]   Samal, S., Mohapatra, B.K., Mukherjee, P.S., Chatterjee, S.K., (2009). Integrated XRD, EPMA and XRF study of ilmenite and titania slagused in pigment production. **Journal of Alloys and Compounds**, *474,* 484–489.

[34]   Nian, J.N., Teng, H., (2006). Hydro thermalsynthesis of single-crystalline anatase TiO_2 nanorods with nanotubes as the precursor. **Journal of Physical ChemistryB**, *110,* 4139–4198.

[35]   Jung, W.H., Kwak, N.-S., Hwang T.S., Yi, K.B., (2012). Preparation of Highly Porous TiO_2 Nanofibers for dye-sensitized solar cells (DSSCs) by electro-spinning. **Applied Surface Science**, *261,* 343–352.

[36]   Carp, O., Huisman, C L., Reller, A., (2004). Photoinduced reactivity of titanium dioxide. **Progress in Solid State Chemistry**, *32,* 33–117.

[37]   Norotsky, A., Jamieson, J C., Kleppa, O J., (1967). Enthalpy of transformation of a high pressure polymorph of titanium dioxide to the rutile modifica-tion. **Science**, *158,* 338–389.

[38]   Zhang, Q., Gao, L., Guo, J., (2000). Effects of calcination on the photocatalytic properties of nanosized TiO_2 powders prepared by $TiCl_4$ hydrolysis. **Applied Catalysis B: Environmental**, *26,* 207–215.

[39]   Wisitsoraat, A., Tuantranont A., Comini, E., Sberveglieri, G., Wlodarski W., (2009). Characterization of n-type and p-type semiconductor gas sensors based on NiO_x doped TiO_2 thin films. **Thin Solid Films,** *517,* 2775–2780.

[40]   Asahi, R., Taga, Y., Mannstadt, W., Freeman, AJ., (2000). Electronic and optical properties of anatase TiO_2. **Physical Review B**, *61,* 7459–7465.

[41]   Michael, R. H., Scot, T. M., Wonyong, C., Detlef W.B., (1995). Environmental applications of semiconductor photocatalysis. **Chemical Reviews,** *95,* 69-96.

[42]   Fujishima, A., Honda, K., (1972). Electrochemical photolysis of water at a semiconductor electrode. **Nature**, *238(5358),* 37–38.

[43]   Gupta, S. M., Tripathi, M., (2011). A review of TiO_2 nanoparticles. **Chinese Science Bulletin**, *56 (16),* 1639-1657.

[44]   Pollution Control Department. "Material safety data sheet (MSDS). Titanium dioxide" [Online]. Available : msds.pcd.go.th/searchName.asp?vID=1421. 2007.

[45]   Xiaobo, C., (2009). Titanium dioxide nanomaterials and their energy applications. **Chinese Journal of Catalysis**, *30,* 839–851.

[46]   Zhang, W., Zhu, Z., Cheng, C.Y., (2011). A literature review of titanium metallurgical processes. **Hydrometallurgy**, *108,* 177–188.

[47]   Byrappa, K., Yoshimura, M., (2001).Handbook of hydrothermal technology, Noyes publications, New Jersey, USA, 2001.

[48]   Morey G. W., Niggli, P., (1913).The hydrothermal formation of silicates, A review. **Journal of the American Chemical Society**, *35,* 086–1130.

[49]   Gleiter, H., (1989). Nanocrystalline materials. **Progress in Materials Science**, *33,* 233-315.

[50]   Byrappa, K., Yoshimura, M., (2001). Handbook of hydrothermal technology, Noyes Publications, New Jersey, USA, 2001.

[51]   Byrappa, K., Adschiri, T., (2007). Hydrothermal Technology for Nanotechnology. **Progress in Crystal Growth and Characterization of Materials**, *53,* 117-166.

[52]   Cho, W., S. Yashima, M., Kakihana, M., Kudo, A., Sakata, T., Yoshimura, M., (1995). **Applied Physics Letters**, *66,* 1027-1029.

[53]   Dimitris, I., Kondarides M., PHOTOCATALYSIS, in Catalysis, [Ed. Gabriele Centi], in Encyclopedia of Life Support Systems (EOLSS), Developed under the Auspices of the UNESCO, EOLSS Publishers, Oxford, UK. 2010.

[54]   Veena, C., Dhawan, S.K., Parveen, S., Polymer based nanocomposites for electromagnetic interference (EMI) shielding EM Shielding – Theory and Development of New Materials, 2012.

[55]   Wang, Z.L., "Characterization of nanophase materials" Wiley-VCH, Weinheim, Germany, 2000.

[56]   Fultz, B., Howe, J., "Transmission electron microscopy and diffractometry of materials" Springer-Verlag Berlin Heidelberg, Germany, 2013.

[57]   Beckhoff, B., Kanngießer, B. Langhoff, N. Wedell, R.   Wolff, H. "Handbook of practical X-ray fluorescence analysis" Springer-Verlag Berlin Heidelberg, Germany, 2006.

[58]   "X-ray microscopy and imaging: X-ray fluorescence mapping" [Online]. Available : http://www.aps.anl.gov.

[59]   "X-ray   fluorescence   (XRF)"   [Online].   Available   : http://www.amptek.com/xrf_1.gif.

[60]   Pennycook, S.J.,   Nellist, P.D.,   "Scanning transmission electron microscopy" Springer-Verlag New York, United State of America.

[61]   Amelinckx, S., van Dyck, D.,   van Landuyt, J.,   van Tendeloo, G., "Electron   microscopy: principles and fundamentals" John Wiley & Sons, 2008.

[62]   "Scanning   electron   microscope."   [Online].   Available   : http://www.microscopy.ethz .ch/ images/sem.jpg

[63]   Williams, D.B., Carter, C.B., "Transmission electron microscopy" Springer US, 2009.

[64]   Leng, Y., "Materials characterization" Wiley-VCH, Weinheim, 2013.

[65]   "The   transmission   electron   microscope"   [Online].   Available   : http://www.nobelprize.org/educational/physics/microscopes/tem/.

[66]   Lowell, S., Shields, J.E., Thomas M.A., Thommes, M., "Characterization of porous solids and powders: surface area, pore size and density of nanoparticles" Springer Netherlands, 2004.

[67]   Naderi, M., "Brunauer-Emmett-Teller" *Progress   in   filtration   and Separation*, 2015, pp. 585-608.

[68]   "Brunauer, Emmett and Teller (BET) Theory" [Online]. Available : http://particle. dk/ methods-analytical-laboratory/surface-area-bet/surface-area-bet-theory/.

List of Bibliography (Continued)

[69]   Workman Jr. J., "The handbook of organic compounds: NIR, IR, raman, and UV-Vis spectra featuring polymers and surfactants" Academic Press, 2000.

[70]   "UV-Vis absorption spectroscopy" [Online]. Available : https://www2.chemistry.msu.edu/faculty/reusch/virttxtjml/spectrpy/uv-vis/uvspec.htm.

[71]   Pavasupree, S., Jitputti, J., Ngamsinlapasathian, S., Yoshikawa, S., (2008). Hydrothermal synthesis, characterization, photocatalytic activity and dye-sensitized solar cell performance of mesoporous anatase TiO_2 nanopowders **Materials Research Bulletin**, *43,* 149–157.

[72]   Jitputti, J., Pavasupree, S., Suzuki, Y., Yoshikawa, S., (2007). Synthesis and photocatalytic activity for water-splitting reaction of nanocrystalline mesoporous titania prepared by hydrothermal method. **Journal of Solid State Chemistry,** *180,* 1743–1749.

[73]   Suzuki, Y., Ngamsinlapasathian, S., Yoshida, R., Yoshikawa, S., (2006). Partially nanowire-structured TiO_2 electrode for dye-sensitized solar cells. **Central European Journal of Chemistry**, *4,* 476–488.

[74]   Fujian, L., Chun-Lin, L., Baowei, H., Wei-Ping, K., Chen-Ze. Q., (2012). High-temperature hydrothermal synthesis of crystalline mesoporous TiO_2 with superior photo catalytic activities. **Applied Surface Science**, *258,* 7448–7454.

[75]   Taicheng, A., Jikai, L., Guiying, L., Shanqing, Z., Huijun, Z., Xiangying, Z., Guoying, S., Jiamo, F., (2008). Structural and photocatalytic degradation characteristics of hydrothermally treated mesoporous TiO_2. **Applied Catalysis A: General.** *350,* 237–243.

[76]   Huajun, F., Min-Hong, Z., Liya, E., (2012). Hydrothermal synthesis and photocatalytic performance of metal-ionsdoped TiO_2. **Applied Catalysis A : General**, *413–414,* 238– 244.

[77]   Lin, W., Yun, G., Xiao-Hong, X., Quan-Rong, D., Shao, G., (2011). Phase selection and visible light photo-catalytic activity of Fe-doped TiO_2 prepared by the hydrothermal method. **Materials Research Bulletin**, *46,* 442–446.

[78]   Li, X., Chen, Z., Yongchao, S., Liu, y., (2011). Preparation of N, Fe co-doped $TiO_2$with visible light response. **Powder Technology**, *207,* 165 –169.

[79]   Sood, S., Umar, A., Kumar, S., Sushil, M., Kansal, K., (2015). Highly effective Fe-doped TiO_2 nanoparticles photocatalysts for visible-light driven photocatalytic degradation of toxic organic compounds. **Journal of Colloid and Interface Science**, *450,* 213–223.

[80]   Liu , P., Huang, Y., Yang, Y., Yan, J., Zhang, X., (2016). Sandwich structures of graphene@Fe_3O_4 @PANI decorated with TiO_2 nanosheets for enhanced electromagnetic wave absorption properties. **Journal of Alloys and Compounds***, 662,* 63- 68.

[81]   Zong, M., Huang, Y., Zhao,Y., Wang, L., Liu, P., Wang, Y., Wang, Q., (2013). One-pot simplified co-precipitation synthesis of reduced grapheme oxide/Fe_3O_4composite and its microwave electromagnetic properties, **Materials Letters***, 10 (6),* 22–25.

[82]   Kangle, Lv., Quanjun, X., Jiaguo, Y., (2011).   Effect of calcination temperature on morphology and photocatalytic activity of anatase TiO_2 nanosheets with exposed {001} facets. **Applied Catalysis B: Environmental.** *104,* 275–281.

[83]   Wu, JM., Song, X.M., Yan, M., (2011). Alkaline hydrothermal synthesis of homogeneous titania microspheres with urchin-like nanoarchitectures for dye effluent treatmentsJournal of Hazardous. **Materials** *194,* 338–344.

[84]   Huang, H., Yu, Z., Zhu, W., Gan, Y., Xia, Y., Tao, X., Zhang, W., (2014). Hierarchically porous nanoflowers from TiO_2– B nanosheets with ultrahigh surface area for advanced lithium-ion batteries. **Journal of Physics and Chemistry of Solids,** *75,* 619– 623.

[85]   Chen, K., Jiang, Z., Qin, J., Jiang, Y., Li, R., Tang, H., Yang, X., (2014). Synthesis and improved photocatalytic activity of ultrathin TiO_2 Nanosheets with nearly 100% exposed (001) facets. **Ceramics International** *40,* 16817– 16823.

[86]   Que, YP., Weng, J., Hu, LH., Wu, JH., Dai, SY., (2016). High open voltage and superior light- harvesting dye-sensitized solar cells fabricated by flower-like hierarchical TiO_2 composed with highly crystalline nanosheets. **Journal of Power Sources,** *307,* 138-145.

[87]   Shen, B., Li, Y., Yi, D., Zhai, W., Wei, X., Zheng, W., (2016). Microcellular graphene foam for improved broadband electromagnetic interference shielding. **Carbon,** *102,* 154-160.

[88]   Yang, Y., Zhao, Y., Sun, S., Zhang, X., Duan, L., Ge, X., Lü, W., (2016). Self-assembled three-dimensional graphene/Fe_3O_4 hydrogel for efficient pollutant adsorption and electromagnetic wave absorption. **Materials Research Bulletin**, *73,* 401– 408.

[89]   Yuan, X., Cheng, L., Kong, L., Yin, X., Zhang, L., (2014). Preparation of titanium carbide nanowires for application in electromagnetic wave absorption. **Journal of Alloys and Compounds**, *596,* 132–139.

[90]   Wang, H., Zheng, K., Zhang, X., Ding, X., Zhang, Z., Bao, C., Guo, L., Chen, L.,Tian, X., (2016). 3D network porous polymeric composites with outstanding electromagnetic interference shielding. **Composites Science and Technology**, *125,* 22-29.

[91]   Wang, Y., Peng, Z., Jiang, W., (2016). Controlled synthesis of Fe_3O_4@SnO2/RGO nanocomposite for microwave absorption enhancement. **Ceramics International,** *42.* 10682– 10689.

[92]   Yang, Z., Luo, F., Zhou, W., Zhu, D., Huang, Z., (2016). Design of a broadband electromagnetic absorbers based on TiO_2/Al_2O_3 ceramic coatings with metamaterial surfaces. **Journal of Alloys and Compounds,** *6 (87),* 384 - 388.

[93]   Jia, Q., Wang, W., Zhao, J., Xiao, J., Lu, L., Fan, H., (2017). Synthesis and characterization of TiO_2 /polyaniline /graphene oxide bouquet-like composites for enhanced microwave absorption performance. **Journal of Alloys and Compounds**, *710,* 717 -724.

[94]   Lu, L., He, Y., Ping, B., Wang, F., Hu, S., (2017). TiO_2 containing electromagnetic wave absorbing aggregate and its application in concrete Construction and Building. **Materials,** *134*, 602–609.

[95]   Pawar, SP., Biswas, S., Kar, GP., Bose, S., (2016). High frequency millimetre wave absorbers derived from polymeric nanocomposites. **Polymer**, *84,* 398- 419.

[96]   Tian, H., Wan, C., Xue, X., Hu, X., Wang, X., (2017). Effective electron transfer pathway of the ternary TiO_2 /RGO /Ag nanocomposite with enhanced photocatalytic activity under visible light. **Catalysts**, *7, 156.* doi:10.3390/catal7050156

[97]   Truppi, A., Petronella, F., Placido, T., Striccoli, M., Agostiano, A., Curri, ML., Comparelli, R., (2017). Visible-light-active TiO_2-based hybrid nanocatalysts for environmental applications. **Catalysts**, *7, 100*; doi:10.3390/catal7040100.

[98]   Suzuki, Y., Yoshikawa, S., (2004). Synthesis and thermal analyses of TiO_2-derived nanotubes prepared by the hydrothermal method. **Journal of Materials Research**, *19 (4),* 982–985.

[99]   Yoshida. R., Suzuki, Y., Yoshikawa, S., (2005). Effects of synthetic conditions and heat treatment on the structure of partially ion-exchanged titanate nanotubes. **Materials Chemistry and Physics**, *91 (2-3),* 409–416.

[100]   Yoshida, R., Suzuki, Y., Yoshikawa, S., (2005). Syntheses of TiO_2 nanowires and TiO_2 anatase nanowires by hydrothermal and post-heat treatments. **Journal of Solid State Chemistry**, *178(7),* 2179–2185.

[101] Suzuki, Y., Pavasupree, S., Yoshikawa, S., Kawahata, R., (2006). Direct hydrothermal processing of long titanate nanofibers from natural rutile. **Key Engineering Materials**, *317-318,* 243–246.

[102] Rungpin, N., Pavasupree, S., Prasassarakich, P., Poompradub, S., (2015). Production of nano-calcium carbonate from shells of the freshwater channeled applesnail, Pomacea canaliculata, by hydrothermal treatment and its application with polyvinyl chloride. **Polymer Composites**, *36,* 1620-1628.

[103] Diakonov, I.I., Schott, J., Martin, F., Harrichourry, J.C., Escalier, J., (1999). Geochim, iron(III) solubility and speciation in aqueous solutions. Experimental study and modelling: Part 1. Hematite solubility from 60 to 300 $^\circ$C in NaOH–NaCl solutions and thermodynamic properties of $Fe(OH)_4^-$(aq). **Geochimica et Cosmochimica Acta**, *63,* 2247–2261.

[104] Khan, M.A., Woo, S.I., Yang, O.-B., (2008). Hydrothermally stabilizedFe(III) doped titania active under visible light for water splittingreaction. **International Journal of Hydrogen Energy,** *33*, 5345–5351.

[105] Li, H., Li, T., Liu, H., Huang, B., Zhang, Q., (2016). Hierarchical flower-like nanostructures of anatase TiO_2 nanosheets dominated by {0 01} facets. **Journal of Alloys and Compounds**, *657*, 1–7.

[106] Lu, J., Zhao, L., Li, J., Zheng, L., Zhang, L., Gong, Z., Wang, Z., Zhu, A., (2011). A systematic study on evolution mechanism of titanate nanostructures in the hydrothermal process. **Chemical Physics Letters**, *508*, 258–264.

[107] Li, Y., Sheng, H., Zhang, J., Xue, K., Zheng, Q., Huo, H., Zou, H., (2011). Synthesis and luminescent properties of TiO_2:Eu^{3+} nanotubes. **Powder Technology,** *212*, 372 –377.

[108] Sun, Z., Liao, T., Dou, Y., Hwang, S.M., Park, MS., Jiang, L., Kim, JH., Dou, S.X., (2014). Generalized self-assembly of scalable two-dimensional transition metal oxide nanosheets. **Nature Communication**, *5(3813),* 1–9.

[109] Sakai, N., Fukuda, K., Shibata, T., Ebina,Y., Takada, K., Sasaki, T., (2006). Photoinduced hydrophilic conversion properties of titania nanosheets. **Journal of Physical Chemistry B**, *110(12),* 6198–6203.

[110] Sakai, N., Ebina, Y., Takada, K., Sasaki, T., (2004). Electronic band structure of titania semiconductor nanosheets revealed by electrochemical and photoelectrochemical studies. **Journal of the American Chemical Society**, *126(18),* 5851–5858.

[111] Awwad, S., Omar, A., Khashman Gasan, I., Bisharat, R., (2010). Photocatalytic degradation of phenol using Fe-TiO_2 by different illumination sources, **International Journal of Chemistry**, *2*, 10–18.

[112]   Sun, Z., Liao, T., Dou, Y., Hwang, S.M., Park, MS., Jiang, L., Kim, JH.,
         Dou, S.X., (2014). Generalized self-assembly of scalable two-dimensional
         transition metal oxide nanosheets. **Nature Communications**, *5*, 1–9.

APPENDICES

(List of Publications)
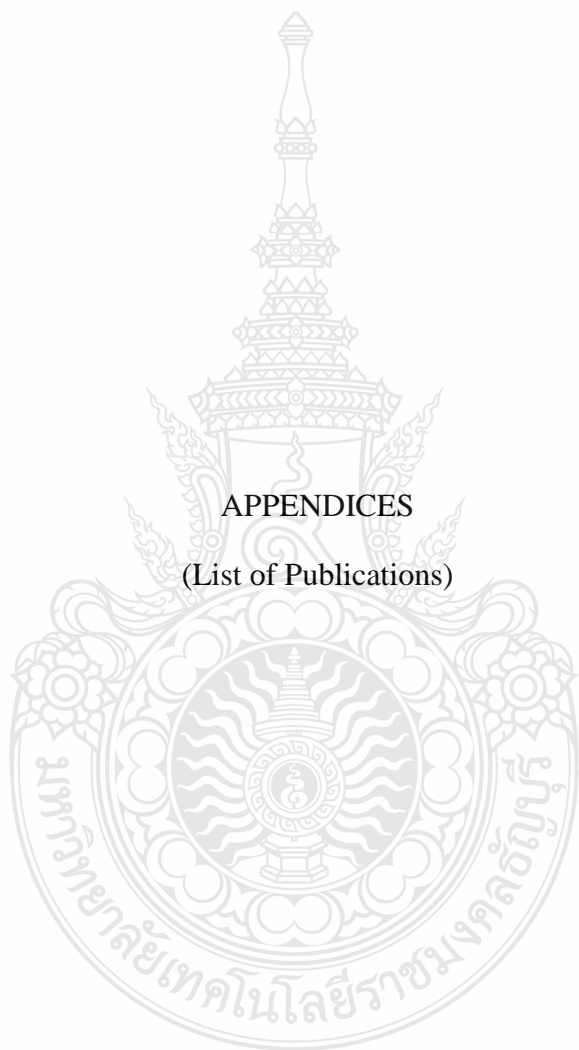
List of Publications

International Journal

1. **Wissanu Charerntanom** Wisanu Pecharapa Suttipan Pavasupree and Sorapong Pavasupree "Effect of calcination temperature on structure and photocatalytic activity under UV and visible light of nanosheets from low-cost magnetic leucoxene mineral" Photonics and Nanostructures– Fundamentals and Applications 25(2017) 38–45.
Impact Factor 2016 = 1.705
https://doi.org/10.1016/j.photonics.2017.04.007

International Conferences

1. **W. Charerntanom**, A. Simpraditpan, N. O-Charoen, N. Srisawat, W. Pecharapa and S. Pavasupree "Hydrothermal preparation and MB photocatalytic activity under UV light of nanosheets from natural magnetic leucoxene mineral" Proceeding, Science and Technology of Emerging Materials (STEMa 2016), Pattaya, Thailand, July 27-29, 2016, pp. 23-26.

2. **W. Charerntanom**, A. Simpraditpan, N. O-Charoen, N. Srisawat, W. Pecharapa and S. Pavasupree "Preparation of n-type semiconductor nanosheets from natural Thai ilmenite mineral for electromagnetic wave absorber" Proceeding, Science and Technology of Emerging Materials (STEMa 2016), Pattaya, Thailand, July 27-29, 2016, pp. 31-34.

3. **W. Charerntanom**, N. O-Charoen, K. Sungsanit, V. Chobpattana, W. Pecharapa and S. Pavasupree "Preparation and high photocatalyst nanosheets from natural Thai magnetic leucoxene mineral," 13th Eco-Energy and Materials Science and Engineering Symposium (13th EMSES 2016), Udonthani, Thailand, December 1-3, 2016, pp. 280-283.

National Conferences

1. **W. Charerntanom**, J. Numprasert, P. Kummeesith, C. Sea-aung, N. O-Charoen, K. Sungsanit, S. Jaiyen, N. Srisawat and S. Pavasupree "Preparation of electromagnetic wave absorber plate using recycled HDPE and micro materials from Thai minerals" Proceeding, Industrial

Engineering Network Conference 2016 (IE NETWORK 2016), Kosa Hotel, Khon Kaen, Thailand, July 7-8, 2016, pp. 1300-1305.

2. **W. Charerntanom**, N. O-Charoen, S. Jaiyen and S. Pavasupree "Preparation of electromagnetic wave absorber plate using recycled HDPE and micro materials from natural Thai rutile minerals" Proceeding, The 2nd National Conference on Industrial Technology and Engineering (NCITE 2016), Ubonratchathani, Thailand, October 19, 2016, pp. 191-197.

3. **W. Charerntanom**, N. O-Charoen and S. Pavasupree "Preparation of electromagnetic wave absorber plate using recycled HDPE and micro materials from natural Thai magnetic leucoxene minerals" Proceedings of the 9th Conference of Electrical Engineering Network of Rajamangala University of Technology 2017 (EENET 2017) KP Grand Hotel Chanthaburi, Thailand, May 2-4, 2017, pp. 618-621.

Petty Patent

1. Petty Patent "The preparation of nanomaterial from magnetic leucoxene mineral for X-ray absorption and shielding" Inventor / designer **Mr. Wissanu Charerntanom** and Assistant Professor Dr. Sorapong Pavasupree Patent number. 11668 Request number. 1503002104 (December 14 2015).

2. Petty Patent "The preparation of nanosheets from ilmenite mineral for textile dye degradation" Inventor / designer **Mr. Wissanu Charerntanom** and Assistant Professor Dr. Sorapong Pavasupree Patent number. 11669 Request number. 1503002105 (December 14 2015).

3. Petty Patent "The preparation of nanosheets from magnetic leucoxene mineral for photocatalyst" Inventor / designer **Mr. Wissanu Charerntanom** and Assistant Professor Dr. Sorapong Pavasupree Patent number. 11670 Request number. 1503002106 (December 14 2015).

Awards

1. Best paper presentation award

W. Charerntanom, N. O-Charoen, S. Jaiyen and S. Pavasupree "Preparation of electromagnetic wave absorber plate using recycled HDPE and micro materials from natural Thai rutile minerals" Proceeding, The 2nd National Conference on Industrial Technology and Engineering (NCITE 2016), Ubonratchathani, Thailand, October 19, 2016.

2. Best engineering invention contest

W. Charerntanom and S. Pavasupree "Preparation of nanosheets from magnetic leucoxene mineral for photocatalytic activities and electromagnetic wave absorber application" The 6th RMUTT Young Talent Inventor Awards, Rajamangala University of Technology Thanyaburi, June 6, 2017.

Biography

Name - Surname	Wissanu Charerntanom
Date of Birth	12 September 1983
Address	110/15 Moo 1, Tambon Nong Sang district Wapipathum Mahasarakham 44120
Education	Bachelor's Degree in Petrochemicals and Polymeric Material Engineering, Faculty of Engineering, Silpakorn University
	Master of Engineering (Material Engineering) Faculty of Engineering, Rajamangala University of Technology Thanyaburi (RMUTT)
	Doctor of Engineering Program in Energy and Materials Engineering (International Program), Faculty of Engineering, Rajamangala University of Technology Thanyaburi (RMUTT)
Experience Work	Printing Section Leader Fuji name (Thailand) Co., Ltd. Production Section Leader Manee Mongkol Import-Export Co., Ltd. Research Assistant, Department of Materials and Metallurgical, Engineering Faculty of Engineering, Rajamangala University of Technology Thanyaburi (RMUTT) 2012- Present.
Telephone Number	08-4767-1388
Email Address	wissanu_c@mail.rmutt.ac.th